CENTRO DE INVESTIGACIONES
EN OPTICA, A.C.

Up-converted Luminescent Properties of Rare-earth doped ZrO_2 Nanocrystals

A dissertation submitted by

David Octavio Solís Santana

In partial fulfillment of the requirements for the degree of

Doctor in Science (Optics)

León, Gto. **December 2010**

Up-converted Luminescent Properties of Rare-earth doped ZrO_2 Nanocrystals

A dissertation
submitted by

David Octavio Solís Santana

In partial fulfillment of the requirements for the degree of Doctor in Science (Optics)

CENTRO DE INVESTIGACIONES EN ÓPTICA A.C.

Advisor:
Dr. ELDER DE LA ROSA CRUZ

León, Gto. **December 2010**

HOW GRAD SCHOOL IS JUST LIKE KINDERGARTEN

ALL DAY NAPPING IS ACCEPTABLE

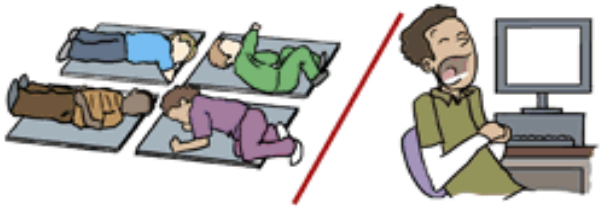

THERE IS CONSTANT ADULT SUPERVISION

YOU GET COOKIES FOR LUNCH

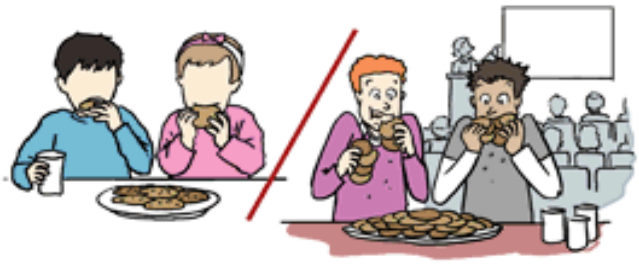

MOST COMMON ACTIVITY: CUTTING AND PASTING

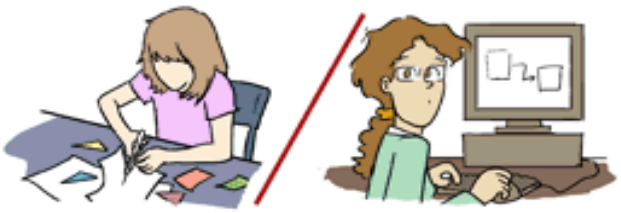

THERE ARE NO GRADES
(YOU JUST HAVE TO PLAY WELL WITH OTHERS)

CRYING FOR YOUR MOMMY IS NORMAL

To my parents, for their trustfulness

To my sisters, for their fondness

To my godparents, for their friendliness

To my nephews: Alejandro and Mauricio

To an unconditional person: Lucy

To my friends at C.I.O

CARPE DIEM

Acknowledgements

The main acknowledgement is to my advisor Dr. Elder de la Rosa by his unflagging efforts and support related to this research during my permanence at C.I.O., as well as his supervising for this work. The author also expresses gratitude to Dr. Pedro Salas, Dr. Carlos Angeles Chávez and Dr. Ascención Montoya, for their help in the XRD, TEM and HRTEM characterization; to Luis Meza and Dr. Luis Díaz for the rate-equation model applied. Credit are also to the Consejo Nacional de Ciencia y Tecnología (CONACyT) for the Ph.D scholarship I was granted. I extend my thanks to Luis Meza, Dr. Tzarara López and Sean Anderson by the partnership work, as well as Martín Olmos by his cooperation at laboratory. I should also express gratitude to the reviewers of the thesis for their valuable comments and suggestions, Dr. Luis Díaz and Dr. M. Antonio Meneses from Centro de Investigaciones en Óptica, as well as Dr. Gustavo Hirata from Centro de Nanociencias y Nanotecnología, Institute pertaining to UNAM and located in Ensenada, B.C.N. Finally I am grateful to the personnel and friends at C.I.O.

Abstract

ZrO_2 nanocrystalline samples doped with different concentrations of Erbium, Holmium and Thulium ions, using Ytterbium as a sensitizer, were prepared by sol-gel and solvothermal chemical methods and annealed applying determined temperature routes as well as surface supplemental modifiers. Concentration ranges for each ion were established for producing high emission intensity samples, along with an analysis of the crystalline structure and crystallite size of the host. The structural and morphological characterization showed that the introduction of different ion concentrations affect the crystalline structure stability. The samples were pumped at 970 nm with a semiconductor laser source, thus the up-converted luminescence and the change in the peak intensities of the measured bands were studied. According to experimental results, there is a strong influence of both Yb^{3+} and Er^{3+} ion concentrations over the red/green ratio mainly due to the cross-relaxation, process that is theoretically interpreted in this work. Green UC emission from Ho^{3+} presented the highest efficiency, with a decay constant of 360 μs, for the 2/0.001 mol% Yb/Ho composition. This yields a chromatic coordinate of (0.289, 0.699) with a maximum luminance of 8.7×10^{-3} lm. The blue UC emission from Tm^{3+} is presumably and favorably affected by similar cross-relaxation channel as well. The strong increase in blue signal for very low concentration of Tm^{3+} can be attributed to the reduction of inter-ionic cluster interactions. It is clear that the excitation dynamics is a relevant part on the luminescent processes and the effect by material preparation. From the results, a procedure for color emission tuning is proposed, as well as the feasibility of obtaining white light emission from a combination of several rare-earth ions concentrations. The viability of strong and tunable color emission signals make these nanocrystals very attractive for luminescence labeling in biomedical applications.

Abstract

Muestras nanocristalinas de ZrO_2 dopado con diferentes concentraciones de iones de erbio, holmio y tulio, además de yterbio como sensibilizador, fueron sintetizadas por los métodos químicos sol-gel y solvotermal, utilizando un recocido con determinadas rutas de temperatura, así como modificadores de superficie. Se establecieron los intervalos de concentración por cada ion para la producción de muestras con alta intensidad de emisión, junto con un análisis de la estructura cristalina y el tamaño de cristal involucrados. La caracterización estructural y morfológica mostró que la introducción de diferentes concentraciones de iones afecta la estabilidad y la estructura cristalina. Las muestras se excitaron por medio de un diodo láser a 970 nm y se estudió la luminiscencia de conversión ascendente (UC), así como el cambio en las intensidades pico de las bandas de emisión. De acuerdo a la evidencia hallada, hay una fuerte influencia de las concentraciones de iones de yterbio y erbio en la relación de la emisión rojo/verde, comportamiento debido principalmente al proceso de relajación cruzada (CR), proceso que es interpretado teóricamente. La emisión verde de UC del Ho^{3+} presentó la mayor eficiencia, con una constante de decaimiento de 360 µs, para la composición 2/0.001% mol de Yb/Ho. Esto produce una coordenada cromática de (0.289, 0.699) con una luminosidad máxima de $8{,}7 \times 10^{-3}$ lm. La emisión azul del tulio se vio favorecida por un canal similar de CR y para concentraciones muy bajas de Tm^{3+} se puede atribuir a la reducción de interacciones entre grupos inter-iónicos. Es evidente que la dinámica de excitación es una parte importante en los procesos luminiscentes, así como el efecto de la preparación del material. A partir de estos resultados, se propone un procedimiento para sintonizar el color de la emisión, así como la posibilidad de obtener la emisión de luz blanca a partir de una combinación de concentraciones de varios iones. La viabilidad de una señal intensa y la posibilidad de sintonizar el color de la emisión de estos nanocristales resulta atractivo para las aplicaciones biomédicas de marcadores por luminiscencia.

Preface

Research on nanoscale materials is rapidly increasing due to their potential applications in the development of state-of-the-art technologies. Among the various nanoscale materials, trivalent lanthanide (Ln^{3+})-doped oxide nanocrystals are particularly attractive both from a fundamental and a practical point of view mainly due to their unique luminescence properties arising from the intra 4*f* transitions [1,2]. These inner 4*f* electrons are well shielded by the outer 5*s* and 5*p* orbitals giving rise to a strong and sharp emission due to weak interactions with the host lattice. The lanthanide ions can undergo the well-known process of up-conversion (UC) where they can convert low energy near infrared (NIR) radiation to emission of higher energies such as visible and/or UV light [3,4]. Although electron confinement effect is not expected due to localization of electrons in atomic orbitals of active ions, the excitation dynamics is influenced by the nanoscopic interaction that can induce an enhancement in the fluorescence emission.

Taking advantage of up-conversion, one may tailor the visible emission wavelengths to obtain almost any desired visible emission by using different combinations of Ln^{3+} ions, after typical excitation centered at 970-980 nm. Such characteristics make this kind of nanomaterials an interesting alternative to quantum dots in the development of a feasible powerful tool to modern detection technologies. In contrast to conventional fluorescent reporters (QDs and fluorophores), up-converting nanophosphors do not bleach and allow permanent excitation with simultaneous signal integration. A large anti-Stokes shift (up to 500 nm) separates discrete emission peaks from the infrared excitation source. Along with the high contrast in biological specimens due to the absence of self-fluorescence upon infrared excitation, up-converting phosphor technology (UPT) has unique properties for highly sensitive particle-based assays [5].

UPT can also find application on the generation of white light for solid-state lighting and displays. The technology of visible light sources based on frequency up-conversion (UC) of rare-earth (RE) doped materials has been revisited recently [6]. This application could be possible due to the development of powerful 970-980 nm diode lasers for the telecommunication industry and as part of the Super High Efficiency Diode Sources (SHEDS) program [7]. The SHEDS projects an electrical to optical efficiency of 85%. As a result of this development, the up-conversion technology which appeared to be too inefficient in the past now has attainable practical applications, including full color displays.

Whatever the application is considered, oxide nanocrystals with strong UC visible emission will be required. RGB emission, tunability of the emitted signal, high emission intensity, crystallite size and low cost preparation method are key parameters that must be considered for the development of this kind of nanomaterials. The UC process is nonlinear in nature and as a result, its efficiency increases depending on the properties of the emitter [6,8,18], hence it is not straightforward to tailor a color or white emitter with optimum performances. The use of Yb^{3+} as a sensitizer ion, improves the UC efficiency of Er^{3+} and makes possible the visible emission from both Ho^{3+} and Tm^{3+} [9-13]. High doping densities are usually required in order to make possible such energy transfer. However, even at lower doping densities, some host media have a tendency for clustering the dopants, facilitating the energy transfers or migration between similar ions. Thus, ion concentration of sensitizer and active ion play an important role on the up-conversion emission. The challenge is to select the appropriate concentration not only to improve the emission efficiency but also to tune the color emission.

In addition, UC emission may be strongly quenched by multi-phonon transitions, as these can reduce the lifetimes of metastable levels. The phonon energy of the host plays an important role in the UC process, as lower the phonon energy higher the up-conversion emission. However, in some cases it promotes the population of some energy level that in turn produces visible emission. Impurities introduced during the synthesis process also promote non-radiative relaxations and quench the UC emission. This is why the selection of host is

important, and why the synthesis process should be improved, in addition to control crystallite size and maintain good solubility and low cost. Several doped oxide nanocrystals has been reported, perhaps the most studied are YAG and Y_2O_3 with 850 cm^{-1} and 597 cm^{-1} of phonon energy, respectively [12,14-16]. However, the searches for new host with lower phonon energy deserve special attention.

In this thesis work, we propose the Er^{3+}, Tm^{3+} and Ho^{3+} doped ZrO_2 nanocrystals codoped with Yb^{3+} used as sensitizer as a new nanophosphor with strong up-converted signal emitted, controlled crystallite size, RGB visible emission, tunability in the visible range and prepared using a simple wet chemical method. Zirconium dioxide (ZrO_2) is chemically and thermally stable, and has low phonon energy of about 470 cm^{-1} that is small compared to that of other hosts [17,18]. This low phonon energy opens up the possibility of higher UC emission of active ions incorporated into the host. Thus, combining the properties of rare-earth ions, nanosize, and good qualities of ZrO_2, the study of luminescent properties in zirconium dioxide nanocrystals is worthy of attention in the field of sensitive particle for biolabeling and solid-state lighting. Recently, in our group, we have demonstrated UC emission of Er^{3+}, Yb^{3+}/Er^{3+} and Yb^{3+}/Ho^{3+} doped ZrO_2 nanocrystals [19,20,21]. However, no systematic study of ions concentration to improve emitted signal and tunability has been reported.

Here in this thesis, we report the structural properties of the host after doping; searching for optimum concentration of ions for each proposed system (green, red and blue); feasible control tuning for determined emission color; description of luminescent processes related to each emission; as well as to exploit a particular synthesis method that may be partially modified so as to obtain better results.

The objectives of the PhD thesis project can be described as follows:

- Study of lanthanides composition effect on the intensity and color of the UC emitted signal and determine the optimal composition to maximize produced signal.

- Demonstrate the ability to color tuning in lanthanide doped nanocrystals, in particular make evident the generation of white light.
- Study the influence of preparation method and its correlation with the optimization and color of emitted signal, in order to determine the most appropriate method.
- To understand the relaxation mechanism of lanthanide co-doped nanocrystals associated to the up-converted signal.

With those above objectives is attempted to achieve the following goal: obtain lanthanide-doped ZrO_2 nanocrystals with high up-converted emitted signal and white emission by color tuning in the visible spectrum, produced through low-cost chemical methods.

This thesis work is based on up-converted luminescence of RE^{3+} (RE= Er, Ho, Tm and Er-Tm) rare-earth ions on ZrO_2 nanocrystals using Yb^{3+} as sensitizer, and focuses on controlling the produced up-conversion, resulting in the enhancement of emission. It is organized into six parts that cover several aspects associated with each analyzed oxide nanomaterial. **Chapter 1** deals with fundamental aspects such as the description of rare-earth elements and their characteristic that promotes luminescence; the properties related to nanoparticles from which a proper use could enhance expected luminescence; the chemical methods that were developed during this work; as well as the behavior of nanostructured oxides and a brief explanation about up-conversion. **Chapter 2** describes the characterization of the structural and luminescent properties of Yb-Er co-doped ZrO_2 nanocrystals, a steady state model for the energy's transition dynamic is included, as well as related structural and luminescent effects resulting from Pluronic F-127 surfactant, which was taken into account to enhance following samples elaborated for this work. **Chapter 3** deals with the structural and luminescence characterization of Yb^{3+}-Ho^{3+}, obtaining the best composition of lanthanides for highest luminescence and a way to measure color and intensity of emitted signal. **Chapter 4** reports the structural and luminescence properties of Yb^{3+}-Tm^{3+}, the composition of lanthanides that maximize up-converted emitted signal; an alternative thermal modification is considered, along with the cooperative emission of Yb^{3+} that efficiently occurs in this system, and finally

the luminescence by rare-earth remnants into the host. With all that acquired information, this study became the groundwork for **Chapter 5**, in which a multi-doped nanocrystal is proposed to obtain feasible color tuning, focused on potential technological applications. Finally, in **Chapter 6** the physicochemical properties of zirconium dioxide nanoparticles are broadly disclosed trough a general point of view, as well as conclusions about the acquired data are explained. With this thesis work, it might be expected that the goal to achieve an applicable result on RE^{3+} doped ZrO_2 nanocrystals could be accomplished in the near future.

References

[1] F. Vetrone, J.-C. Boyer, J. A. Capobianco, In “The Handbook of Luminescence, Display Materials and Devices”, Nalwa, H. S. and Rohwer, L. S. (Eds.), American Scientific Publishers, Stevenson Ranch, CA, 2003; Chapter 3, pp 141− 182

[2] Blasse, G.; Grabmaier, B. C., “Luminescent Materials”, Springer, Berlin, 1994

[3] Auzel, F., “Upconversion and anti-Stokes processes with f and d ions in solids”, Chem. Rev. **104**, 139 173 (2004)

[4] Pollnau, M.; Gamelin, D. R.; Lthi, S. R.; Gdel, H. U.; Hehlen, M. P., “Power Dependence of Upconversion Luminescence in Lanthanide and Transition-Metal-Ion Systems”, Phys. Rev. B **2000** 61 3337 3346

[5] Corstjens, P.L.A.M., “Infrared up-converting phosphors for bioassays”, IEE Proceedings - Nanobiotechnology **152**(2), 64 (2005)

[6] Rapaport, A.; Milliez, J.; Cassanho, A.; Jenssen, H.; Bass, M., “Review of the properties of up-conversion phosphors for new emissive displays,” J. Display Technol. **2**(1), 68–78, Mar. 2006.

[7] “SHEDS: The next revolution for the laser diode,” Photon. Spectra, pp. 89–118, Jan. 2005

[8] F. Auzel, “Application of resonant energy transfers to the laser effect in Er-doped glasses,” Ann. Telecommun. **24**, 363–376 (1969)

[9] D. Matsuura, "Red, green, and blue upconversion luminescence of trivalent-rare-earth ion-doped Y_2O_3 nanocrystals", Applied Physics Letters **81**(24), 4526 (2002)

[10] A.V. Kir'yanov, A. Belovolov, M.I. Timoshechkin, V. Aboites, M.I. Belovolov, M.J. Damzen, A. Minassian, "Powerful visible (530-770 nm) luminescence in Yb, Ho: GGG with IR diode pumping. Optics express **10**(16), 832-9 (2002)

[11] J.C. Boyer, F. Vetrone, J.A. Capobianco, A. Speghini, M. Bettinelli, "Yb^{3+} ion as a sensitizer for the upconversion luminescence in nanocrystalline $Gd_3Ga_5O_{12}$: Ho^{3+}", Chemical Physics Letters **390**(4-6), 403-407 (2004)

[12] M. Liu, S. Wang, J. Zhang, L. An, L. Chen, "Upconversion luminescence of $Y_3Al_5O_{12}$ (YAG):Yb^{3+}, Tm^{3+} nanocrystals" Optical Materials **30**(3), 370-374 (2007)

[13] T. M. Kozhan, V. V. Kuznetsova, I. I. Sergeev, V. S. Khomenko, P. P Pershukevich, V. A. Chernyavskii, "Luminescence of Tm^{3+} ions in yttrium oxide", Journal of Applied Spectroscopy **68**(3), 355-358 (2001)

[14] F. Vetrone, J.C. Boyer, J.A. Capobianco, A. Speghini, M. Bettinelli, "Effect of Yb^{3+} Codoping on the Upconversion Emission in Nanocrystalline Y_2O_3:Er^{3+}", Journal of Physical Chemistry B **107**(5), 1107-1112 (2003)

[15] Qin, G.; Lu, J.; Bisson, J.F.; Feng, Y.; Ueda, K.; Yagi, H.; Yanagitani, "Upconversion luminescence of Er in highly transparent YAG ceramics", T. Solid State Communications **132** (2004) 103-106

[16] De, G.; Qin, W.; Zhang, J.; Zhang, J.; Wang, Y.; Cao, C.; Cui, Y., "Upconversion luminescence properties of $Y2O_3$:Yb^{3+}, Er^{3+} nanostructures", Journal of Luminescence **119-120** (2006) 258-263

[17] W. Córdova-Martínez, E. De la Rosa-Cruz, L.A. Díaz-Torres, P. Salas, A. Montoya, M. Avendaño, R.A. Rodríguez, O. Barbosa-García, "Nanocrystalline tetragonal zirconium oxide stabilization at low temperatures by using rare earth ions: Sm^{3+} and Tb^{3+}", Opt. Mater. **20**, 263 (2002)

[18] A. Patra, C. S. Friend, R. Kapoor, and P. N. Prasad, "Up- conversion in Er^{3+}: ZrO_2 nanocrystals," Journal of Physical Chemistry B **106**(8), 1909–1912 (2002)

[19] T. Lopez-Luke, E. De la Rosa, P. Salas, C. Angeles-Chavez, L. A. Diaz-Torres, S. Bribiesca, "Enhancing the up-conversion emission of ZrO_2 : Er^{3+} nanocrystals prepared by a micelle process," Journal of Physical Chemistry C **111**(45), 17110-17117 (2007)

[20] E. De la Rosa, P. Salas, H. Desirena, C. Angeles, R. A. Rodriguez, "Strong green upconversion emission in ZrO_2 : Yb^{3+}-Ho^{3+} nanocrystals," Applied Physics Letters, **87**(24), (2005)

[21] D. Solís, T. López-Luke, E. De la Rosa, P. Salas, C. Angeles-Chavez, "Surfactant effect on the upconversion emission and decay time of ZrO_2:Yb-Er nanocrystals," Journal of Luminescence, **129**(5), 449-455 (2009)

Contents

List of Figures

LIST OF TABLES

CHAPTER 1

FUNDAMENTALS

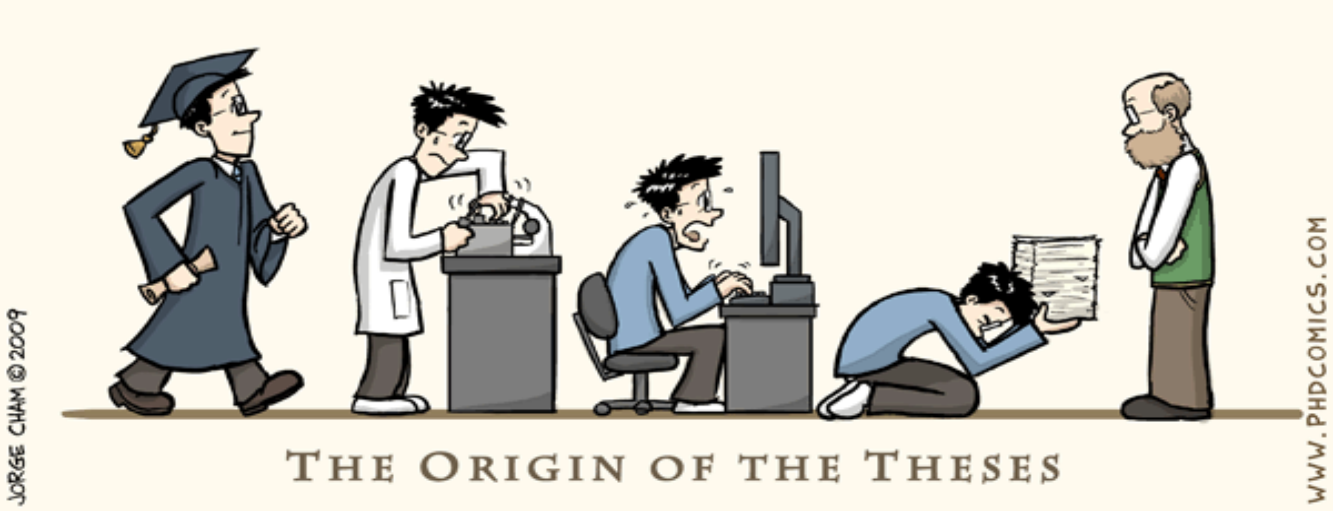

The field of study of nanoscience and technology has shown rapid and exciting progress in the last few years. Chemistry constitutes a major part of nanoscience research; without chemical techniques it is difficult to synthesize or assemble most nanomaterials. Furthermore, many of the properties and phenomena associated with nanomaterials as well as their applications require chemical and physical understanding. This section attempt to briefly explain several topics related to nanomaterials studied in this thesis.

1.1. ELECTRONIC ASPECTS OF PHOSPHORS

We can, as a general rule, divide inorganic solids into 2 classes: those that absorb light (pigmented) and those that emit light (phosphors and solid state lasers). In both cases, we add controlled amounts of a transition metal ion to control the absorption and/or emission properties of that solid. At this point, it should be apparent that emission refers to: (1) absorption of energy (whether by absorption of a photon or other means such as energy from an electron); and (2) reemission of a photon (usually of lower energy, particularly if the original source of energy was a photon). Thus, one view of a phosphor is that it is a "photon-converter".

An inorganic phosphor consists of two parts: (1) the HOST or inorganic compound and (2) the ACTIVATOR or the added transition metal cation. In general, the host needs to be transparent, or non-absorbing, to the radiation source used for the "excitation" process. The activator does just what the name implies, i.e., it "activates" the host. This combination has several advantages, the most important being that both the type and the amount of activator can be precisely controlled. The details concerning those elements that can be used to form the host and those which can be used as activators could be read elsewhere [1].

There are three terms we need to become familiar with, as follows:

- LUMINESCENCE - Absorption of energy with subsequent emission of light
- FLUORESCENCE- Like luminescence, but visible emission

- PHOSPHORESCENCE- Luminescence or fluorescence, but with delayed emission of light

The luminescence is defined as the de-excitation of an atom, molecule, crystal or polymer resulting in the emission of the absorbed energy in the form of photons. This phenomenon occurs in any state of matter, and can occur in organic and inorganic materials that in general are called phosphors, which is the term and meaning to be used in this work. In most inorganic solids, luminescence is associated with impurities and structural defects which act as triggers, such as transition metals, actinides, pure ionic crystals, semiconductors, lanthanides or rare-earths. There are several special cases of the phenomenon of luminescence, for example, the photoluminescence. These differ depending on the excitation energy used to stimulate the emission [2]. The photoluminescence, which is the case of our interest, is the luminescent signal produced by a material after being excited by light.

Luminescence is the general case in which a higher energy photon is absorbed and a lower energy photon is emitted (such a process is called a Stokes process). In this case, the excess energy is absorbed by the solid and appears as lattice vibrational (heat) energy. When the photon has lower energy than excitation then the process is called down-conversion. However, it can also happen that the photon has greater energy than that of excitation; in this case the process is called up-conversion (UC). We shall use fluorescence and luminescence interchangeably, even though, strictly speaking, they are not equivalent. Phosphorescence involves a process where photon absorption occurs but the reemission process is delayed [3]. This delay may be a function of the type of transition metal employed, or a function of the action of solid state defects, including vacancies and the like which "trap" the energy for a time. Note that there are some materials which glow for hours after being excited. This is due to the presence of traps, i.e., lattice defects, put there deliberately during their manufacture. Such phosphors are sometimes called "daylight" phosphors since they can be excited by visible light. Once activated, they will glow for hours.

During the first half of this century, the difference between fluorescence and phosphorescence was a subject actively discussed. Controversy centered on the duration of the after-glow after excitation ceased and on the temperature dependence of the after-glow. However, according to present knowledge, these discussions are now meaningless. In modern usage, light emission from a substance during the time when it is exposed to exciting radiation is called fluorescence, while the after-glow if detectable by the human eye after the cessation of excitation is called phosphorescence. However, it should be noted that these definitions are applied only to inorganic materials; for organic molecules, different terminology is used. For organics, light emission from a singlet excited state is called fluorescence, while that from a triplet excited state is defined as phosphorescence.

The definition of the word *phosphor* itself is not clearly defined and is dependent on the user. In a narrow sense, the word is used to mean inorganic phosphors, usually those in powder form and synthesized for the purpose of practical applications. Single crystals, thin films, and organic molecules that exhibit luminescence are rarely called phosphors. In a broader sense, the word phosphor is equivalent to “solid luminescent material.”

Let us now briefly examine energy dissipation processes of phosphors. The sequence of energy processes that occur within a phosphor include:

a. Absorption of energy (from a variety of sources)
b. Excitation within the activator center to form an excited state
c. Relaxation of the excited state (it is here that energy is lost to the vibrational states of the lattice)
d. Emission of a lower energy photon from the excited state, and relaxation to the original (ground) state

In a phosphor, absorption of energy may occur in the host, or directly in the activator center (the added transition metal ion). But it is the activator center (or site) which becomes excited,

whether by transfer of energy from the host, or not. That is, the activator center absorbs the energy and changes its electronic energy state from a ground state to an excited state. When sufficient energy is absorbed, then the center will become excited, however vibrational modes of the host lattice upon the electronic states of the activator center take place. It is called vibronic coupling, and is caused by phonon wave propagation throughout the host lattice, and interaction at the activator center. (Phonon waves are quantized lattice vibrational waves present in all solids). Remember that unless the host lattice is at 0 °K, then vibrational waves are always present.

From the above description, it should be evident that the electronic excitation-emission transition is a dynamic process which is perturbed by vibronic coupling of the phonon spectrum present in the host lattice. Thus, the host is just as important as the activator center. We can summarize the material in as follows. Essentially, we have treated a phosphor as a one-electron process. The sequences for changes in electronic states are: absorption, excitation and emission. Finally are presented all of the time processes as they relate to phosphors as follows. This is shown in the following:

- Absorption = 10^{-18} s
- Excitation = 10^{-11} s (electronic transition)
- Lattice absorption = 10^{-8} s (vibronic coupling)
- Emission = 10^{-9} to 10^{-2} s (electronic transition)

In view of what we have already stated, it is now easy to see that for emission to occur, vibronic coupling between the excited activator center and the lattice must be minimized, since at least one hundred or more lattice vibrations will occur before the photon is emitted. Otherwise, a radiationless relaxation will occur. In other words, the activator center is not perturbed until it absorbs energy and transforms to an excited state. Once it has done so, then it can relax to an excited state from which emission can occur almost instantaneously. It

is this fact that mandates careful choice of the host used as a basis for preparing the phosphor.

What we can conclude is that the luminescence process involving a phosphor is indeed complicated and is a dynamic process in which the excited center undergoes many perturbations by the lattice during its excited lifetime.

1.2. UP-CONVERSION

A photoexcitation at a certain wavelength in the infrared (NIR) followed by luminescence at a shorter wavelength in the visible (VIS) is called NIR to VIS photon up-conversion (UC). This is a rather unusual process since low energy photons are "converted" to higher energy photons. At least two NIR photons are required to generate one VIS photon. Up-conversion can occur preferably in materials in which multiphonon relaxation processes are not predominant, thus allowing more than one metastable excited state. In rare-earth compounds, the 4*f* or 5*f* electrons are efficiently shielded and thus not strongly involved in the metal-to-ligand bonding. Therefore, electron-phonon coupling to *f-f* transitions is reduced and multiphonon relaxation processes are less competitive. The phenomenon of up-conversion is therefore most common and best studied in materials containing lanthanide ions. The most noteworthy up-conversion processes of these ions involve absorption of two photons on different levels.

1.2.1. UP-CONVERSION PROCESSES

The principle of up-conversion is shown schematically in Figure 1.1. The energy level structure of an ion is shown with ground state A and excited levels B and C. The energy differences between levels C and B and levels B and A are equal. Excitation occurs by radiating the energy which corresponds to this energy difference, so that the ion is excited from A to B. If the life time of level B is not too short, the excitation radiation will excite this ion further from B to C. Finally, emission from C to A may occur. This is known as anti-Stokes emission (energy emission greater than that of excitation). In this way, infrared radiation can be detected

visually. It should be noted that this explanation is idealized; it does not consider energy losses.

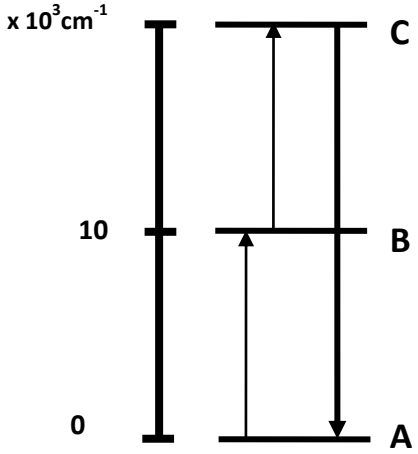

Figure 1.1: The principle of up-conversion. The infrared excitation radiation (10 000 cm^{-1}) is converted into green emission (20000 cm^{-1}).

At present, several up-conversion processes are possible with widely different conversion efficiencies. Their energy schemes are shown in Figure 1.2. Some of the most common processes that generate the UC process are: sequential two-photon absorption by the same ion (ESA, Excited State Absorption), see Figure 1.2a, along with the energy transfer from another ion (ETU = Energy Transfer Up-conversion) Figure 1.2b. As is shown in this figure, an excited ion is relaxed to ground state and its energy promotes other excited ion to a higher state from where it relaxes to the ground state emitting a photon with twice the pumping energy, or simply by a non-radiative relaxation. Other mechanism to produce UC is the avalanche process, shown in Figure 1.2c and d. This process is generated when the excitation beam does not have enough energy to populate the second level from the ground state; however there is a strong pumping absorption by ESA from level 2 to level 3. If for some reason the intermediate level comes to be populated, it absorbs the photon pumping, then promotes the excited electron to a superior level and hence it relaxes to the ground state emitting a photon of higher energy. The population of level 2 is due to two mechanisms. The first mechanism is due to a weak excitation from level 1 involving phonon coupling. Figure 1.2c shows how this level originates from a phonon state (dotted line).

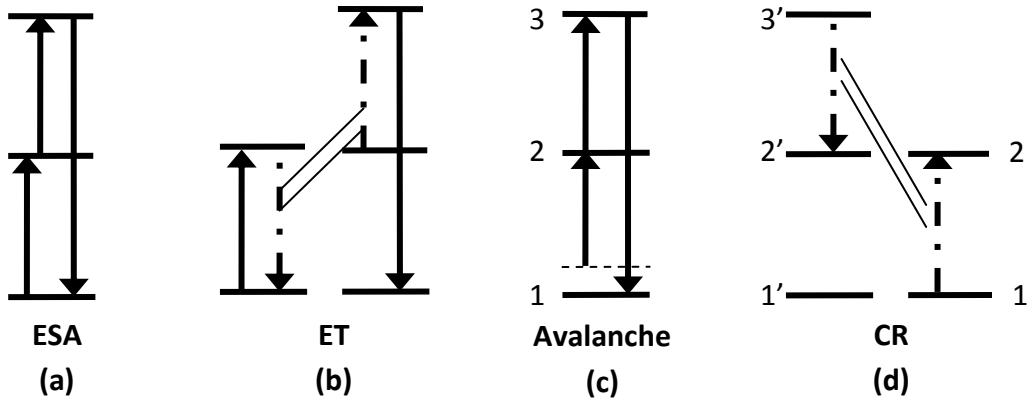

Figure 1.2: Mechanisms for producing the fluorescence up-conversion process. Upward arrows indicate photon absorption pump and down arrows indicate emission. The dotted arrows mean non-radiative relaxation and energy transfer.

The second mechanism involves cross relaxation (CR) at level 3. Part of the population in level 3 is relaxed to level 2 and this energy is transferred to another ion by promoting an electron from the ground state to level 2, see Figure 1.3d. As a result of this, both ions are at level 2. Then, an electron excited to level 3 will produce two electrons in level 2 which in turn will be promoted to level 3 and produce electrons in level 2 by an avalanche generating process. Thus, the level 3 is populated by cross relaxation process along with a strong excited state absorption, resulting in an increased luminescence. For higher-efficient processes it is required energy levels which are resonant with the incoming or outgoing radiation. In addition, the efficiency depends strongly on the choice of the host lattice.

1.2.2. DRAWBACKS

Trivalent rare-earth ions are very suitable for up-conversion processes. This is not surprising in view of their energy level schemes. Such levels often show a wealth of intermediary levels. The positive role of up-conversion in the field of materials has already been outlined above, but there are also negative aspects of up-conversion, viz saturation effects. This is due to the fact that up-conversion implies an upward transition from an intermediate excited state. If we are interested in the emission from this specific intermediate excited state, either in view of

its luminescence or its stimulated emission, we have to consider the fact that up-conversion will decrease the population of this level, so that the intensity of the emission of interest decreases. This will especially be the case for higher activator concentrations and/or high excitation densities (saturation effect).

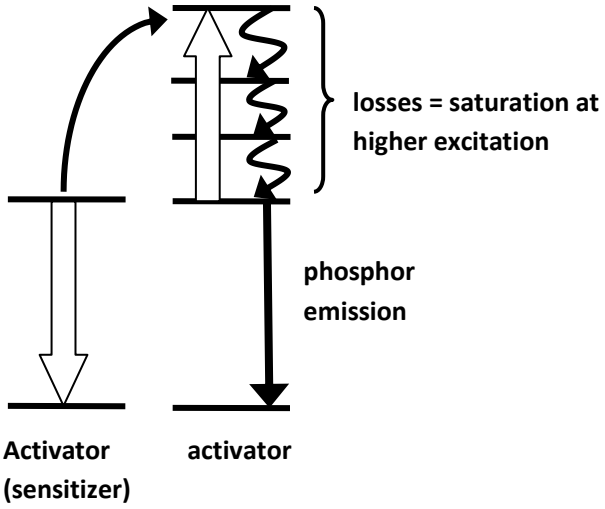

3 *Figure 1.3: Up-conversion as a quenching process of the intermediate level luminescence in a phosphor.*

Part of the saturation effects in projection-television phosphors can be ascribed to an up-conversion process of the type shown in Figure 1.3. Often this type of up-conversion prevents a material from becoming a good laser material. If the stimulated emission radiation is reabsorbed by ions which are still in the excited state, the laser efficiency drops. From Figure 1.3, it becomes clear that the up-conversion process, which is usually called excited state absorption in this case, influences the population inversion in a negative way: considering the two ions in Figure 1.3, the population inversion is complete before the up-conversion occurs, but after up-conversion, the population inversion has decreased to 50%. For this reason excited-state absorption studies are popular among those who investigate potential laser materials.

1.3. LANTHANIDES (RARE-EARTHS)

The lanthanides (rare earths) have found use in regard to phosphors, solid state lasers (which are specialized phosphors) and Anti-Stokes phosphors. Lanthanides have historically been called "rare earths" because it was originally believed that these elements were sporadically distributed in nature. Actually, they are relatively abundant in the Earth's crust, even though only a few ore bodies exist where they constitute the major metallic content. The isolated oxidic product has the feel of Fuller's Earth, hence the use of the term "earth". The name "Lanthanide" comes from the chemical element lanthanum, which is usually included in Group VI of the periodic table, comprised by a total of 15 elements, from atomic number 57 (lanthanum) to 71 (lutetium).

Their chemistry is unique and major difficulties in separating them have been encountered. This behavior relates to their electronic configuration:

$|\text{Xe core}|\ 6s^2 = |\ldots 4d^{10}\ 4f^n\ 5s^2\ 5p^6\ |\ 6s^2$

The optically active electrons involve the 4f shell, buried deep within the Xe-core of electrons. The lanthanides have structures that enable states to be excited to achieve radiative processes. The most commonly used elements are those with a 3^+ oxidation state [4] and their electronic energy levels are in the *4f* orbital, which are distinctive features of rare-earths. These have been extensively studied by Dieke [5] among others [6]. The rare-earth electronic levels are not affected by the environment that surrounds them, because they are covered by the *5s2* and *5p6* electrons. *4f* transitions are very close and exhibit multiple structures derived from electronic interactions, emitting from the excited energy levels by multiple radiative channels.

Because of the shielding effect of the outer closed shells ($5s^2\ 5p^6$), the chemistry of each lanthanide is quite similar to the others. Thus, the separation of each rare earth, free from the others, has proven to be very difficult. Y and Sc are not lanthanides, but their chemical

properties are so nearly identical that they occur in the same ore bodies and have the same separation difficulties as those of the lanthanides. Hence, they are included in the rare earth category.

When a rare earth ion is immersed in a solid, the interaction with the matrix ions produces ion disturbances due to the crystalline field of the host. The most notable evidences of active ion-lattice interaction are:

- The presence of spectral lines that do not exist in the free ion spectra which are originated from allowed transitions by ion-lattice interactions.
- The temperature dependence of both the position of energy levels and the width of the band.
- Radiative transitions are produced, which are explained by the interaction between ion and the phonon energy of the crystal lattice. It is possible to occur that the ion in an excited state relaxes to a lower energy state by phonon coupling.

1.3.1 DEFECTS ON RARE-EARTH DOPED HOSTS

It is unavoidable to find some kinds of defects in solids because oxygen molecules, which are the counter component of the metal oxide, are highly volatile even at low temperatures and are able to escape easily from the solid. More basically, the entropy term of the state requires the existence of defects. Most of the transport phenomena in solids, for example, diffusion of ions, are controlled by defects [7,8].

In general, the point defect in a crystal is a function of temperature, especially at higher temperatures, but not sensitive to environmental oxygen, pressure or temperature. The reaction between gas oxygen and oxygen vacancy in the oxides is easy and fast even at temperatures above 300 ^{o}C. This change may be related to the valence variation of the metal, which forms mixed valence compounds. Electron transfer between different metal cations usually has to be helped by the ligand oxygen, i.e. M-O-M. However, the electron hopping between the rare-earth cations is facilitated because the oxygen vacancy has a positive

charge. Therefore, the correlation between oxygen vacancy and mixed valency is a significant property of rare-earth doped oxides. Based on thermodynamics, the “point defects” in a solid lattice are a natural tendency, due to the fact that increased entropy minimizes the free energy of the system. Surface, interface between two grains or phases, dislocation, and stacking faults are the imperfections of a solid.

1.4. PROPERTIES OF NANOPARTICLES

Nanotechnology is the study of the controlling of matter on an atomic and molecular scale. Generally nanotechnology deals with structures sized between 1 to 100 nanometer in at least one dimension, and involve developing materials or devices within that size. Nanoparticles are entities that appear in-between extended solids and molecules or even in an isolated atom. Properties of nanosolids determined by their shapes and sizes are indeed fascinating, and they form the basis of the emerging field of nanoscience.

Structural miniaturization has indeed provided a new level of freedom, which allows us to tune the physical properties of bulk chunks that are initially nonvariable by simply changing the shape and size of nanoparticles. The effect of size and atomic coordination reduction enhances many properties in a particle. The properties include the lattice contraction (nanosolid densification and surface relaxation), mechanical strength (resistance to both elastic and plastic deformation), thermal stability (phase transition, liquid–solid transition, and evaporation), and lattice vibration (acoustic and optical phonons). They also cover photon emission and absorption (blue shift), electronic structures (core-level disposition and work function modulation), magnetic modulation, dielectric suppression, and activation energies for atomic dislocation, diffusion, and chemical reaction.

The bond order of an atom is lost at a site surrounding a defect or near the edge of a surface in which the coordination reduction (deviation of bond order, length, and angle) distributes randomly. Bond order loss causes remaining bonds of the under-coordinated atom to contract spontaneously and enhances the density of charge, mass, and energy in the relaxed

region. The energy density rise in the relaxed region perturbs the Hamiltonian and the associated properties such as the band gap width, core-level energy, Stokes shift (electron–phonon interaction), and dielectric susceptibility. On the other hand, bond order loss lowers the cohesive energy of the under-coordinated atom, which dictates the thermodynamic process such as self-assembly growth, atomic vibration, thermal stability, and activation energies.

Chemical kinetics of particle surface and surface area increment are the first effects resulting from nano-sized particles. *Chemical kinetics* depends partially on surface available for contact between the reactants, in particular solid ones in heterogeneous systems. The fraction of the atoms or the molecules located at particle surface plays a great role, since these are more active than those inside the solid particle because of the disperse surrounding, which leads to easy bonding with the contacting materials and causes various changes in particle properties. On the other hand, as size reduction of a solid particles advances, the specific *surface area* increases, generally in inverse proportion to particle size. The increase in specific surface area directly influences such properties as the solution and reaction rates, thus it is one of major reasons for the unique properties of the nanoparticles.

1.5. SYNTHESIS AND PREPARATION FOCUSED ON NANOPARTICLES

Since 1980's, ultrafine particles ranging from nanometer to sub-micrometer scale have involved attention because of their remarkably different physical and chemical properties from those of bulk materials. The origin of the change in properties has been explained by the quantum size effect and the surface effect.

One of the main ways to synthesize and prepare fine particles is the buildup method. The buildup method means growing particles from an atom, a molecule, or an ion, and it is possible to synthesize small particles. In addition, this method is suitable to get particles of high quality because is possible to use high purity starting materials. In this section, synthesis and preparation of fine oxide nanoparticles are reviewed.

1.5.1. HYDROTHERMAL METHOD

Hydrothermal synthesis can be defined as a method of synthesis of single crystals which depends on the solubility of minerals in hot water under high pressure. The crystal growth is performed in an apparatus consisting of a steel pressure vessel called autoclave, in which a nutrient is supplied along with water. A gradient of temperature is maintained at the opposite ends of the growth chamber so that the hotter end dissolves the nutrient and the cooler end causes seeds to take additional growth. Hydrothermal synthesis is commonly used to grow synthetic quartz, gems and other single crystals with commercial value.

Possible advantages of the hydrothermal method over other types of crystal growth include the ability to create crystalline phases which are not stable at the melting point. Also, materials which have a high vapour pressure near their melting points can also be grown by the hydrothermal method. A large number of compounds belonging to practically all classes have been synthesized under hydrothermal conditions: elements, simple and complex oxides, tungstates, molybdates, carbonates, silicates, germanates etc. The method has proved to be extremely efficient in the search for new compounds with specific physical properties.

In this method, high temperature and high pressure water is used as transfer medium of heat, pressure, and mechanical energy. Water also works as a solvent that dissolves and recrystallizes the solid materials, and as a reagent acting as a mineralizer. These properties have been used in processing of inorganic materials in the preparation of single crystals and particularly of fine powders with nanosized to submicron particles [9]. Not only water (hydrothermal synthesis), but also ammonia or certain organic solvents are utilized as reaction media, and this is generally called a solvothermal method.

The hydrothermal method composes of three types of processes: hydrothermal synthesis, hydrothermal oxidation, and hydrothermal crystallization. Hydrothermal synthesis is used to synthesize oxides from their component salts, oxides or hydroxides. Pressure, temperature, and mineralizer concentration control the size and morphology of the particles. Forced

hydrolysis of solutions is effective to obtain uniform and fine particles. For example, fine cerium oxide particles were prepared from a tetravalent cerium salt solution ($CeSO_4 \cdot 4H_2O$, $(NH_4)_4Ce(SO_4)_4 \cdot 2H_2O$, and $(NH_4)_2Ce(NO_3)_6$) in low concentrations at low temperature aging in a sealed vessel [10-13]. The metal ions are solvated by water molecules that can be deprotonated to give hydroxide or oxide particles. This method is very sensitive to the concentration of precursors, temperature, and pH value of solution. In the hydrothermal oxidation, fine oxide particles can be prepared from metals, alloys, and intermetallic compounds by oxidation at high temperature and pressure solvent, and as a result, the starting metals are directly changed into fine oxide powders. For example, solvothermal oxidation of cerium metal in 2- methoxyethanol at 473-523 K yields ultrafine cerium particles (ca. 2 nm) [14].

Hydrothermal crystallization is the most extensively used method in hydrothermal synthesis and crystal growing. Precipitation and crystallization from aqueous solutions under elevated temperature and high pressure conditions are performed as the following process. The autoclave is thermally quenched and the obtained crystalline powder products are washed and dried. Using the hydrothermal crystallization method, a number of yttria [15,16] ceria [17-22], and ZnO [23,24] nanoparticles have been prepared. The obtained particles sizes ranges from 3 nm to 0.8 μm in size, depending on the reaction temperature, crystallization time, and starting materials.

1.5.2. SOL-GEL METHOD

The sol-gel process, also known as chemical solution deposition, is a wet-chemical technique widely used in the fields of materials science and ceramic engineering. Such methods are used primarily for the fabrication of materials (typically a metal oxide) starting from a chemical solution (or sol) which acts as the precursor for an integrated network (or gel) of either discrete particles or network polymers. Typical precursors are metal alkoxides and metal chlorides, which undergo various forms of hydrolysis and polycondensation reactions.

In the sol-gel method, metal alkoxides are generally dissolved in an alcohol solvent (methanol, ethanol, or iso-propanol are frequently used) and addition of water causes hydrolysis. This reaction is followed by a series of condensation reactions between hydroxide groups. Mixed oxide gels can be produced by mixing plural alkoxides. This process is efficient to obtain fine powders, but has the disadvantage of the high costs of metal alkoxides. Preparation of fine particles by pyrolysis of a precursor gel is often included in the category of the sol-gel method involving a chelating agent. In some cases, this method is called combustion synthesis. A variety of organic acids are used as chelating agents such as citric acid, tartaric acid, malonic acid, oxalic acid, and acetic acid [25].

In sol-gel chemical procedure, the “sol” (or solution) gradually evolves towards the formation of a gel-like diphasic system containing both a liquid phase and solid phase whose morphologies range from discrete particles to continuous polymer networks. In the case of the colloid, the volume fraction of particles (or particle density) may be so low that a significant amount of fluid may need to be removed initially for the gel-like properties to be recognized. Removal of the remaining liquid (solvent) phase requires a drying process, which is typically accompanied by a significant amount of shrinkage and densification. The rate at which the solvent can be removed is ultimately determined by the distribution of porosity in the gel. The ultimate microstructure of the final component will clearly be strongly influenced by changes imposed upon the structural template during this phase of processing. Afterwards, a thermal treatment, or firing process, is often necessary in order to favor further polycondensation and enhance mechanical properties and structural stability via final sintering, densification and grain growth. One of the distinct advantages of using this methodology as opposed to the more traditional processing techniques is that densification is often achieved at a much lower temperature.

The precursor sol can be either deposited on a substrate to form a film, cast into a suitable container with the desired shape (e.g., to obtain monolithic ceramics, glasses, fibers, membranes, aerogels), or used to synthesize powders (e.g., microspheres, nanospheres). The

sol-gel approach is a cheap and low-temperature technique that allows for the fine control of the product's chemical composition. Even small quantities of dopants, such as organic dyes and rare earth elements, can be introduced in the sol and end up uniformly dispersed in the final product. It can be used in ceramics processing and manufacturing as an investment casting material, or as a means of producing very thin films of metal oxides for various purposes. Sol-gel derived materials have diverse applications in optics, electronics, energy, space, (bio)sensors, medicine (e.g., controlled drug release), reactive material and separation (e.g., chromatography) technology.

1.6. SURFACTANTS

Surfactants are wetting agents that reduce the surface tension of a liquid by adsorbing at the liquid-gas interface, allowing easier spreading, and abating of the interfacial tension between two liquids. The term surfactant is a blend of surface active agent [26]. Surfactants are usually organic compounds that are amphiphilic, meaning they contain both hydrophobic groups (their tails) and hydrophilic groups (their heads). Therefore, they are soluble in both organic solvents and water. They also reduce the interfacial tension between oil and water by adsorbing at the liquid-liquid interface. Many surfactants can also assemble in the bulk solution into aggregates. Examples of such aggregates are vesicles and micelles. The concentration at which surfactants begin to form micelles is known as the critical micelle concentration (CMC). When micelles form in water, their tails form a core that can encapsulate an oil droplet, and their (ionic/polar) heads form an outer shell that maintains favorable contact with water. When surfactants assemble in oil, the aggregate is referred to as a reverse micelle. In a reverse micelle, the heads are in the core and the tails maintain favorable contact with oil. Thermodynamics of the surfactant systems are of great importance, theoretically and practically [27]. This is because surfactant systems represent systems between ordered and disordered states of matter. Surfactant solutions may contain an ordered phase (micelles) and a disordered phase (free surfactant molecules and/or ions in the solution).

A systematic study reported that surfactant helps to reduce residual contaminants, avoid aggregation, control crystallite size, and in the proper concentration enhance the up-converted emitted signal from phosphors [28]. Thus using of surfactant during preparation of particles should be considered.

A surfactant can be classified into four primary groups by the presence of formally charged groups in its head. A non-ionic surfactant has no charge groups in its head. The head of an ionic surfactant carries a net charge. If the charge is negative, the surfactant is more specifically called anionic; if the charge is positive, it is called cationic. If a surfactant contains a head with two oppositely charged groups, it is termed zwitterionic (dual charge).

1.6.1. CTAB

Nanoparticles of ZrO_2 were synthesized using CTAB (cetyl trimethyl ammonium bromide) as surfactant, $C_{19}H_{42}BrN$. This type of surfactant is formed by two types of groups, a hydrophobic and hydrophilic. The hydrophilic part, which binds to water molecules, is an amine and the hydrophobic part avoiding the water is the hydrocarbon chain. The representation of the formula and the micelle is shown in Figure 1.4. This surfactant is cationic.

Currently there are studies on the synthesis of various types of nanoparticles using CTAB as surfactant, including mentioned metal oxide nanoparticles as ZrO_2-Y_2O_3, TiO_2 and ZrO_2 [29-31], the synthesis of Au nanoparticles [32] and semiconductor nanoparticles such as ZnS:Mn [33]. These materials have been synthesized by the method of micelles or inverse micelles obtaining different morphologies, sizes, etc. However, there is very little information in the literature on a detailed study on the effect of surfactant on the optical properties of nanoparticles.

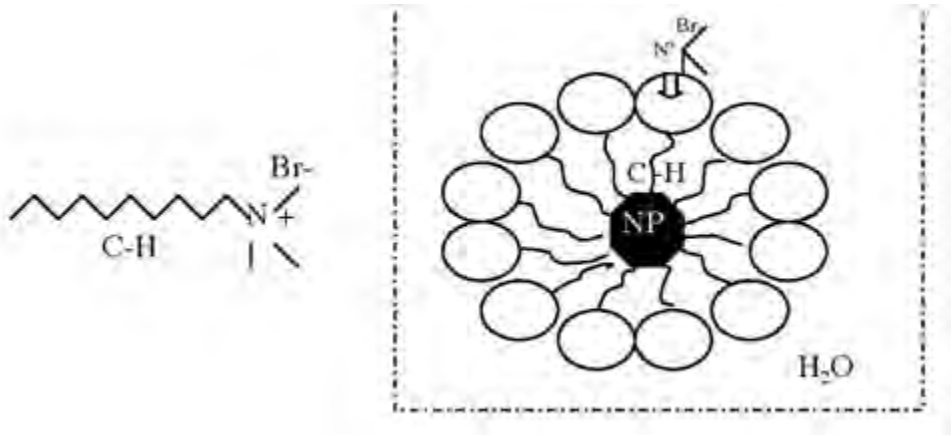

4 *Figure 1.4: CTAB molecule and schematic structure of a spherical micelle.*

1.6.2. PLURONIC F-127

Pluronic F127 is a difunctional block copolymer surfactant terminating in primary hydroxyl groups, as well as a nonionic surfactant that is 100% active and relatively nontoxic. The nonionic surfactants are characterized by having no charge on the hydrophilic part. This surfactant is a three-block copolymer, PEO-PPO-PEO, where PEO means poly (ethylene oxide) and PPO means poly (propylene oxide). The PEO part is hydrophilic and PPO is hydrophobic. When making this type of surfactants in a water suspension with solid particles PPO polymer chain is adsorbed on the solid surface and the PEO polymer chains are adsorbed water molecules.

Pluronics is the trade name for poloxamers [34]. Poloxamers are nonionic triblock copolymers composed of a central hydrophobic chain of polyoxypropylene (poly(propylene oxide)) flanked by two hydrophilic chains of PEO or polyoxyethylene (poly(ethylene oxide)). The word "poloxamer" was coined by the inventor, Irving Schmolka, who received the patent for these materials in 1973 [35]. Because the lengths of the polymer blocks can be customized, many different poloxamers exist with slightly different properties. For the generic term "poloxamer", these copolymers are commonly named with the letter "P" (for poloxamer) followed by three digits, the first two digits x 100 give the approximate molecular mass of the polyoxypropylene core, and the last digit x 10 gives the percentage polyoxyethylene content

(e.g., P407 = Poloxamer with a polyoxypropylene molecular mass of 4,000 g/mol and a 70% polyoxyethylene content). For the Pluronic trade name, coding of these copolymers starts with a letter to define its physical form at room temperature (L = liquid, P = paste, F = flake (solid)) followed by two or three digits, The first digit (two digits in a three-digit number) in the numerical designation, multiplied by 300, indicates the approximate molecular weight of the hydrophobe; and the last digit x 10 gives the percentage polyoxyethylene content. In the example given, poloxamer 181 (P181) = Pluronic L61.

Currently there are studies on the synthesis of various types of nanoparticles using Pluronic as surfactant and related to luminescent materials, such as ZnO and SiO_2 [36-38].

1.7. REFERENCES

[1] R. C. Ropp, “Luminescence and the Solid State”, Studies in Inorganic Chemistry series 21, Elsevier B.V., Amsterdam, Netherlands (2004)

[2] Weber, M.J., “Phosphors, light emitting diodes, and scintillators: Applications of photo-, cathodo-, electro- and radioluminescence”, Society of Photo-Optical Instrumentation Engineers, Bellingham, WA. (1998)

[3] Reuven Chen and S.W.S. McKeever, “Theory of Thermoluminescence and Related Phenomena”, World Scientific, (1997)

[4] G.R. Choppin, “Chemical properties of the rare earth elements”, in Lanthanide Probes in Life, J.C.G. Bunzli and G.R. Choppin (eds.), Chemical and Earth Sciences, Elsevier, Amsterdam, p.1, (1989)

[5] G.H. Dieke, “Spectra and Energy Levels of Rare Earth Ions in Crystals”, Wiley Interscience, New York (1968)

[6] Boyn, R., 4f-4f Luminescence of Rare-Earth Centers in II-VI Compounds. Phys. Status Solidi B, **148**, 1, p.11, (1988)

[7] Z.M. Jarzebski, translated by B. Grzybowska-Swierkosz, “Oxide Semiconductors”, Pergamon Press, Oxford, (1973)

[8] F.A. Kroeger, “The Chemistry of Imperfect Crystals”, North-Holland Publishing, Amsterdam, (1964)

[9] M. Yoshimura and S. Somiya, “Hydrothermal synthesis of crystallized nano-particles of rare earth-doped zirconia and hafnia”, Mater. Chem. Phys. **61**, 1 (1999)

[10] W.P. Hsu, L. Rönnquist, and E. Matijevi, “Preparation and properties of monodispersed colloidal particles of lanthanide compounds. 2. Cerium(IV)”, Langmuir **4**, 31 (1988)

[11] M. Hirano, Y. Fukuda, H. Iwata, Y. Hotta, and M. Inagaki, “Preparation and Spherical Agglomeration of Crystalline Cerium(IV) Oxide Nanoparticles by Thermal Hydrolysis”, J. Am. Ceram. Soc. **83**, 1287 (2000)

[12] M. Hirano and M. Inagaki, “Preparation of monodispersed cerium(IV) oxide particles by thermal hydrolysis: influence of the presence of urea and Gd doping on their morphology and growth”, J. Mater. Chem., **10**, 473 (2000)

[13] M. Hirano, T. Miwa, and M. Inagaki, “Low-Temperature Direct Synthesis of Nanoparticles of Fluorite-Type Ceria–Zirconia Solid Solutions by “Forced Cohydrolysis” at 100°C”, J. Solid State Chem. **158**, 112 (2001)

[14] M. Inoue, M. Kimura, and T. Inui, “Transparent colloidal solution of 2 nm ceria particles”, Chem. Commun. **957** (1999)

[15] H. Tomaszewski, H. Weglaz, and R. De Gryse, “Crystallization of yttria under hydrothermal conditions”, J. Eur. Ceram. Soc. **17**, 403–406 (1997)

[16] P.K. Sharma, M.H. Jilavi, R. Nass, and H. Schmidt, “Seeding Effect in Hydrothermal Synthesis of Nanosize Yttria”, J. Mater. Sci. Lett. **17**, 823 (1998)

[17] Y.C. Zhou and M.N. Rahaman, “Hydrothermal synthesis and sintering of ultrafine CeO2 powders”, J. Mater. Res. **8**(7), 1680 (1993)

[18] W. Chengyun, Q. Yitai, X. Yi, W. Changsui, Y. Li, and Z. Guiwen, “A novel method to prepare nanocrystalline (7 nm) ceria”, Mater. Sci. Eng. B **39**, 160 (1996)

[19] M. Hirano and E. Kato, “The hydrothermal synthesis of ultrafine cerium(IV) oxide powders”, J. Mater. Sci. Lett. **15**(14), 1249 (1997)

[20] M. Hirano and E. Kato, “Hydrothermal Synthesis of Cerium(IV) Oxide”, J. Am. Ceram. Soc. **79**, 777 (1996)

[21] Y. Hakuta, S. Onai, H. Terayama, T. Adschiri, and K. Arai, “Production of Ultra-fine Ceria Particles by Hydrothermal Synthesis Under Supercritical Conditions”, J. Mater. Sci. Lett. **17**, 1211 (1998)

[22] M. Hirano and E. Kato, “Hydrothermal Synthesis of Nanocrystalline Cerium(IV) Oxide Powders”, J. Am. Ceram. Soc. **82**, 786 (1999)

[23] E. De la Rosa, S. Sepulveda-Guzman, B. Reeja-Jayan, A. Torres, P. Salas, N. Elizondo, and M. J. Yacaman, "Controlling the growth and luminescence properties of well-faceted ZnO nanorods," Journal of Physical Chemistry C **111**, 8489-8495 (2007)

[24] B. Reeja-Jayan, E. De la Rosa, S. Sepulveda-Guzman, R. A. Rodriguez, and M. J. Yacaman, "Structural characterization and luminescence of porous single crystalline ZnO nanodisks with sponge-like morphology," Journal of Physical Chemistry C **112**, 240-246 (2008)

[25] S. Roy, W. Sigmund, and F. Aldinger, "Nanostructured yttria powders via gel combustion", J. Mater. Res. **14**, 1524 (1999)

[26] M.J. Rosen, "Surfactants and Interfacial Phenomena" John Wiley & Sons (3rd ed.), Hoboken, New Jersey, (2004)

[27] S.A. Baeurle, J. Kroener, "Modeling Effective Interactions of Micellar Aggregates of Ionic Surfactants with the Gauss-Core Potential", J. Math. Chem. **36**, 409–421 (2004)

[28] T. Lopez-Luke, E. De la Rosa, P. Salas, C. Angeles-Chavez, L. A. Diaz-Torres, and S. Bribiesca, "Enhancing the up-conversion emission of ZrO2 : Er3+ nanocrystals prepared by a micelle process," Journal of Physical Chemistry C 111, 17110-17117 (2007)

[29] C.Y. Tai, and B.Y. Hsiao, "Characterization of zirconia powder synthesized via reverse microemulsion precipitation", Chem. Eng. Commun. **192**(10-12), 1525-1540 (2005)

[30] X.L. Fang, and C.F. Yang, "An experimental study on the relationship between the physical properties of CTAB/hexanol/water reverse micelles and ZrO_2-Y_2O_3 nanoparticles prepared", J. Colloid Interface Sci. **212**(2), 242-251 (1999)

[31] I. Alessandri, L. Armelao, E. Bontempi, G. Bottaro, L.E. Depero, F. Poli, and E. Tondello, "Sol-gel synthesis and characterization of lamellar mesostructured titania films", Materials Science & Engineering C-Biomimetic and Supramolecular Systems **25**(5-8), 560-564 (2005)

[32] C.M. Aguirre, T.R. Kaspar, C. Radloff, and N.J. Halas, "CTAB mediated reshaping of metallodielectric nanoparticles", Nano Lett. **3**(12), 1707-1711 (2003)

[33] X.B. Yu, L.Z. Yang, S.P. Yang, and P.L. Zhou, "Morphological control and photoluminescence of ZnS:Mn microstructure", J. Mater. Res. **22**(5), 1207-1213 (2007)

[34] BASF Corporation Website, "BASF-Product information the chemicals catalog-Pluronics",http://worldaccount.basf.com/wa/NAFTA~en_US/Catalog/ChemicalsNAFTA/pi/BASF/Brand/pluronic. Retrieved 2008-12-09

[35] US patent 3740421

[36] L. A. Rocha, J. M. A. Caiut, Y. Messaddeq, S. J. L. Ribeiro, M. A. U. Martines, J. D. Freiria, J. Dexpert-Ghys, and M. Verelst, "Non-leachable highly luminescent ordered mesoporous SiO_2 spherical particles," Nanotechnology **21**(2010)

[37] J. Li, X. Zhao, C. Yan, and L. Yijing, "Electroluminescence of ZnO nanocrystalline particles annealed from mesoporous precursors," Materials Chemistry and Physics **107**, 177-182 (2008)

[38] C. Yan, Z. Chen, and X. Zhao, "Enhanced electroluminescence of ZnO nanocrystalline annealing from mesoporous precursors," Solid State Communications **140**, 18-22 (2006)

CHAPTER 2

LUMINESCENCE PROPERTIES OF

$ZrO_2:Yb^{3+}$, Er^{3+} NANOCRYSTALS

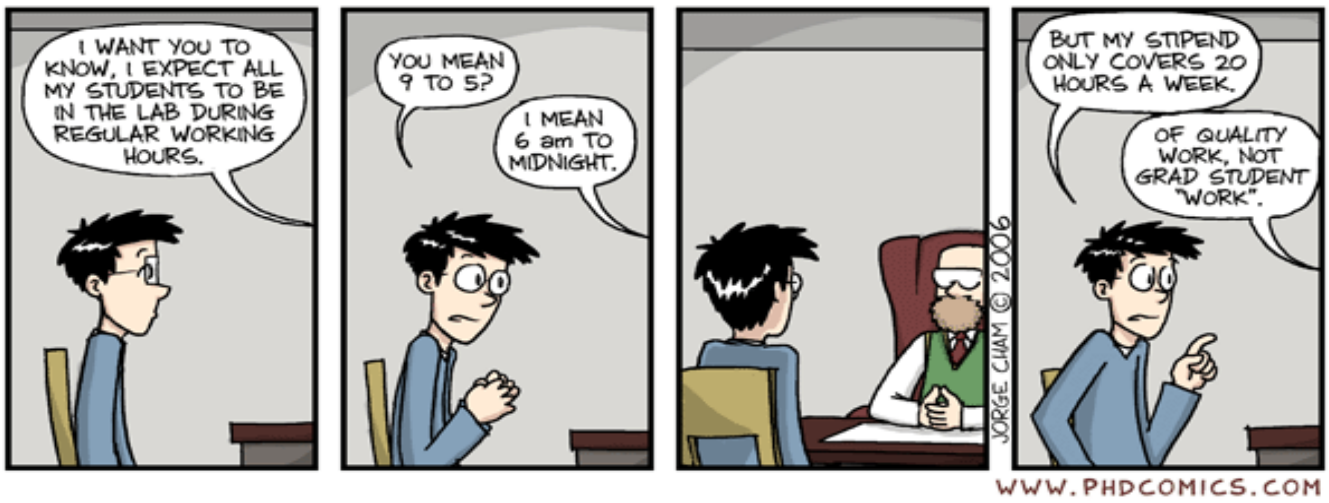

2.1. INTRODUCTION

The importance of research in up-conversion luminescence materials still attracts attention, renewed with the advent of nanophosphor. Recently, it has been reported up-conversion emission, red and green, in Er^{3+}–Yb^{3+} co-doped cubic nanocrystalline yttrium oxide (Y_2O_3:Yb^{3+}–Er^{3+}) [1,2] and by up-conversion with ZrO_2:Er^{3+} nanocrystals [3-5]. In this last case, it was shown tuning capability of the red and green emission band either by controlling the ion concentration or by controlling the pumping wavelength. The study of luminescence properties in zirconium oxide nanocrystals is worthy of attention. The low phonon energy of ZrO_2 opens up the possibility of higher efficient luminescence of active ions incorporated into the host [6]. ZrO_2 has been studied with different rare earth ions, such as Yb^{3+}–Tm^{3+} [7], Yb^{3+}–Ho^{3+} [8], Er^{3+} and Yb^{3+}–Er^{3+} [28]. Furthermore, it has been reported a dependence of the luminescence efficiency on particle size, reduction of the organic remnants and the phonon energy of the host [9,17,34]. In this section, the luminescence properties of the ZrO_2: Yb^{3+}-Er^{3+} prepared samples are studied, by which we determined the concentration region that generates the maximum intensity. Furthermore, the effect of the phenomena of cross-relaxation (CR) and energy back transfer (EBT) on the emission color are modeled and explained. Finally, some enhancement performances are particularly considered.

2.2 EXPERIMENTAL PROCEDURE

(a) Sample Preparation

The synthesis of Yb^{3+}-Er^{3+} codoped ZrO_2 nanophosphors were prepared by sol-gel and micelle methods**.** In both cases, all chemical used were reactive grades and supplied by Aldrich Inc. The samples were obtained using zirconium n-propoxide (ZP), erbium nitrate $(Er(NO)_3)_3 \cdot 5H_2O$) and ytterbium chloride ($YbCl_3 \cdot 6H_2O$) as precursors. All components were mixed in a solution of ethanol (40 mol), hydrochloric acid (0.3 mol) and nitric acid (0.9 mol) at room temperature applying vigorous stirring. The mixed solution was stirred for 20 min and subsequently CO_2-free distilled water in a molar ratio of 1:4 was added wisely to manipulate the oxalation process. Samples were aged at 70^{o}C for 15 ~ 18 h and then grinded in an agate mortar to obtain a fine powder. All this process was carried out under ambient pressure by

using open containers. Further, samples were dried at 300^{o}C for 2 h, dehydrated at 500^{o}C for 2 h and annealed at 1000^{o}C for 5 h applying an incremental temperature of 5^{o}C/min.

In the micelle method, Pluronic F-127 was added to the solution at molar ratio (PLURONIC/ZrO_2) of 0.0082. After that, samples were stirred 1 h and carried to hydrothermal treatment at 80^{o}C for 24 h by using hermetic 100 ml Pyrex containers in which 30-40% were occupied by the solution. The autoclave allowed a natural cooling and the gel was washed twice with absolute ethanol. All samples were annealed at 1000^{o}C, some samples were removed from the furnace as soon as the final temperature was reached (annealed 0 min (0')) and some samples were kept there for 5h. In all cases, the heating rate was 5^{o}C/min and stayed at 300 and 500^{o}C for 2 h. This method will be compared with sol-gel method as to determine which one from both presents better luminescent characteristics.

Yb^{3+}-Er^{3+} samples were synthesized with the addition of surfactant at molar ratio (Mrp= PLURONIC/ZrO_2) of 0.0082 and 0, though 0.01 was also used for Er doped samples (Mrp= 0, 0.0082, 0.01). Studied concentrations 0.2 mol% Er^{3+} and 2-1 mol% Yb^{3+}-Er^{3+} ZrO_2 samples were considered.

(b) Structural Characterization

The X-ray diffraction (XRD) patterns were obtained using a SIEMENS D-5005 equipment provided with a Cu tube with Kα radiation at 1.5405 Å, scanning in the 20^{o}-70^{o} 2θ range with increments of 0.02^{o} and a sweep time of 2 s. Transmission electron microscopy (TEM) were performed in a Tecnai G^2 F30 S-Twin transmission electron microscope operating at 300 kV. The microscope is equipped with a Schottky-type field emission gun and an S-Twin objective lens (Cs = 1.2 mm; Cc = 1.4 mm; point-to-point resolution, 0.20nm). The Fourier transform infrared (FTIR) spectra were obtained using a Spectrophotometer Spectrum BX, FTIR system from Perkin-Elmer with a DTGS detector at 4 cm^{-1} spectral resolution and Beer-Norton anodization. Measurements were performed in the attenuated total reflectance (ATR) mode using 100 mg of nanophosphor covering the whole active area of the ATR device. The spectrum was obtained in the medium-infrared region from 1000 to 4000 cm^{-1} with 20 scans

per spectra. Before measurements, the equipment was calibrated by verifying that power energy was 80% and spectral response was calibrated with a polystyrene film as a reference.

(c) Photoluminescence characterization

The photoluminescence (PL) characterization was performed using a CW semiconductor laser diode with a 350 mW pumping source centered at 970 nm. The luminescent emission was analyzed with a Spectrograph SpectraPro 2300i. The system was PC controlled with SpectraSense software. Luminescence lifetime were performed using a chopper SR540 (Stanford) and a Tektronix TDS 3052B oscilloscope. All measurements were done at room temperature. Samples were supported in 1 mm capillary tubes in order to guarantee the same quantity of excited material. Special care was taken to maintain the alignment of the set up in order to compare the intensity of the up-converted signal between different characterized samples. A schematic of the experimental arrangement is shown in Figure 2.1.

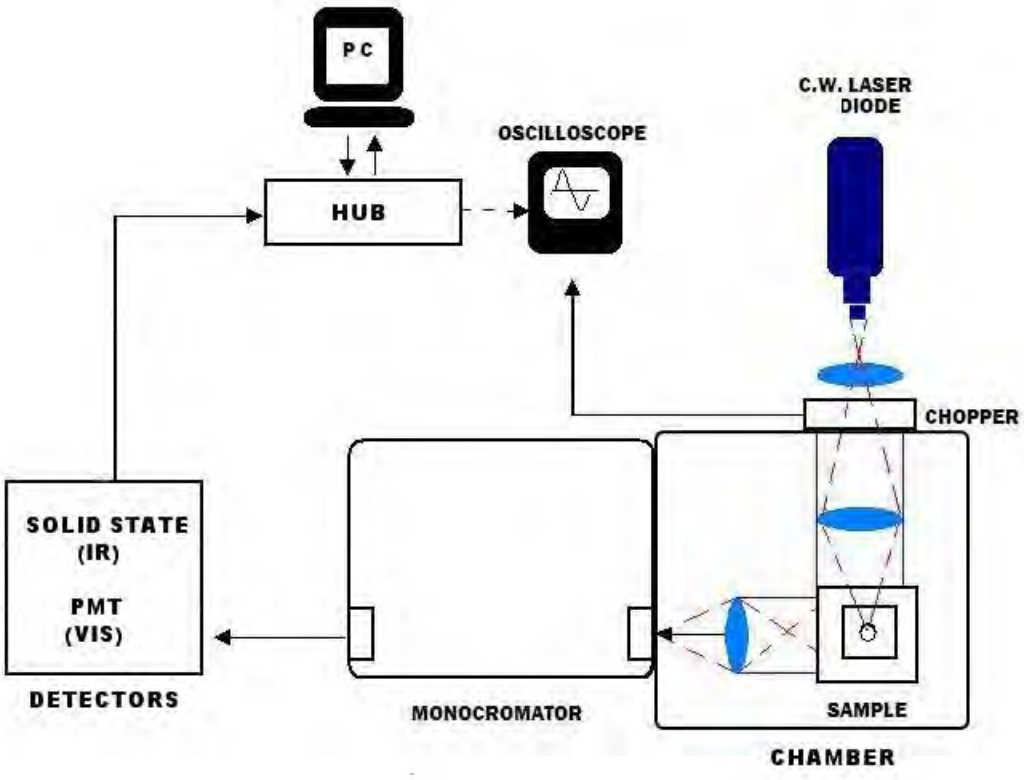

Figure 2.1: Experimental PL set-up.

2.3. STRUCTURAL CHARACTERIZATION

The crystalline structure of bulk ZrO_2 depends on the annealing temperature (T_a) and shows three stable crystalline phases: monoclinic (*m*) structure at $T_a < 1170^oC$, tetragonal (*t*) structure between 1170 and 2370^oC and cubic (*c*) structure at $T_a > 2370^oC$. Both optical and mechanical properties are function of the crystalline phase composition. Nevertheless, the metastable *t* phase has been synthesized at 500^oC by using the sol-gel. The diffraction pattern of undoped ZrO_2 nanocrystals is dominated for the monoclinic structure. The characteristic peaks of this structure are $(1,1,0)_m$, $(-1,1,1)_m$ and $(1,1,1)_m$ according to the standard JCPDS 37-1484.

Samples were synthesized by a hydrothermal method with the addition of surfactant (pluronic F-127) in order to determine a correlation between particle size, annealing time and surfactant concentration on the emission intensity. The effect of sensitizer on structure was evaluated. It induces an increment on the tetragonal phase larger than 90% and 70% for doped and codoped, respectively, for an optimum molar ratio of 0.0082.

2.3.1. STRUCTURE OF ZrO_2: Yb^{3+}, Er^{3+}

The crystalline phase composition for ZrO_2:Yb^{3+}/Er^{3+} nanophosphor depends on the ion concentration. The XRD patterns for characteristic samples under study are shown in Figure 2.2. For undoped samples, the pattern is dominated by $(-1,1,1)_m$ and $(1,1,1)_m$ diffraction peaks characteristics of the monoclinic structure. Pure tetragonal structure with characteristic peak $(1,0,1)_t$ was obtained for ZrO_2:Yb^{3+}/Er^{3+} (2/1 mol%) sample, and a mixture of monoclinic and tetragonal phase was observed for total concentration lower than 3 mol% of dopant ions. For a higher concentration, a mixture of tetragonal and cubic phase was observed. 33 wt% cubic phase was obtained for ZrO_2:Yb^{3+}/Er^{3+} (4/1 mol%) sample and pure cubic was observed for total concentration higher than 5 mol%. Notice that dominant peak in both tetragonal and cubic are the same. Tetragonal phase can be identified by the characteristic double peak $(2,0,0)_t$ and $(0,1,1)_t$ at 34.92^o and 35.40^o, and single peak $(2,0,0)_c$ at 35.13^o for cubic crystalline structure. Even though phase composition changes with the increase of Er^{3+} ion, experimental results show that Yb^{3+} ion is dominant to stabilize crystalline phase. Phase composition was

obtained from the Rietveld analysis of the XRD patterns and is resumed in Table 2.1 along with all characteristic parameters including crystallite size. The noticeable small width of diffraction peaks indicates a uniform distribution of the average crystallite size. For ZrO_2:Yb^{3+}-Er^{3+} doped samples the average crystallite size was 70 nm for tetragonal phase, that is the dominant phase for most of samples under study. The changes in lattice parameters, also observed from the Rietveld analysis of XRD, indicate the substitution of Yb-Er in Zr^{4+}. Such changes are partially due to the difference in the Zr^{4+} ionic radii with both Yb and Er, and partly due to charge compensation by the difference on valence.

Table 2.1: Crystalline phase composition, lattice parameters and crystallite size for some typical samples.

Dopant composition Yb/Er (mol%)	Phase composition (wt%)	Lattice parameters (Å)			Crystallite size (nm)
		a_o	b_o	c_o	
0/0	Tetragonal (3)	3.585	3.585	5.210	17.1
	Monoclinic (97)	5.147	5.198	5.324	48.8
2/1	Tetragonal (100)	3.602	3.602	5.172	77.8
4/1	Tetragonal (67)	3.607	3.607	5.160	49.1
	Cubic (33)	5.124	5.124	5.124	79.9
10/1	Cubic (100)	5.126	5.126	5.126	53.6

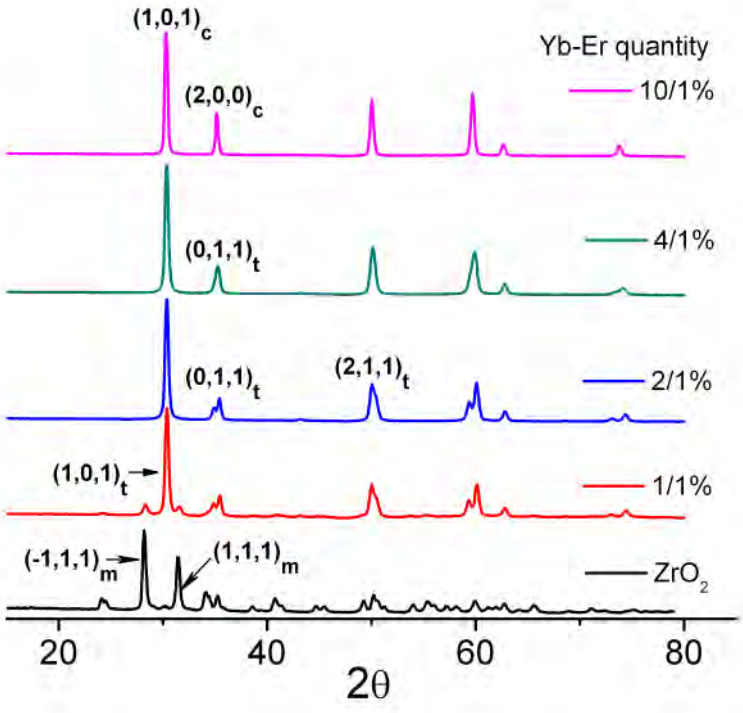

Figure 2.2: X-ray diffraction of undoped and codoped ZrO_2:Yb^{3+}-Er^{3+} nanocrystals.

2.3.2. STRUCTURE OF ZrO_2: Yb^{3+}, Er^{3+} WITH PLURONIC F-127

The XRD patterns of ZrO_2:Yb^{3+}–Er^{3+} and ZrO_2:Er^{3+} nanocrystals annealed at 1000°C are shown in Figure 2.3. The phase composition was estimated by using the expression [10]:

$$C_m = \frac{I_m(-1,1,1) + I_m(1,1,1)}{I_m(-1,1,1) + I_m(1,1,1) + I_t(1,0,1)} \qquad (2.1)$$

$$C_t = 1 - C_m$$

where *m* and *t* stand for the monoclinic and tetragonal phase of the host and *I* stand for the integrated intensity of each diffraction peak. The phase composition of codoped and doped samples annealed for 5 h without surfactant (Figure 2.3 b and d) is dominated by the tetragonal (60 wt%) and the monoclinic (96 wt%) crystalline phase, respectively. This confirm the influence of ion concentration on the stabilization of tetragonal phase, as was reported previously [26]. Interestingly, the tetragonal phase was increased to 85 wt% after the addition

of PLURONIC F-127 on codoped samples, see Figure 2.3a and 2.3b. However, in $ZrO_2:Er^{3+}$ the surfactant concentration does not induce any appreciable change on the phase composition. This difference suggests an increment on particles dispersion arresting growing crystallite size and then avoiding the conversion from tetragonal to monoclinic. For low concentration of dopant (0.2 mol%), the tetragonal crystalline structure is dominated by the annealing time since the content of this phase increases from 4.9 to 21.2% when the time is reduced from 5 h to 0 min, as is shown on the XRD pattern of Figure 2.3c and 2.3e.

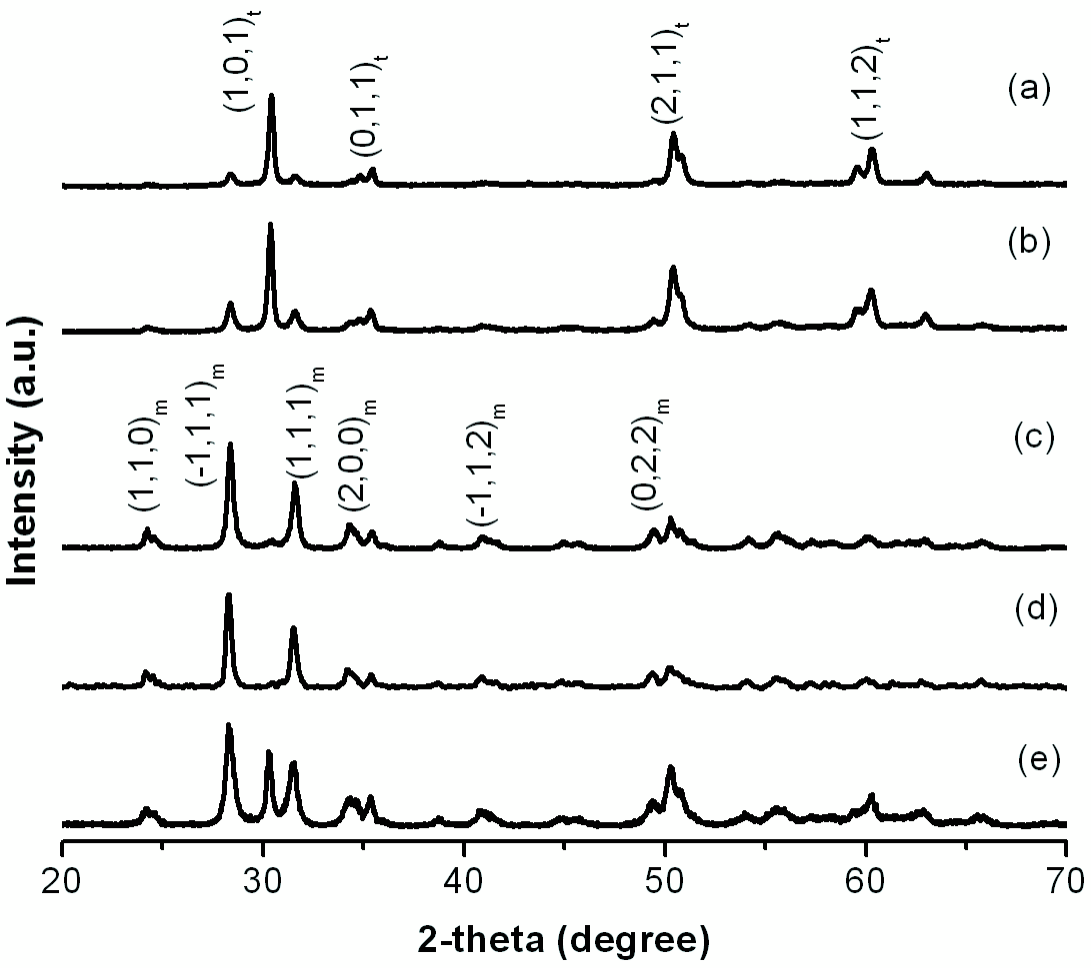

Figure 2.3: X-Ray diffractions patterns as function of surfactant concentration for samples (a) ZrO_2:Yb–Er, Mrp=0.0082-5h, (b) ZrO_2:Yb–Er, Mrp=0-5h (c) ZrO_2:Er, Mrp=0.0082-5h, (d) ZrO_2:Er Mrp=0-5h and (e) ZrO_2:Er Mrp=0.0082-0 min.

Table 2.2: Particle size as function of Pluronic F-127 concentration and annealing time.

Sample 0.2 mol% Er	Annealing time	Particle size (nm)
Mrp=0	5h	90
Mrp=0.0082	5h	82
Mrp=0.0082	0´	54
Mrp=0.01	5h	62

The crystallite size was calculated by the Sherrer's equation [11]

$$D = 0.9\lambda/(\beta \cdot Cos\theta) \quad (2.2)$$

Where λ stands for the X-ray wavelength, β for the corrected half-width of the strongest diffraction peak, and θ for the diffraction angle. The crystallite size for ZrO_2:Er^{3+} samples prepared with surfactant, Mrp=0.0082, was 54 nm and 37 nm for samples annealed 5 h and 0 min, respectively. The introduction of Pluronic keeps nanocrystals well dispersed even for a long annealing time as is shown in Fig. 2.4 for doped and codoped samples. The average particle size of ZrO_2:Yb^{3+}–Er^{3+} and ZrO_2:Er^{3+} nanophosphor synthesized with surfactant (Mrp=0.0082) and annealed at 1000^{o}C during 5 h is 75 nm and 82 nm, respectively. With a short annealing time (0 min at 1000^{o}C) the average particle size of ZrO_2:Er^{3+} nanocrystals decreased from 82 to 54 nm, suggesting a clear dependence on the annealing time. Considering that the average of crystallites per particle is 1.4, we can conclude that samples prepared with PLURONIC present high crystallite dispersion. The particle size for different annealing time and surfactant concentration is shown in Table 2.2.

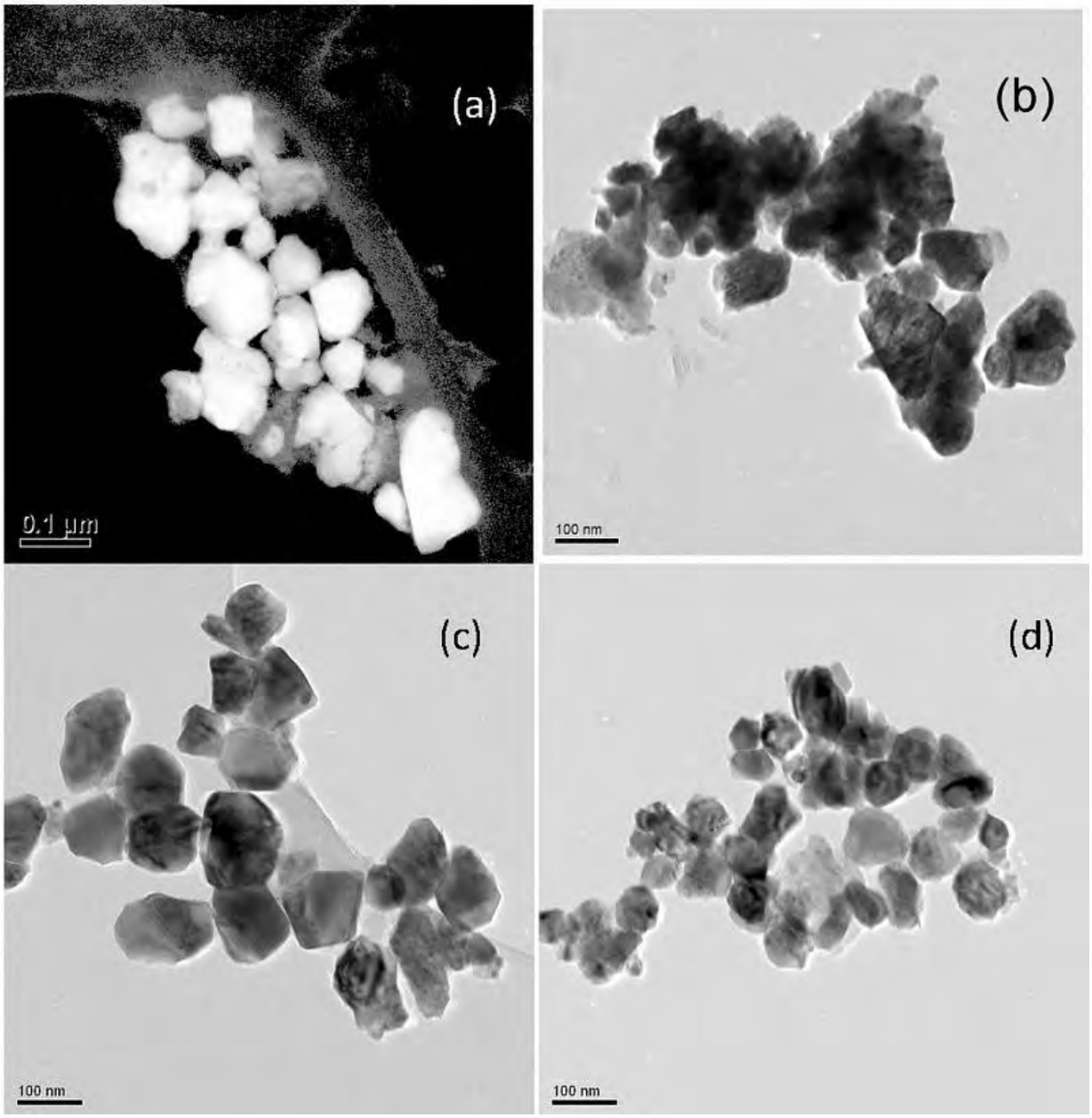

Figure 2.4: TEM micrographs of nanoparticles. (a) ZrO_2:Yb–Er, Mrp= 0.0082-5 h, (b) ZrO_2:Yb–Er, Mrp= 0-5 h and ZrO_2:Er, Mrp= 0.0082 annealed during (c) 5 h and (d) 0 min.

2.3.3. ORGANIC RESIDUALS IN ZrO_2: Yb^{3+}, Er^{3+}

The presence of organic residuals was analyzed by performing FTIR spectroscopy. Figure 2.5 shows the FTIR spectra for codoped samples prepared with and without surfactant annealed at 1000°C 5 h. The spectra presents several resonant stretching bands that are associated

with different residual components such as OH (3200 – 3800 and 1200 –1400 cm^{-1}), CH_2 (3000 cm^{-1}), CH-CH_2/CH_2 (1500 –1750 cm^{-1}), CH=CH (1050 cm^{-1}), H-C=O (800 cm^{-1}). The band centered at 2350 cm^{-1} is associated with CO_2 adsorbed to the surface, partly during the synthesis process and partly during measurements due to the granular characteristic of the nanopowder.

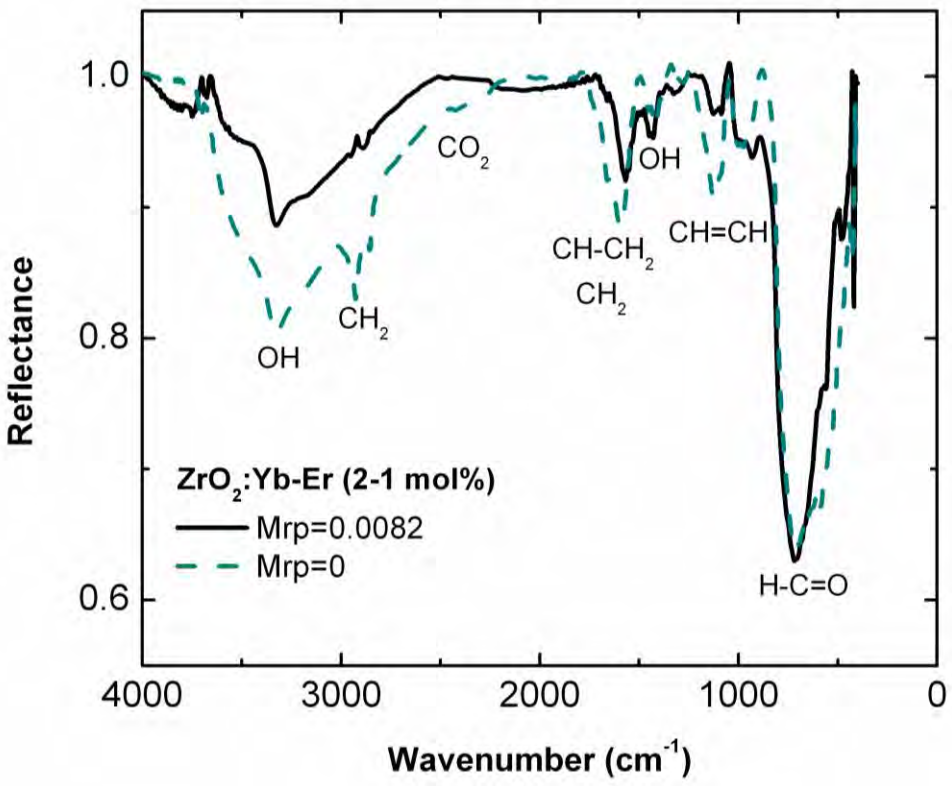

Figure 2.5: FT-IR spectra for surfactant and non-surfactant samples of ZrO_2:Yb-Er (2-1 mol%). Attenuation of OH- groups could be observed.

The OH^- was produced during the hydrolysis and condensation process and cannot be removed completely through a long time heat treatment. The presence of this component is inherent in the sol-gel process and is one of the main problems of the method. The other components are the result of different organic compounds used in the synthesis process. These include the organic part of zirconium n-propoxide, the high quantity of alcohol and surfactant. The introduction of surfactant reduces the residual OH^- component, as can be observed in the FTIR spectrum displayed in Figure 2.5 and was reported recently [12-14]. The

surfactant works as a dispersing agent and its function is to weaken the organic bond. Then, it reduces organic impurities, enhance the crystallization and, under optimum concentration, maintain the particle size.

2.4. LUMINESCENCE PROPERTIES

In order to increment the absorption of pumping energy, co-doping with Yb^{3+} ions is proposed since they present a broad and larger absorption cross-section and due to the possibility to transfer their absorbed energy to Er^{3+} ions. Materials doped with Er^{3+} ions and sensitized with Yb^{3+} ions have been widely studied because Er^{3+} ions have energy levels capable of infrared pumping that closely match the region of the 980 nm peak wavelength of Yb^{3+} absorption [15]. The large spectral overlap between Yb^{3+} emission ($^2F_{5/2} \rightarrow {}^2F_{7/2}$) and Er^{3+} absorption ($^4I_{15/2} \rightarrow {}^4I_{11/2}$) results in an efficient resonant-energy transfer from Yb^{3+} to Er^{3+} in $Yb^{3+} – Er^{3+}$ co-doped system [16], although, cooperative up-conversion rate depends strongly on the host materials [17]. More important, the excited estate of the Yb^{3+} ion has a much higher absorption cross section than the $^4I_{11/2}$ excited state of Er^{3+} thus rendering up-conversion much more efficient. Furthermore, Yb^{3+} ion possesses only one excited state with energy around 10,000 cm^{-1} (λ= 1.0 μm), associated to a convenient wavelength since many commercial diodes are readily available [3].

2.4.1. UP-CONVERSION EMISSION OF ZrO_2: Yb^{3+}, Er^{3+}

As a result of the up-conversion process, strong visible emission was observed in Yb^{3+}, Er^{3+} codoped ZrO_2 nanocrystals after 970 nm excitation. The emission spectra are shown in figures 2.6 and 2.7, as a function of ion concentration. The structure and position of all bands are in agreement with results reported in the literature. Emission is composed of two strong bands, the red one centered at 670 nm associated to $^4F_{9/2} \rightarrow {}^4I_{15/2}$ transition and the green band centered at 550 nm associated to the transition $^2H_{11/2} + {}^4S_{3/2} \rightarrow {}^4I_{15/2}$, and a weak band centered at 410 nm associated to $^2H_{9/2} \rightarrow {}^4I_{15/2}$ transition of the acceptor Er^{3+} ion (named that way since Yb^{3+} act as sensitizer). As is observed in both figures, the up-conversion emission is strongly influenced by the content of both Yb^{3+} and Er^{3+} ions. The overall intensity of the

emitted signal and the emission intensity of each band depend on the concentration of both ions. However, the effect of sensitizer (Yb^{3+}) content is dominant upon Er^{3+}. The increment of Er^{3+} ion with constant sensitizer concentration, enhance both green and red bands but quench the blue band, see Figure 2.6. After a critical concentration, 1 mol% of Er_2O_3, both bands are quenched but the green one is quenched stronger. Nevertheless, the increment of Yb^{3+} concentration enhances strongly both green and red bands but after a critical concentration, 2 mol% of Yb_2O_3, the green band was strongly quenched while the red band still enhanced, see Figure 2.7. The highest intensity red band was obtained for 4/1 mol% Yb_2O_3/Er_2O_3, and for higher concentration of Yb^{3+} the overall signal was quenched, but the green band almost disappears. Notice that also the blue band was quenched indicating that its presence depends strongly of the sensitizer concentration.

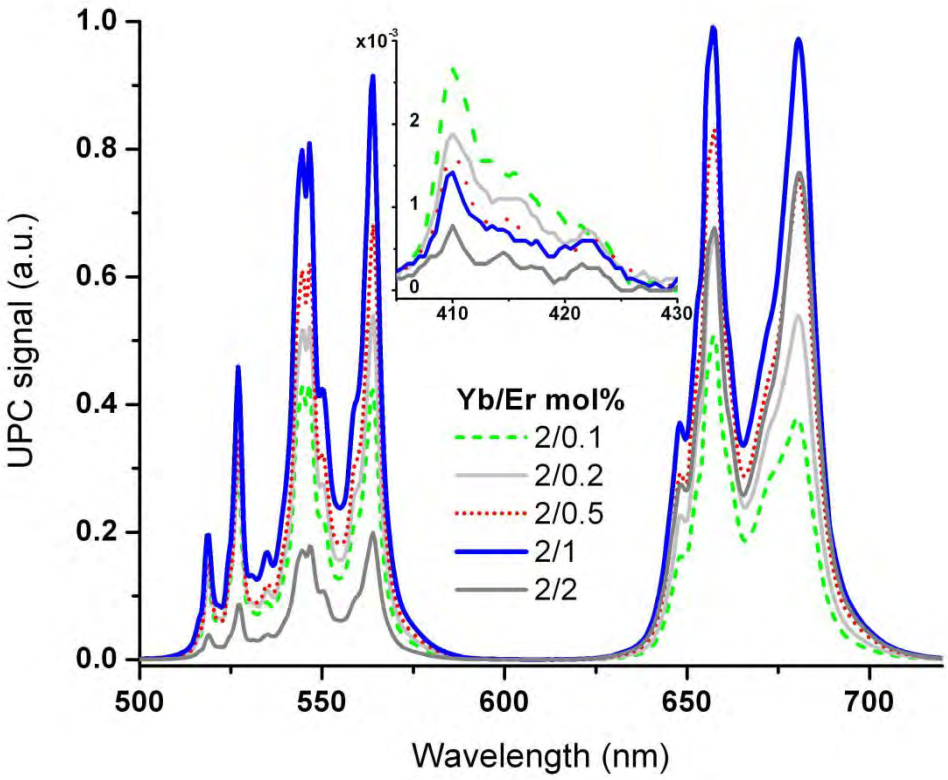

Figure 2.6: Up-conversion emission spectra for 2 mol% Yb^{3+} and different concentration of Er^{3+}. The inset shows the blue band.

A quantification of the overall intensity and the red/green emission ratio (R/G) as function of Yb^{3+} and Er^{3+} concentration is shown in Figure 2.8. The highest overall signal intensity corresponds to the composition 2/1 mol% (Yb/Er) with an R/G~1.5, perceptible to the naked eyes as a green-yellow emission with color coordinate (0.377, 0.612), see Figure 2.9. Interestingly, the spectrum of the emitted signal is determined by the Yb/Er concentration ratio and by the content of each ion. This can be observed from Figures 2.8 and 2.9 comparing the corresponding signal of 2/0.2 and 10/1 mol% (Yb/Er) composition. In both cases, Yb^{3+} is 10 times the Er^{3+} concentration but the overall intensity of the former is three times higher. The R/G ratio is completely different, 1.5 and 14, respectively. This means, the former looks green-yellow to the naked eyes while the last one looks red with color coordinates (0.373,0.615) and (0.573,0.417) respectively[1], as is shown in Figure 2.9.

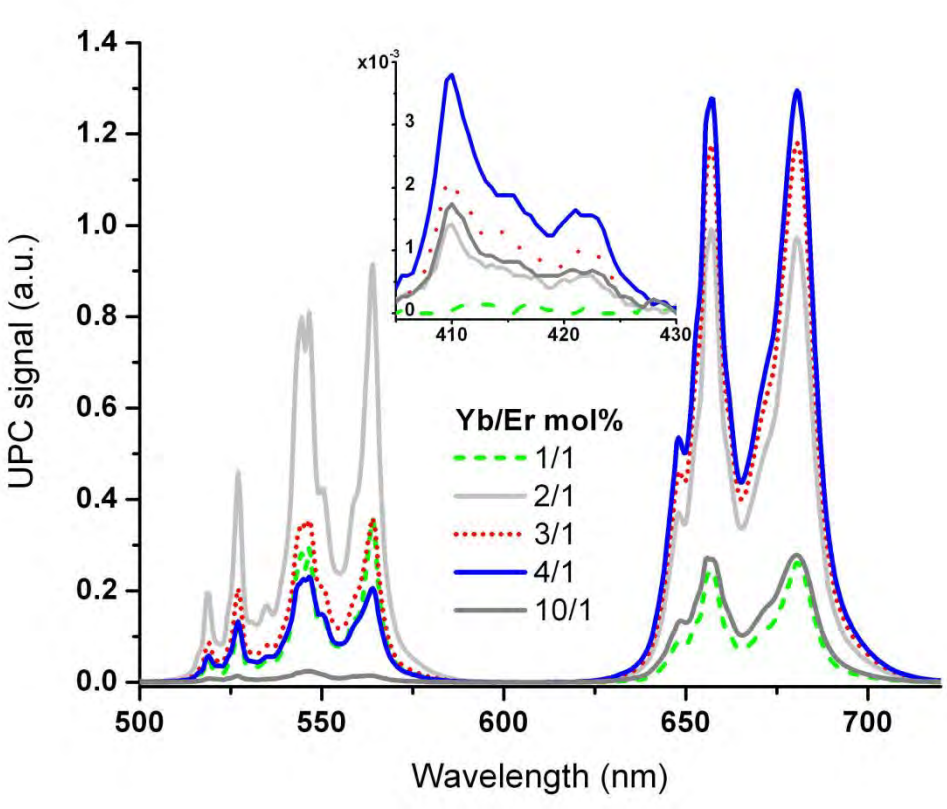

Figure 2.7: Up-conversion emission spectra for 1 mol% Er^{3+} and different concentration of Yb^{3+}. The inset shows the blue band.

[1] The procedure by which these coordinates are obtained is explained in Chapter 5, which describes aspects related to the chromaticity and color properties.

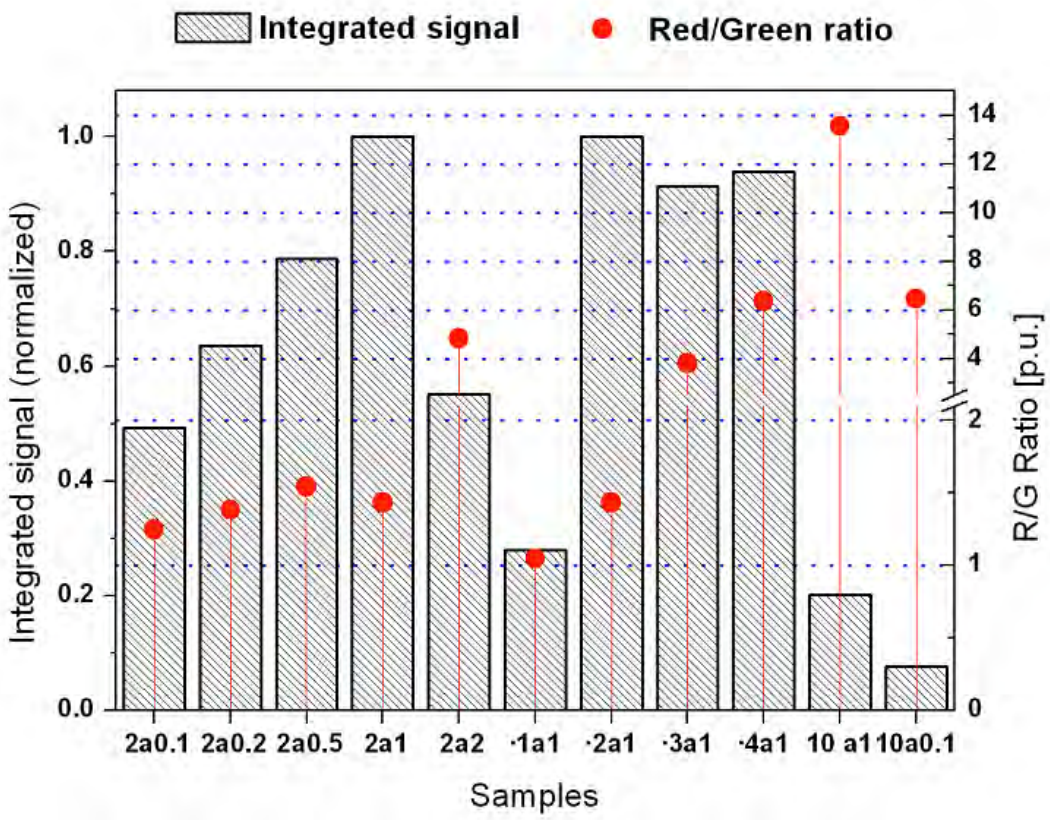

Figure 2.8: Integrated up-converted signal (rods) and red/green ratio as function of Yb^{3+}/Er^{3+} ion concentration.

Nevertheless, in this last case the up-conversion emission was 80% lower than the best luminescent sample under study. An interesting emission was obtained for the composition 3/1 mol% (Yb/Er). In this case, the overall intensity was 90% respect to the highest signal and presents an R/G~4 that looks yellow to the naked eyes with color coordinate (0.447,0.543); see Figure 2.9. In fact, orange to red color was tuned for R/G ≥ 4. Indeed, color coordinates between green-red and anywhere in between can be tuned by properly changing the Yb/Er composition as can be appreciated from Figures 2.8 and 2.9. This tuning capability promise potential applications of these nanocrystals, especially in biomedicine for labeling cells.

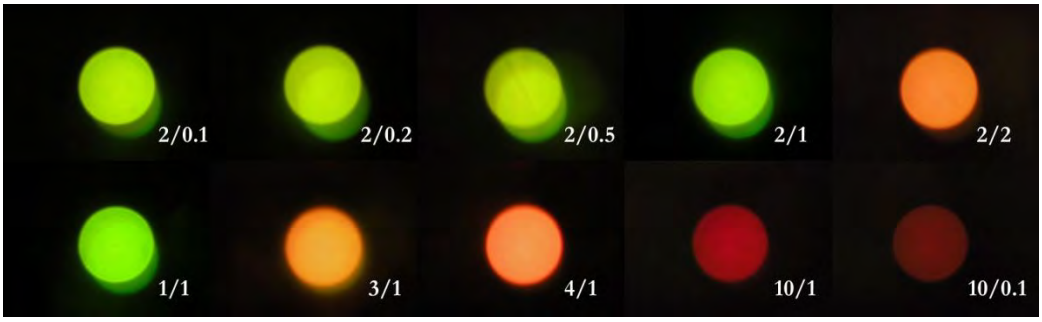

Figure 2.9: Photograph showing the luminescence of ZrO_2:Yb^{3+}-Er^{3+} nanocrystals after excitation at 970 nm for different ion concentration.

2.5. UP-CONVERSION EMISSION MECHANISM

The physical mechanism involved in the up-conversion (UC) processes can be elucidated by analyzing the dependence of the integrated up-converted signal intensity (I_{uc}) as function of the pumping intensity (I_{pump}). As is well-known, for unsaturated UC process the number of required photons (n) to populate the emitting states is related with the pumping intensity and up-converted signal by the expression $I_{uc}=kI_{pump}^{2}$, such dependence is shown in Figure 2.10. It is observed that for green emission and different concentration of both Yb and Er ions n~2 confirming the expected two photon process. For red emission, the n value deviate from the expected 2 to 1.6 for different concentration of Er, but for larger concentration of sensitizer diminishes to 1. Such changes suggest the presence of additional processes strongly related with the presence of Yb^{3+}. An interesting result was observed for the blue band; it was obtained the expected n~3 for the three-photon process for lowest concentration of Er^{3+} (0.1 mol% of Er_2O_3); though, for higher concentration of both Er^{3+} and Yb^{3+} it changes to n~2. Thus, the typical two-photon process for green and red band and three-photon for blue emission described above are strongly affected by the presence of larger concentration of both codopants. It can be attributed to the linearization of up-conversion process because of the saturation of $^4I_{13/2}$ energy level due to the combined effect of cross relaxation and energy back transfer process, as will be discussed below.

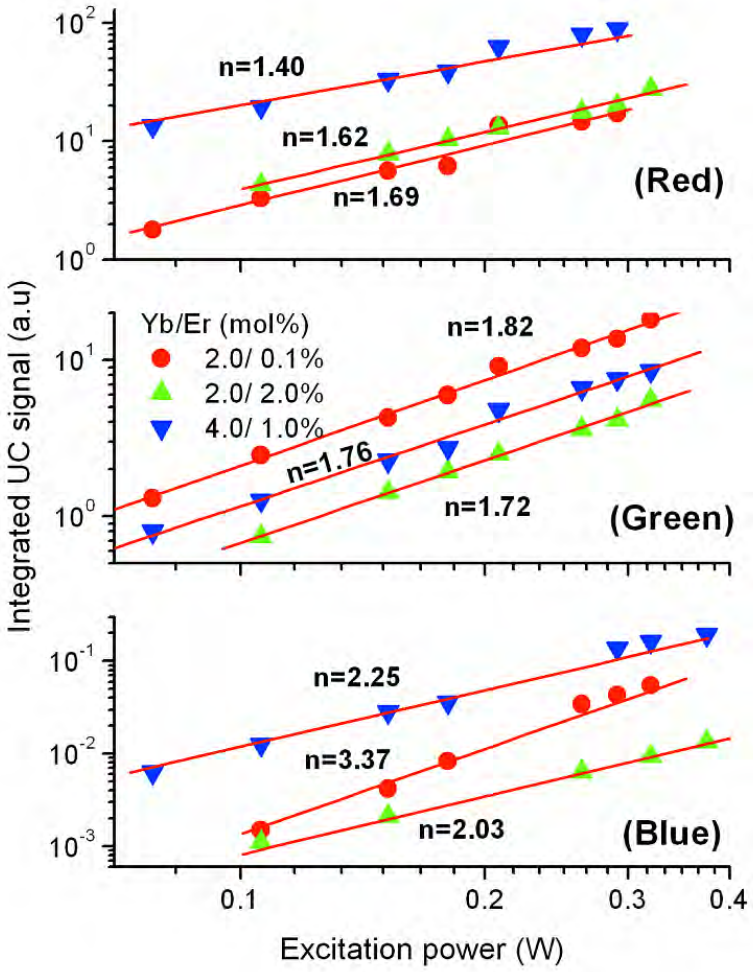

Figure 2.10: Integrated up-converted signal as function of pumping power and different codopant concentration for (a) red, (b) green, and (c) blue band.

The up-conversion is a phenomenon resulted from the interaction between neighboring ions; such interaction depends on the host and dopant concentration. The absorption cross-section of Yb^{3+} is much higher than that of Er^{3+}, and then the mechanism is in all probability dominated by the energy transfer (ET) from Yb^{3+} (donor) to Er^{3+} (acceptor). Nonetheless, ET from Er^{3+} to Er^{3+} is feasible, especially for high concentration. Thus, the mechanism proposed to explain the observed visible emission in accordance with the number of photons described above is based on the energy transfer between Yb-Er, and probably some Er-Er, as is described in the energy levels diagram shown in Figure 2.11. As is shown in such figure, the $^4I_{11/2}$ intermediate excited state of Er^{3+} ion is populated by pumping photons (970 nm) via ET1

from Yb^{3+} and described by the equation $(^4F_{5/2} + {}^4I_{15/2}) \rightarrow (^4F_{7/2} + {}^4I_{11/2})$. Part of this population is promoted to $^4F_{7/2}$ level by absorbing a second pumping photon (ESA) or by the energy transfer (ET2) from a neighbor ion, either Yb^{3+} or Er^{3+}. Population in this excited state is phonon coupled (≈3 phonons from host) to the level $^2H_{11/2} + {}^4S_{3/2}$. From here, part of the population decay radiatively to ground state producing the green emission $(^2H_{11/2} + {}^4S_{3/2} \rightarrow {}^4I_{15/2})$. Producing the red band $(^4F_{9/2} \rightarrow {}^4I_{15/2})$ is feasible if part of the population in $^4S_{3/2}$ could be non-radiative relaxed to $^4F_{9/2}$, otherwise population in $^4I_{11/2}$ could be non-radiative relaxed to $^4I_{13/2}$ intermediate level, and then promoted to $^4F_{9/2}$ level by the energy transfer (ET3) from a neighbor ion, either Yb^{3+} or Er^{3+}. This mechanism is in agreement with the most standard explanation of the UC process, especially for low ion concentration, and is consistent with the two photons required to produce green and red bands.

However on the host under study, $^4F_{11/2} \rightarrow {}^4I_{13/2}$ non-radiative transition (~3650 cm^{-1}) would require more than seven phonons from host (~470 cm^{-1}), it must therefore follow that this transition becomes unlikely. Similar situation occurs for $^4F_{9/2}$ feeding because red emission from the $^4F_{9/2}$ state can hardly arise, since the $^4F_{9/2}$ state has a large energy gap of about (~3100 cm^{-1}) below the $^4S_{3/2}$ state, more than six times the phonon energy of the ZrO_2 lattice (470 cm^{-1}). Since the $^4F_{9/2}$ state is almost not populated by the above $^4S_{3/2}$ state, as well as $^4I_{13/2}$ by the above $^4I_{11/2}$ level, it is thus that such coupling is possibly promoted by the phonon energy introduced by the presence of some impurities such as OH- (3450 cm^{-1}) and CO_2 (1850 cm^{-1}), which resonant stretching bands in infrared spectrum are essentially significant, as is elsewhere reported [18,19]. The CO_2 is adsorbed to the surface partly during the synthesis and partly from the environment. The OH- was produced during the hydrolysis and condensation process and it is inherent to the synthesis process.

Experimental results show strong dependence on the ion concentration suggesting the presence of additional mechanism to produce UC emission, see Figures 2.6 and 2.7.

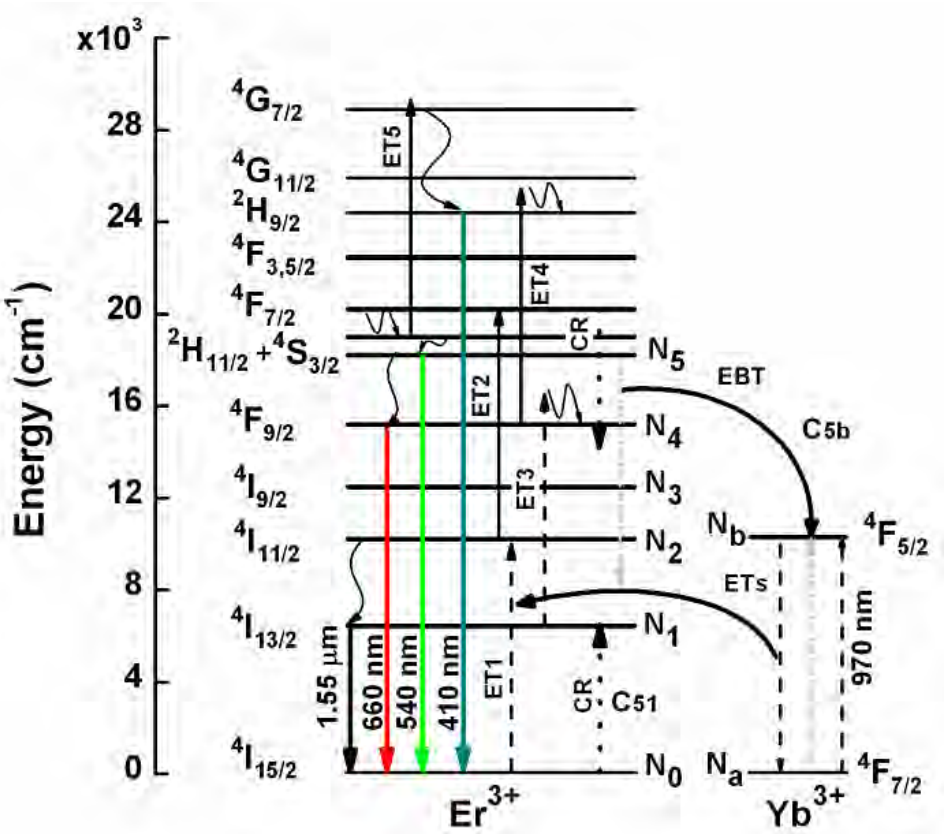

Figure 2.11: Energy diagram for the proposed mechanism of up-conversion process.

The cross-relaxation (CR) is the only process that is strongly Er^{3+} concentration dependent. The CR process ($^4S_{3/2}$ + $^4I_{15/2}$) → ($^4I_{9/2}$ + $^4I_{13/2}$), see Figure 2.8, induces a decrement of population on $^4S_{3/2}$ and an increment on $^4I_{13/2}$ level. In this case, the population on $^4I_{13/2}$ is promoted to $^4F_{9/2}$ by the assisted energy transfer (ET3) from an excited Yb^{3+} or Er^{3+} ion. Phonon coupling of $^4S_{3/2}$ and $^4F_{9/2}$ by OH is suggested by the almost constant red/green ratio for low Er^{3+} concentration (as low as 0.1 mol%) and the strong red/green ratio variation implies the dominance of CR for concentration higher than 1 mol%; see Figure 2.6. These processes explain the quenching of the green band and the enhancement of the red emission. The quenching of the overall up-converted signal intensity is the result of Er^{3+} ion agglomeration from 2 mol% thereafter. Similar quenching behavior is exhibited on other hosts such as $Cs_3Lu_2Cl_9$, Ba_2YCl_7, $LiYF_4$ and Y_2O_3 [20,21].

The presence of sensitizer increases the overall up-converted signal and modifies the red/green ratio; see Figures 2.8 and 2.9. Both figures show the enhancement of the red band and the quenching of the green emission as function of Yb concentration. Such behavior suggest, in addition to CR, the presence of energy back transfer (EBT) from acceptor (Er^{3+}) to donor (Yb^{3+}) described by the equation $(^4S_{3/2} + {}^4F_{7/2}) \rightarrow (^4I_{13/2} + {}^4F_{5/2})$ as has been suggested recently [28]. This process has two effects, increase the population on $^4I_{13/2}$ of Er^{3+} and the population on $^4F_{5/2}$ of Yb^{3+}. The former is partly promoted to $^4F_{9/2}$ by the energy transfer ET3 produced by the non-radiative relaxation of Yb^{3+} ($^4F_{5/2}$), see Figure 2.11. The EBT and CR processes promote saturation on $^4I_{13/2}$ (both create a good population reservoir) that is increased as Yb and Er concentration increases, respectively. As is well-known, this type of saturation induces linearization of the process for very high concentration as is confirmed for Yb^{3+} where n~1. Notice that EBT, and then quenching of the green band, start for concentration larger than 1 mol% of Yb_2O_3, but for 10 mol% quenching of the overall emitted signal was observed as a result of energy migration produced by the agglomeration of Yb^{3+} ion.

The blue band associated to $^2H_{9/2} \rightarrow {}^4I_{15/2}$ transition is strongly dependent of donor and acceptor concentration, see Figures 2.6 and 2.7. The quenching of the signal with the increment of Er^{3+} suggests that $^2H_{9/2}$ was partly filled from $^2H_{11/2} + {}^4S_{3/2}$, via ET5, coming from an Yb^{3+} or Er^{3+} relaxation. The increment of signal with Yb^{3+} concentration could imply that ET, CR and EBT play an important role in the blue band emission. This is hinted by the increment of blue band intensity with the increment of sensitizer concentration (Yb^{3+}).

As was discussed previously, it is considered two mechanisms, shown in Figure 2.11, which could possibly induce saturation of the $^4I_{13/2}$ energy level of Er^{3+}, the EBT process and the CR process. The EBT process is inherently efficient and becomes more prominent for higher Yb^{3+} ion concentration due to reduced average distance between the Yb^{3+} and the Er^{3+} ions. It is dominating at high Yb^{3+} ion concentration mainly due to CR process cannot saturate the $^4I_{13/2}$

(Er) state, since an efficient CR process requires a large number of Er^{3+} ions in the $^2H_{11/2}$ and the ground state simultaneously, which contradicts saturation of the $^4I_{13/2}$ state.

2.5.1. MODELLING THE UP-CONVERSION PROCESS

The contribution of CR and EBT on the green and red emission was studied by analyzing the behavior of the Red/Green ratio. It was modeled according to transitions described above (see Figure 2.11) and by using the following steady-state rate equations. For this study, the weak blue emission band was not considered.

$$\frac{dN_b}{dt} = \alpha_{ab}\phi_p - C_{b5}N_2N_b - C_{b4}N_1N_b - C_{b2}N_0N_b + C_{5b}N_aN_5 - W_bN_b \quad (2.3)$$

$$\frac{dN_1}{dt} = -C_{b4}N_1N_b + C_{51}N_5N_0 + C_{5b}N_aN_5 + W_{21}N_2 - W_1N_1 \quad (2.4)$$

$$\frac{dN_2}{dt} = C_{b2}N_0N_b - C_{b5}N_2N_b - W_2N_2 + W_{32}N_3 - W_{21}N_2 \quad (2.5)$$

$$\frac{dN_3}{dt} = -W_{32}N_3 + W_{43}N_4 + C_{51}N_5N_0 - W_3N_3 \quad (2.6)$$

$$\frac{dN_4}{dt} = C_{b4}N_1N_b - W_{43}N_4 - W_4N_4 + W_{54}N_5 \quad (2.7)$$

$$\frac{dN_5}{dt} = C_{b5}N_2N_b - W_5N_5 - W_{54}N_5 - C_{51}N_5N_0 - C_{5b}N_aN_5 \quad (2.8)$$

Where $\frac{dN_i}{dt} = 0$ on steady-state for *i=b,1,...,5* and N_b (W_b), N_1 , N_2 (W_2), N_3, N_4 (W_4) and N_5 (W_5), are the population densities (radiation rates) of $^2F_{5/2}$ (Yb^{3+}), $^4I_{13/2}$, $^4I_{11/2}$, $^4I_{9/2}$, $^4F_{9/2}$ and $^2H_{11/2}$ + $^4S_{3/2}$ states, respectively. N_a and N_0 are the population densities of the Yb^{3+} and Er^{3+} ions in the ground state. C_{b2}, C_{b4} and C_{b5} denote the direct energy transfer transitions (ET1), (ET3) and (ET2), respectively. C_{5b} and C_{51} are the coefficient of back transfer and cross relaxation process, respectively. ϕ_p is the laser pump intensity and α_{ab} denotes the absorption cross section of the Yb^{3+} ion. W_{ij} are the non radiative transition between $i \rightarrow j$ energy level.

In those equations, the radiation decay of $^4I_{13/2}$ energy level (W_1N_1) in equation 2.4 was neglected due to its longest lifetime of several milliseconds, which creates a good population reservoir for excited Er^{3+} ions. It is also reasonable to neglect the non radiative decay $W_{21} \rightarrow 0$, considering that such coupling (~3650 cm^{-1}) will require ~8 phonons due to the low phonon energy of the host. Coupling could be promoted by the presence of OH (3450 cm^{-1}) and CO_2 (1850 cm^{-1}) impurities; however this possible effect was not included into the model by considering low its contribution. In addition, emission is not observed for $^4I_{9/2}$ level, suggesting that W_3 can be neglected, from equation 2.6. Additionally, it is reasonable to neglect the contribution to the population of the $^2F_{5/2}$ (Yb) state ($C_{5b}N_aN_5$) resulting from the EBT process in equation 2.3, when compared to that induced by the laser excitation. After these considerations, a theoretical steady state approach to the N_4/N_5 ratio associated to the population on transitions producing red and green emission was obtained. The population density N_4 was obtained from equation 2.7 in terms of N_1 and N_5

$$N_4 = \frac{1}{W_{43} + W_4}(C_{b4}N_1N_b + W_{54}N_5) \tag{2.9}$$

N1 was obtained from equation 2.4

$$N_1 = \frac{N_5}{C_{b4}N_b}(C_{51}N_0 + C_{5b}N_a) \tag{2.10}$$

Combining equations 2.9 and 2.10 it can be obtained the ratio N_4/N_5

$$\frac{N_4}{N_5} = \frac{W_{54}}{W_{43} + W_4} + \frac{1}{W_{43} + W_4}(C_{51}N_0 + C_{5b}N_a) \tag{2.11}$$

This equation fit well the experimental data with a standard deviation of 0.09, as is shown in Figure 2.12. The theoretical fitting suggest that $W_{54}/(W_{43} + W_4) \sim 0$. This term is the contribution of phonon coupling between $^2H_{11/2}$ + $^4S_{3/2}$ and $^4F_{9/2}$ (W_{54}). As was discussed above, the associated energy for this coupling is 3,280 cm^{-1} and demands ~7 phonons considering the phonon energy of the host, which make difficult to occur. The phonon energy introduced by the presence of impurities such as OH and CO_2 compounds can promote it.

However, the theoretical fitting confirms the absence or at least the very low effect of such impurities in the emitted signal from all prepared samples. Thus, for a host with low phonon energy, and in the absence or low concentration of impurities, the first term can be neglected. In such a case, for population of Er^{3+} much larger than Yb^{3+} ($N_0 >> N_a$) eq. 2.9 is dominated by the second term corresponding to the cross-relaxation process, $N_4/N_5 \approx C_{51}N_0/(W_{43}+W_4)$. If $N_a >> N_0$, then eq. 2.11 is dominated by the third term corresponding to the energy back transfer process, $N_4/N_5 \approx C_{5b}N_a/(W_{43}+W_4)$.

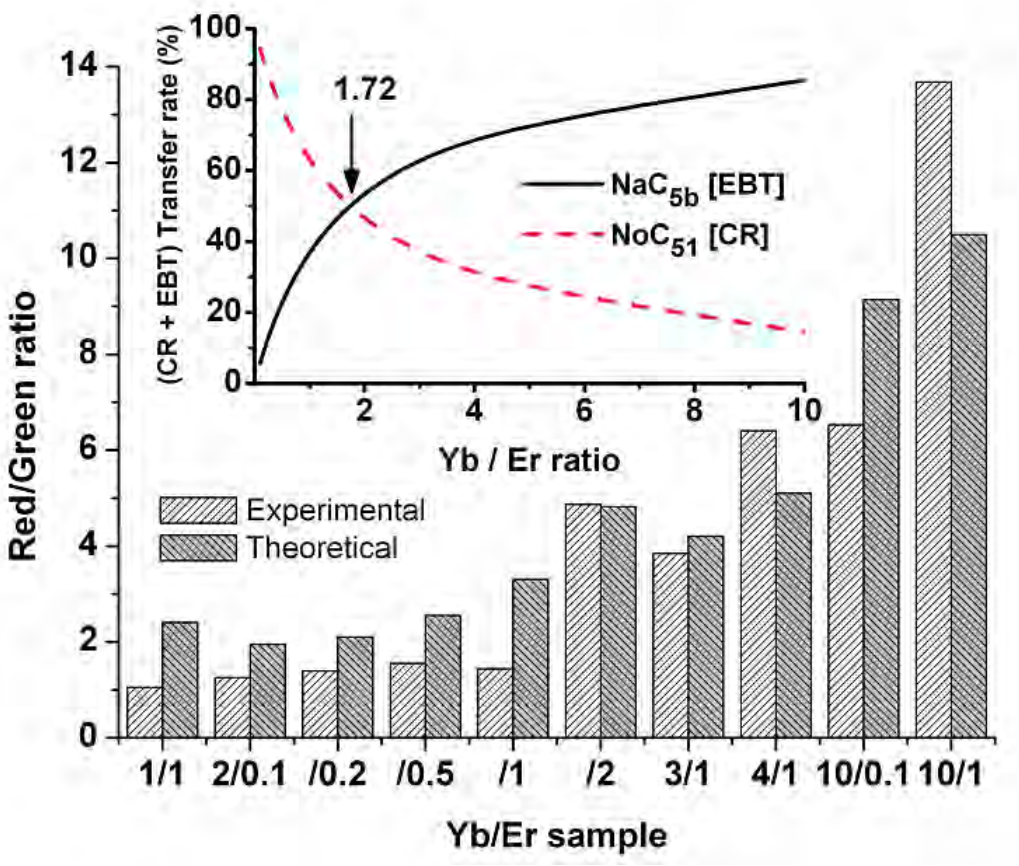

Figure 2.12: Experimental and theoretical fitting of red/green ratio as a function of codopant ions. The inset shows the behavior of cross-relaxation and energy back transfer terms as function of Yb^{3+}/Er^{3+} concentration ratio.

The CR and EBT contribution term are complements, the enhancement of one means the deleterious effect in the other one. The inset of Figure 2.12 shows the contribution of each term calculated by fitting the experimental data, as a function of Yb/Er ion concentration ratio. Equal contribution occurs for a concentration ratio of Yb/Er ≈1.72 and describes the limit approximation of N_4/N_5 as was described above. Of course, the red/green ratio is quenched for very large concentration. Once each term was calculated for each composition, and considering $W_{43} \approx 0$ that is reasonable to neglect taking into account that phonon coupling energy is 2,440 cm^{-1} demanding ~5 phonons, the cross relaxation and energy back transfer coefficient were calculated for different ion concentration and listed in Table 2.3.

For the set of samples with different concentration of Er^{3+} both coefficients are constant, with values of C_{51}~5.81x10^{-18} cm^3s^{-1} and C_{5b}~3.43x10^{-18} cm^3s^{-1}. These values were obtained for the tetragonal phase, the dominant crystalline structure for dopant concentration lower than 3 mol%. However, both coefficients increase with the increment of sensitizer where cubic phase is dominant but C_{51} increase faster than C_{5b}, see Table 2.3. Apparently cubic crystalline phase promote more the CR effect than EBT. The largest value of coefficients, C_{51}~1.02x10^{-16} cm^3s^{-1} and C_{5b}~6.04x10^{-17} cm^3s^{-1}, were calculated for the largest concentration of dopants where pure cubic crystalline structure were obtained. In addition, the increment of C_{5b} coefficient was expected because it depends on Yb^{3+} concentration.

Table 2.3: Cross relaxation (C_{51}) and energy back transfer (C_{5b}) coefficient for different dopant composition.

Yb^{3+} (mol%)	**Er^{3+} (mol%)**	**C_{5b} [x10^{-18}]** cm^3s^{-1}	**C51 [x10^{-18}]** cm^3s^{-1}
2	**1**	3.43	5.81
3	**1**	7.8	13.29
4	**1**	8.79	14.90
10	**0.1**	16.42	27.81
10	**1**	60.47	102.42

In general, equation 2.11 is in correspondence with the model proposed recently by G. Chen and co-workers in the appropriate approximation [28]. Here, we have extended the model, as it has included the effect of CR, together with the EBT process, as well as the calculation of their coefficient values. In addition, we have simulated the ratios between red and green bands (R/G) for each studied concentration, in order to compare it with experimental values. Our experimental results indicate that the red and green emission in ZrO_2:Yb^{3+}-Er^{3+} nanocrystals are the result of both cross-relaxation and energy back transfer process strongly influenced by ion concentration. In fact, the cross relaxation coefficient is larger than the back transfer coefficient. However, according to the experimental and theoretical results, the CR process is dominant for a concentration ratio Yb/Er ≤ 1.72 in any other case the dominant is the EBT process. The contribution of EBT was ~55% for the largest emitted signal Yb/Er = 2/1, ~70% for 5/1 and ~80% for 10/1 concentration ratio.

2.5.2. LUMINESCENCE DECAY TIME

Analysis of luminescence decay time shows the influence of ions concentration in the dynamics of up-conversion process. Figure 2.13 shows the typical decay time plot for green (540 nm) and red (670 nm) emission. Notice that in both cases experimental data are fitted with a double exponential function. In nanocrystals, a significant portion of the rare earth ions are located on the particle surface due to their small size and therefore such ions have more interaction with impurities adsorbed on the surface (OH and CO_2) promoting non-radiative relaxation and then leading to a non-exponential decay curve. In general, the fast decay time is probably associated with the presence of those non radiative processes described above, phonon energy, impurities, cross relaxation, energy back transfer, migration or promotion to higher level. The effective decay time was calculated by the expression [22]

$$\tau_{eff} = \int_0^\infty tI(t)dt \Big/ \int_0^\infty I(t)dt \qquad (2.12)$$

and the respective values are listed in Table 2.4. The effective decay time diminishes 44% and 13% for green and red band, respectively, as the concentration of Er ion increases, see Figure

2.14. Such behavior is consistent with the stronger quenching of the green band compared to the red emission as was discussed before. The continuous diminish of decay time suggest the presence of luminescent quenching produced by the cluster formation of Er ion due to the increment of concentration that is also responsible of the up-converted signal increment.

Table 2.4: Effective decay time and energy transfer efficiency for different composition of dopants.

Transition	$^4F_{5/2}$–$^4F_{7/2}$	($^4F_{5/2}$–$^4I_{15/2}$)→ ($^4F_{7/2}$–$^4I_{11/2}$)	$^4F_{9/2}$–$^4I_{15/2}$	$^2S_{3/2}$+$^2H_{11/2}$–$^4I_{15/2}$
Samples [mol%]	τ_{eff} [μs]	η_{ET}	τ_{eff} [μs]	τ_{eff} [μs]
2/0.1	727	0.043	476	380
2/0.2	641	0.156	455	339
2/0.5	665	0.125	431	283
2/1	539	0.290	438	290
2/2	273	0.640	415	207
1/1	687	0.228	389	281
2/1	539	0.290	438	290
3/1	NA	NA	290	190
4/1	358	0.137	205	134
10/1	NA	NA	100	160
10/0.1	NA	NA	20	85

Dependence of τ_{eff} with Yb^{3+} concentration is quite similar than that observed for Er^{3+}. In this case, decay time diminishes 62% and 53% for green and red emission, respectively, and both follow the same behavior, see Figure 2.14. Interestingly, the increments of decay time (~20%) for both green and red bands with sensitizer changing from 1 to 2 mol% of Yb_2O_3 suggest the reduction of radiative energy transfer between Yb^{3+} neighbor ions [23]. Such value is the optimum concentration for the highest up-converted emitted signal, see Figure 2.7. Effective decay time diminish 94% for very large concentration of Yb^{3+} (10 mol%). The strong reduction is in correspondence with the strong quenching of up-converted signal and is probably the result of energy migration due to the cluster formation of sensitizer as has been reported by others authors [19,24,25]. The energy transfer efficiency is also strongly dependent of

concentration of both ions. Effective decay time of Yb^{3+} (donor) at 1040 nm was measured with and without the presence of acceptor (Er^{3+}), and by using the following expression [26]

$$\eta = 1 - \tau_{Yb(RE)} / \tau_{Yb} \qquad (2.13)$$

The energy transfer efficiency was calculated and listed in Table 2.4. Effective decay time at 1040 nm for 1, 2 and 4 mol% of Yb^{3+}, no Er^{3+}, resulted in 890, 760 and 415 µs, respectively. As is expected, η is very low for low concentration of acceptors but increases to ~64% for 2 mol% of Er_2O_3. Notice that efficiency is only ~29% for the optimum composition 2/1 (Yb/Er) by which the highest up-converted signal was obtained. The luminescent quenching of up-converted signal for large η associated to high concentration of acceptors is the result of Er^{3+} clustering. The reduction of η with the increment of donor concentration is probably associated with the presence of back energy transfer process and Yb^{3+} clustering.

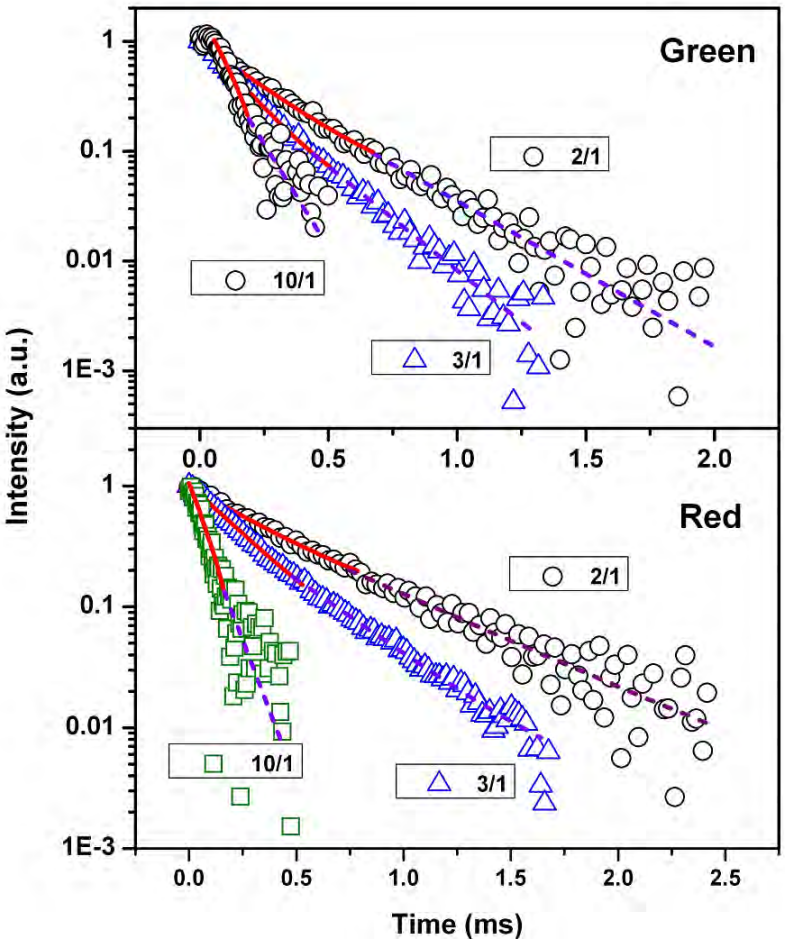

Figure 2.13: Typical decay time plot for green (a) and red (b) emission bands.

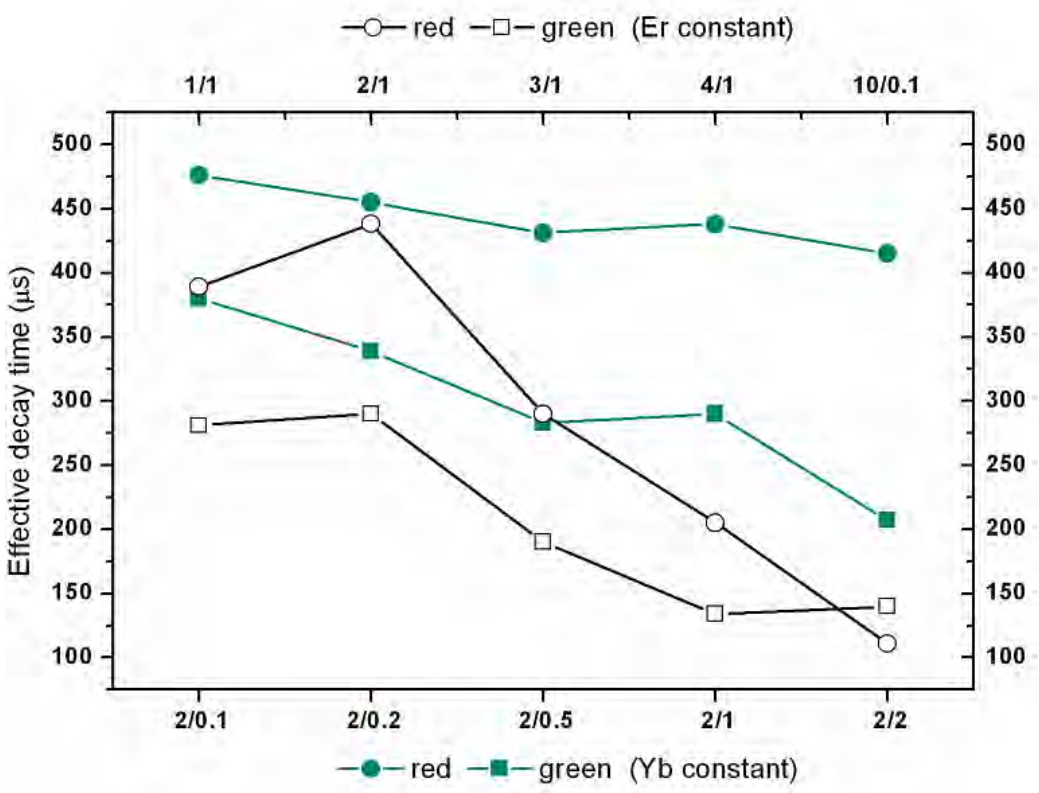

Figure 2.14: Effective decay time as a function of ion concentration for both sets of samples.

2.6. SURFACTANT EFFECT ON LUMINESCENCE PROPERTIES

Experimental results show that luminescence emission is strongly dependent on the annealing time and on the surfactant concentration (Pluronic F-127), as is shown in Figure 2.15 for ZrO_2:Er^{3+} nanocrystals. The figure describes the behavior of the integrated green signal for different combinations of annealing time and surfactant content. The up-converted signal was increased with the content of PLURONIC and diminished for concentration higher than Mrp= 0.0082. With that concentration the integrated signal obtained by annealing 5 h at 1000^{o}C is notably higher (97%) than the signal obtained without surfactant for the samples annealed 5 h and 70% for samples annealed 0 minutes with Mrp= 0.0082.

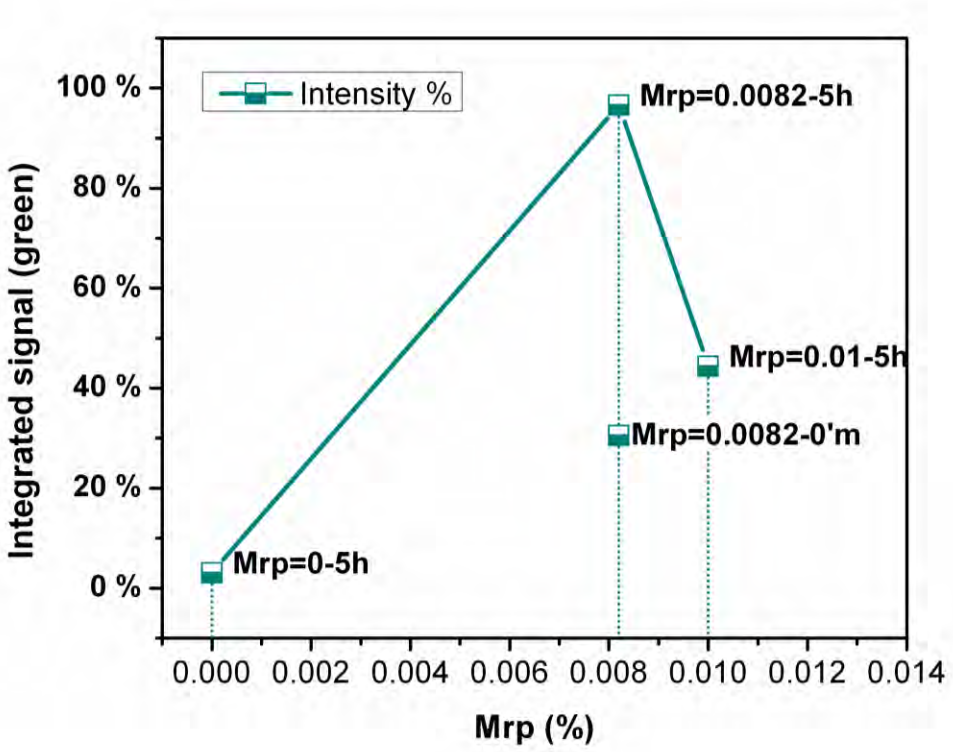

Figure 2.15: Green emission intensity of $ZrO_2:Er^{3+}$ samples as a function of surfactant concentration and annealing time.

Such a strong increment in the emitted signal is related with the reduction of organic impurities as a result of the annealing time increment (0 min to 5 h) and the use of Pluronic F-127 during synthesis process, as has been reported recently [14,27]. The annealing time controls the crystallite size and the surfactant disperses nanocrystals reducing agglomeration and absorption of impurities on the crystallite surface.

The introduction of sensitizer (Yb^{3+}) enhances strongly the up-converted emission of Er^{3+} as is shown in Figure 2.16. Furthermore, the introduction of PLURONIC F-127 produce higher emitted signal. The little difference in the spectral profile structure for doped and co-doped samples is produced by different phonon energy and crystalline field surrounding Er ion, as a result of different crystalline phase. The introduction of sensitizer changes the ratio of green/red emission bands. The red enhancement depends on the concentration of both ions, Er due to cross-relaxation process and Yb due to ET [28,29].

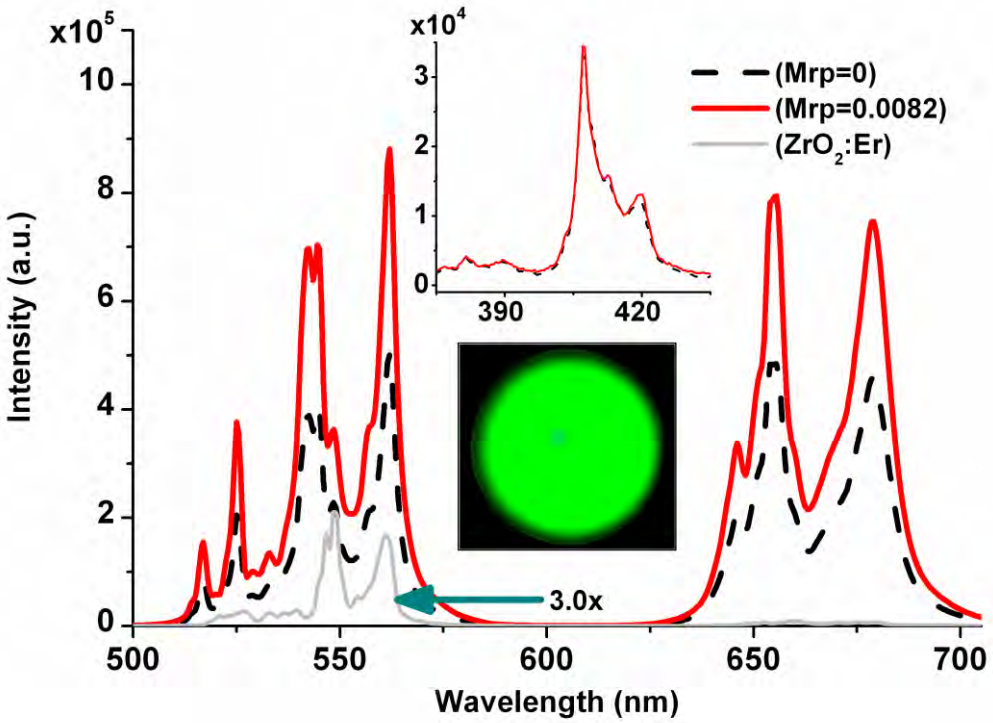

Figure 2.16: Up-conversion emission spectra of $ZrO_2:Yb^{3+}$-Er^{3+} and $ZrO_2:Er^{3+}$. The inset shows the blue emission spectra and a picture of the green emission of codoped sample. $ZrO_2:Er^{3+}$ luminescence is amplified by 3x.

The overall signal intensity in the visible range increases 65% with the optimum concentration of surfactant. Such enhancement is the result of the reduction of impurities as was discussed before. Interestingly, the enhancement is different for each emission band. The intensity increased 75% and 60% for green and red band, respectively. However, a slight increment of 6% was observed for blue emission. As was discussed before, the OH^- ions on the surface would result in an enhancement of the red band and a reduction of the green emission by phonon coupling of $^4F_{7/2} \rightarrow {}^4F_{9/2}$ and $^4I_{11/2} \rightarrow {}^4I_{13/2}$ transitions, this coupling has been also reported by others authors [30]. Thus, the larger enhancement of green band suggests a reduction of OH groups as was confirmed from FTIR spectra; see Figure 2.5.

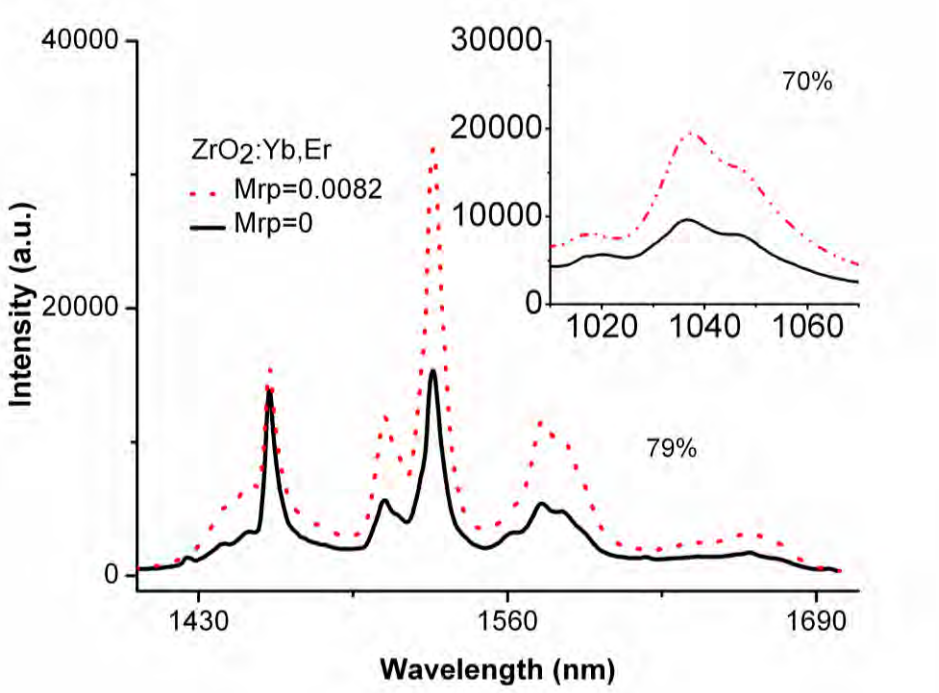

Figure 2.17: NIR emission spectra of ZrO_2:Yb^{3+}-Er^{3+} codoped samples. Eye-safe emission centered at 1550 nm of Er^{3+} ion and the inset shows the characteristic emission of Yb^{3+} centered at 1036 nm.

Figure 2.17 shows the eye-safe emission centered at 1.52 μm associated to $^4I_{13/2} \rightarrow {}^4I_{15/2}$ transition of Er^{3+} ion. The inset corresponds to the characteristic emission of Yb^{3+} centered at 1036 nm ($^2F_{5/2} \rightarrow {}^2F_{7/2}$). As is expected, both near infrared emission bands present a strong enhancement with the presence of surfactant being 79% for eye-safe emission band and 70% for Yb characteristic emission. As was discussed before, the presence of OH^- produces a deleterious effect on the luminescence properties, especially in the near infrared range. Thus, the strong enhancement of both bands indicates the OH^- reduction as can be observed in Figure 2.5. In turn, the OH^- reduction by the surfactant propitiates a more energy transfer from the Yb^{3+} to Er^{3+} by the decrement of non-radiative process.

2.6.1. LUMINESCENCE DECAY TIME

The luminescence decay times of Er^{3+} doped and Yb^{3+}-Er^{3+} codoped ZrO_2 nanocrystals were obtained as function of annealing time and surfactant concentration. Figure 2.18 shows decay time of emission at 550 nm of ZrO_2:Er^{3+} for samples prepared with and without surfactant and

calculated values are listed in Table 2.5. Notice the fast decay time, τ=26 μs, of sample prepared without surfactant being fitted to single exponential function. Such fast decay is produced by the presence of high concentration of impurities such as OH^- and CO_2 that can be corroborated from FTIR, and probably surface defects produced by the crystallite size. It is not connected with energy migration due to ion clustering considering the low concentration of Er^{3+} (0.2 mol%). The introduction of surfactant enlarges decay time but two exponential functions are required to fit the experimental data. In this case and taking into account the appropriate value of Mrp=0.0082 with 5h of annealing, the effective decay time is τ_{eff}=84 μs, about ~3 times larger than non-surfactant sample, with 115 μs for slow decay time that is in agreement with reported results for different host [29,31].

Table 2.5: Luminescence decay time as function of Pluronic F-127 concentration.

Sample 0.2 mol% Er	Fast decay time (μs)	Slow decay time (μs)	Effective decay time (μs)
Mrp=0-5h	26	--	26
Mrp=0.0082-5h	85	115	84
Mrp=0.0082-0h	38	48	39
Mrp=0.01-5h	81	107	85

The enlargement of fast decay time suggests a reduction of OH^- as is indicated in Figure 2.5. Interestingly, for high surfactant concentration (Mrp=0.01) but same annealing process, the effective decay time is the same, even that particle size diminished 20 nm. Sample with optimum composition of surfactant but annealed 0 min, produced a 54 nm particle size and its effective decay time diminished, being ~50% faster than sample annealed 5 h. These

results, and considering also the particle size of sample prepared without surfactant, suggest that luminescence decay time is dominated by surface impurities and perhaps by defects produced by the large surface-to-volume ratio [32].

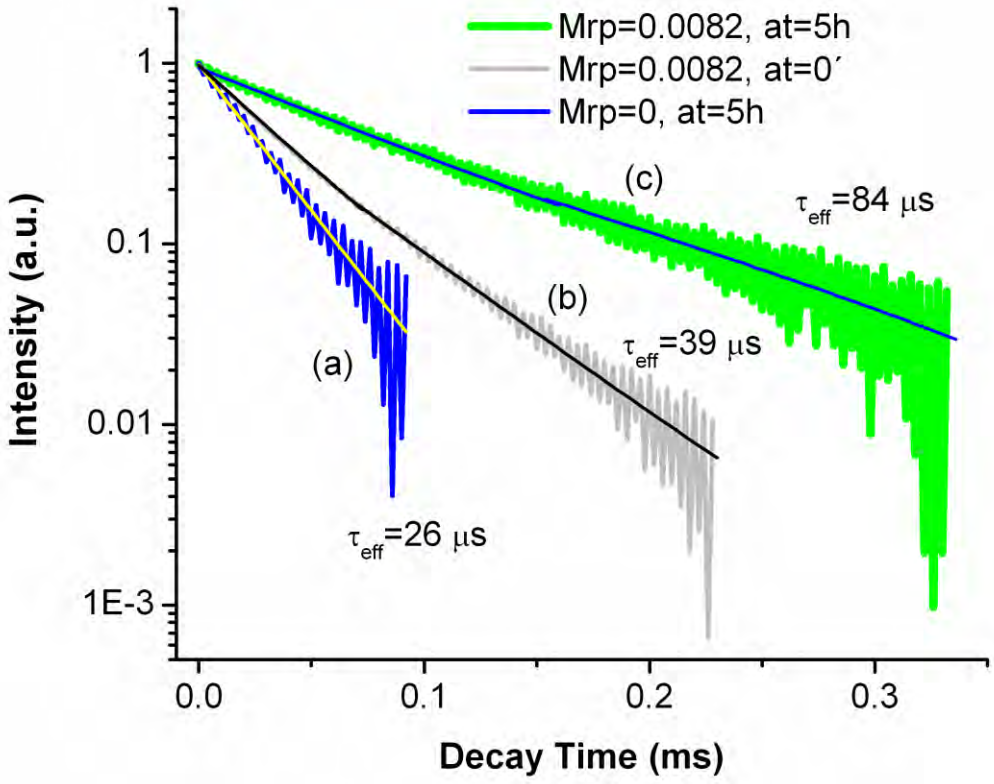

Figure 2.18: Luminescence decay times at 550 nm for $ZrO_2:Er^{3+}$ samples under 970 nm excitation: (a) Mrp=0 at 1000 ^oC-5h, (b) Mrp=0.0082 at 1000 ^oC-0 min and (c) Mrp=0.0082 at 1000 ^oC-5h.

Probably, the mayor contribution of fast decay time is produced by ions close or on the surface of nanocrystals, as has been suggested [32]. For a particle much smaller than the wavelength of emitted signal, the decay time of nanoparticles (τ_{np}) should be inversely proportional to the refractive index of the surroundings medium (n_s). The decay time of bulk and nanocrystals are related by the expression [33]:

$$\tau_{np} = \tau_{bc} \frac{n_{bc}}{n_{eff}} \qquad (2.14)$$

Here, τ_{bc} and n_{bc} stand for decay time and refractive indexes of bulk crystal, respectively. The effective refractive index is calculated by $n_{eff} = (1-x)\cdot n_s + x \cdot n_{bc}$ [34]. Here, *x* is the "filling factor" that is the space fraction occupied by the nanoparticles. The smaller the nanoparticle, the larger the decay time. Such enlargement of τ_{np} was observed as is shown in Tables 2.2 and 2.5. However, for sample with Mrp=0.01 not enlargement was observed even that particle size was reduced. In this particular case, it has been observed a higher concentration of impurities such as OH and CO_2. Furthermore, the lower crystallite size increase the surface defects that induce deleterious effect on optical properties. This suggests that the effect of impurities is stronger than the nanosize effect. The reduction on particle size enlarges but impurities and surface defects shorten the decay time. Impurities' effect is observed in the sample annealed for 0 min, where decay time is notably reduced even though particle size was reduced.

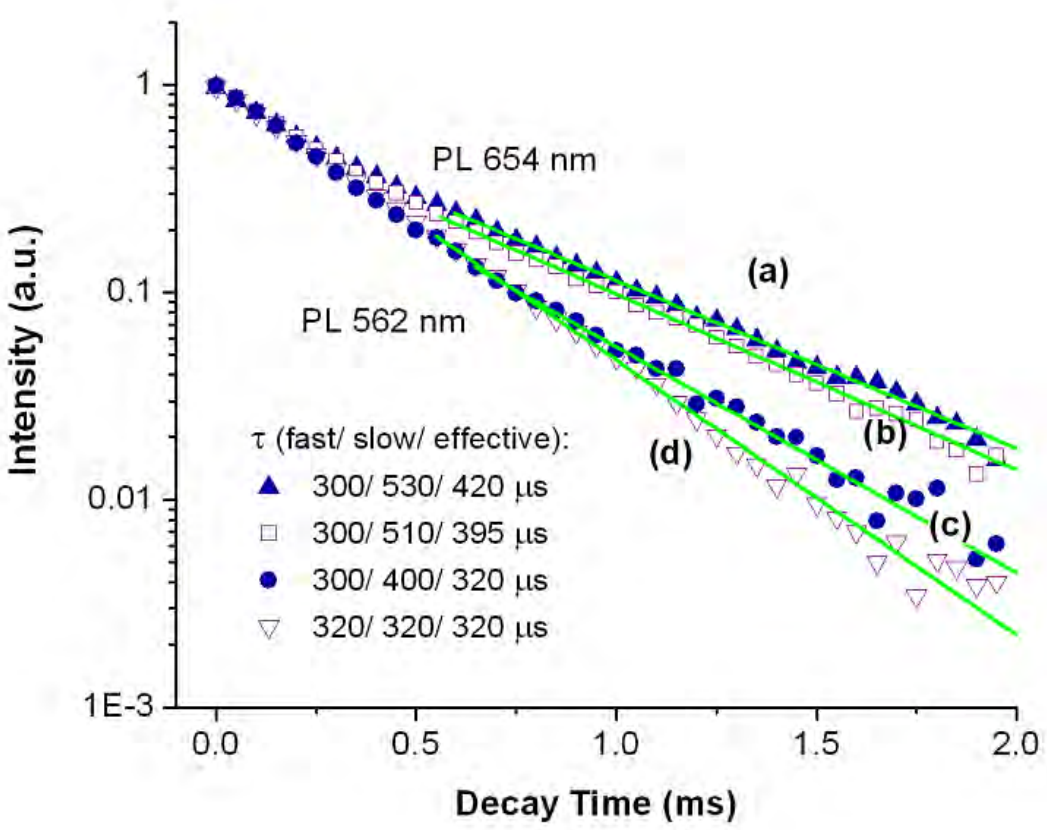

Figure 2.19: Luminescent decay times of $ZrO_2:Yb^{3+}$-Er^{3+} samples under 970 nm excitation: at 654 nm for (a) Mrp=0.0082 and (b) Mrp=0; at 562 nm for (c) Mrp=0.0082 and (d) Mrp=0.

The introduction of Yb as sensitizer enlarges luminescence decay time. Such enlargement, independent of surfactant, is the result of the energy transfer process from Yb to Er. Yb^{3+}-Er^{3+} codoped nanocrystals also present an increment on effective decay time with the use of surfactant. Figure 2.19 shows the corresponding decay time plot for 562 and 654 nm. The effective decay time was 320 μs for green band on both non surfactant and surfactant prepared samples. However, the former was fitted to single exponential and the second one present a slow component decay time of 400 μs that means an increment of ~22%. The effective decay time of red band was 395 and 420 μs, only ~ 5% of increment. Notice the stronger difference between fast and slow decay times; fast components are ~300 μs for both prepared samples and ~510 μs and ~530 μs for non surfactant and surfactant slow components, respectively. Figure 2.20 shows the corresponding decay time plot for NIR emitted signal.

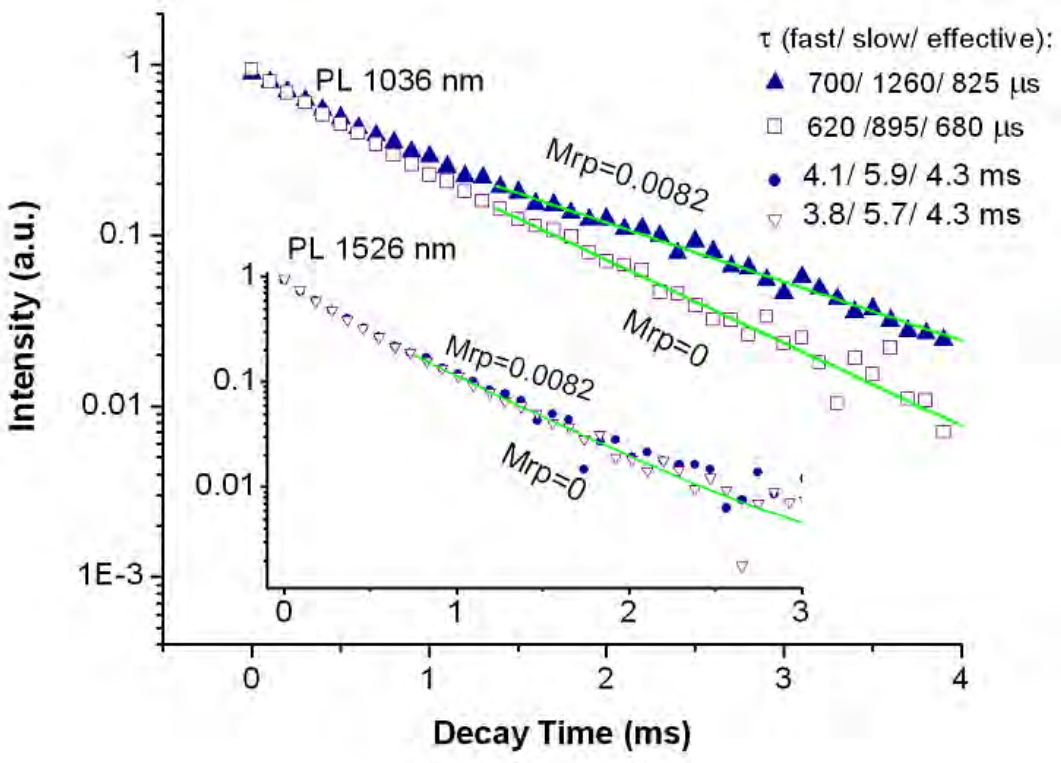

Figure 2.20: Luminescence decay times of ZrO_2:Yb^{3+}-Er^{3+} samples under 970 nm excitation in the 1036 nm emission band associated to $^4F_{5/2}$ energy level of Yb. The inset shows the decay times of 1526 nm emission band associated to $^4I_{11/2}$ energy level of Er.

The enhancement of effective decay time (4.3 ms) for 1.5 μm emitted signal is marginal, only 0.5%. However, an increment of ~8% and ~3% was observed for fast and slow decay time, respectively. Interestingly, the effective decay time for Yb emission is 825 μs that represents an increment of 21% compared to sample prepared without surfactant (680 μs). Notice the strong difference (40%) of slow decay time, 895 μs and 1.26 ms, for non-surfactant and surfactant prepared samples. This longer decay time makes energy transfer more favorable resulting in higher green and red luminescence.

Experimental results have confirmed the intensity enhancement and larger decay times of emitted signal, induced by the use of PLURONIC F-127 during the synthesis process. As discussed before, surfactant not only affects optical properties but also the phase composition and particle dispersion. All together, it improves nanocrystals and increases the potential for different applications.

2.5. REFERENCES

[1] H. Song, B. Sun, T. Wang, S. Lu, L. Yang, B. Chen, X. Wang, and X. Kong, "Three-photon upconversion luminescence phenomenon for the green levels in Er^{3+}/Yb^{3+} codoped cubic nanocrystalline yttria", Solid State Commun. **132**(6), 409–413 (2004)

[2] J.A. Capobianco, F. Vetrone, J.C. Boyer, A. Speghini, M. Bettinelli, "Enhancement of Red Emission ($^4F_{9/2}$--$^4I_{15/2}$) via Upconversion in Bulk and Nanocrystalline Cubic $Y_2O_3:Er^{3+}$", The Journal of Physical Chemistry B **106**, 1181 (2002)

[3] A. Patra, C. S. Friend, R. Kapoor, and P. N. Prasad, "Upconversion in $Er^{3+}:ZrO_2$ Nanocrystals," The Journal of Physical Chemistry B **106**, 1909-1912 (2002)

[4] E. De la Rosa-Cruz, L.A. Diaz-Torres, R.A. Rodriguez-Rojas, M.A. Meneses-Nava, O. Barbosa-Garcia, P. Salas, Applied Physics Letters **83**, 4903-4905 (2003)

[5] L.A. Diaz-Torres, E. De la Rosa-Cruz, P. Salas, C. Angeles-Chavez, "Concentration enhanced red upconversion in nanocrystalline ZrO_2 : Er under IR excitation", J. Phys. D: Appl. Phys. **37** (2004) 2489

[6] E. De la Rosa-Cruz, L.A. Diaz-Torres, R.A. Rodriguez-Rojas, M.A. Meneses-Nava, O. Barbosa-Garcia, P. Salas, Applied Physics Letters **83**, 4903-4905 (2003)

[7] A. Patra, S. Saha, M. Alencar, N. Rakov, G. S. Maciel, "Blue upconversion emission of Tm3+-Yb^{3+} in ZrO_2 nanocrystals: Role of Yb^{3+} ions," Chem. Phys. Lett. **407**(4-6), 477-481 (2005)

[8] E. De la Rosa, P. Salas, H. Desirena, C. Angeles, R. A. Rodriguez, "Strong green upconversion emission in ZrO_2 : Yb^{3+}-Ho^{3+} nanocrystals," Applied Physics Letters, **87**(24), (2005)

[9] P.K. Sharma, M.H. Jilavi, R. Nass, H. Schmidt, "Tailoring the particle size from μm→nm scale by using a surface modifier and their size effect on the fluorescence properties of europium doped yttria - The Physics and Chemistry of Sol Gel Processing", Journal of Luminescence **82**, 187-193 (1999)

[10] W. Córdova-Martínez, E. De la Rosa-Cruz, L.A. Díaz-Torres, P. Salas, A. Montoya, M. Avendaño, R.A. Rodríguez, O. Barbosa-García, "Nanocrystalline tetragonal zirconium

oxide stabilization at low temperatures by using rare earth ions: Sm^{3+} and Tb^{3+}", Opt. Mater. **20**, 263 (2002)

[11] B.D. Cullity, (Ed.), Elements Of X Ray Diffraction, Addison-Wesley Publishing Company, Inc., Massachusetts, 1956

[12] S.J. Hong, J.I. Han, "Effect of synthetic conditions on particle size and photo-luminescence properties of Y_2O_3:Eu^{3+} nanophosphor", Journal of Electroceramics **18**, 67-71 (2007)

[13] G. De, W. Qin, J. Zhang, J. Zhang, Y. Wang, C. Cao, Y. Cui, "Effect of OH on the upconversion luminescent efficiency of Y_2O_3:Yb^{3+}, Er^{3+} nanostructures", Solid State Communications **137**, 483-487 (2006)

[14] T. Lopez-Luke, E. De la Rosa, P. Salas, C. Angeles-Chavez, L.A. Diaz-Torres, S. Bribiesca, "Enhancing the up-conversion emission of ZrO_2 : Er^{3+} nanocrystals prepared by a micelle process", Journal of Physical Chemistry C **111**, 17110-17117 (2007)

[15] S. Tanabe, T. Ohyagi, N. Soga, T. Hanada, "Compositional dependence of Judd-Ofelt parameters of Er^{3+} ions in alkali-metal borate glasses", Phys. Rev. B **46**, 3305-3310 (1992)

[16] V.P. Gapontsev, S.M. Matitsin, A.A. Isineev, V.B. Kravchenko, "Erbium glass lasers and their applications", Opt. Laser Technol. **14**, 189-196 (1989)

[17] B-C. Hwang, S. Jiang, T. Luo, J. Watson, G. Sorbello, N. Peyghambarian, "Cooperative upconversion and energy transfer of new high Er^{3+} and Yb^{3+} – Er^{3+} doped phosphate glasses", J. Opt. Soc. Am. B **17**, 5, 833-839 (2000)

[18] J.A. Capobianco, A. Speghini, F. Vetrone, M. Bettinelli, T. D'Alesio, and G. Tessari, "Optical spectroscopy of nanocrystalline cubic Y_2O_3: Er^{3+} obtained by combustion synthesis," Chemistry Chemical Physics **2**, 3203–3207 (2000)

[19] I. Hyppänen, J. Hölsä, J. Kankare, M. Lastusaari, and L. Pihlgren, "Upconversion Properties of Nanocrystalline ZrO_2:Yb^{3+}, Er^{3+} Phosphors," Journal of Nanomaterials **2007**, 16391 (2007)

[20] M. Pollnau, D. Gamelin, S. Lüthi, H. Güdel, and M. Hehlen, "Power dependence of upconversion luminescence in lanthanide and transition-metal-ion systems," Physical Review B 61,3337-3346 (2000)

[21] G. Tessari, M. Bettinelli, A. Speghini, D. Ajò, G. Pozza, L. E. Depero, B. Allieri, and L. Sangaletti, "Synthesis and optical properties of nanosized powders: lanthanide-doped Y2O3," Applied Surface Science 144-145, 686-689 (1999)

[22] E. Nakazawa, "Phosphor handbook", S. Shionoya, W.M. Yen (eds.), CRC Press, Boca Raton, FL(1999)

[23] Y. Guyot, H. Canibano, C. Goutaudier, A. Novoselov, A. Yoshikawa, T. Fukuda, and G. Boulon, "Yb^{3+}-doped $Gd_3Ga_5O_{12}$ garnet single crystals grown by the micro-pulling down technique for laser application. Part 2: Concentration quenching analysis and laser optimization," Optical Materials **28**, 1-8 (2006)

[24] M. Liu, S. Wang, J. Zhang, L. An, and L. Chen, "Upconversion luminescence of $Y_3Al_5O_{12}$ (YAG):Yb^{3+}, Tm^{3+} nanocrystals," Optical Materials **30**, 370-374 (2007)

[25] W. Lu, L. Cheng, H. Zhong, J. Sun, J. Wan, Y. Tian, and B. Chen, "Dependence of upconversion emission intensity on Yb^{3+} concentration in Er^{3+} /Yb^{3+} co-doped flake shaped Y_2 $(MoO_4)_3$ phosphors," Journal of Physics D: Applied Physics **43**, 085404 (2010)

[26] M. Inokuti and F. Hirayama, ”Influence of energy transfer by the exchange mechanism on donor luminescence”, J. Chem. Phys. **43**, 1978-1989 (1965)

[27] T. Lopez-Luke, E. De la Rosa, D. Solis, P. Salas, C. Angeles-Chavez, A. Montoya, L. A. Diaz-Torres, and S. Bribiesca, "Effect of the CTAB concentration on the up-conversion emission of ZrO_2 : Er^{3+} nanocrystals," Optical Materials **29**, 31-37 (2006)

[28] G.Y. Chen, G. Somesfalean, Y. Liu, Z.G. Zhang, Q. Sun, F.P. Wang, “Upconversion mechanism for two-color emission in rare-earth-ion-doped ZrO_2 nanocrystals”, Physical Review B **75**, 195204-6 (2007)

[29] F. Vetrone, J.C. Boyer, J.A. Capobianco, A. Speghini, M. Bettinelli, “Concentration-dependent near-infrared to visible upconversion in nanocrystalline and bulk Y_2O_3 : Er^{3+}”, Chemistry of Materials **15**, 2737-2743 (2003)

[30] G. De, W. Qin, J. Zhang, J. Zhang, Y. Wang, C. Cao, Y. Cui, “Upconversion luminescence properties of Y_2O_3:Yb^{3+},Er^{3+} nanostructures”, Journal of Luminescence **119-120**, 258-263 (2006)

[31] S. Shionoya, (Ed.), Phosphor handbook, CRC Press, Boca Raton, FL, 1999

[32] H. Guo, M. Yin, N. Dong, M. Xu, L. Lou, W. Zhang, "Effect of heat-treatment temperature on the luminescent properties of Lu_2O_3:Eu film prepared by Pechini sol-gel method", Applied Surface Science **243**, 245-250 (2005)

[33] H.P. Christensen, D.R. Gabbe, H.P. Jenssen, "Fluorescence lifetimes for neodymium-doped yttrium aluminum garret and yttrium oxide powders", Physical Review B **25**-3 (1982)

[34] R.S. Meltzer, S.P. Feofilov, B. Tissue, "Dependence of fluorescence lifetimes of Y_2O_3 : Eu^{3+} nanoparticles on the surrounding medium", H.B. Yuan, Phys. Rev. B **60**, 14012 (1999)

CHAPTER 3

LUMINESCENCE PROPERTIES OF

$ZrO_2:Yb^{3+}$, Ho^{3+} NANOCRYSTALS

3.1. INTRODUCTION

The rare-earth doped nanophosphors emitting in the visible range (via up-conversion process) have received special attention. They offer the possibility for alternative solid-state hosts capable of producing efficient frequency up-conversion processes [1]. Perhaps the most studied system designed to generate green light is the Er ion embedded in different hosts. However, trivalent holmium has several emission lines in the NIR spectral range that can be excited with NIR photons via several metastable energy levels ($^5I_6$ and $^5I_7$) of Ho^{3+}, which act as good population reservoirs for potential energy transfer (ET) or excited-state absorption (ESA) processes [2]. Infrared-to-visible up-conversion emission has been investigated in holmium-doped crystals under excitation of photons in the red-infrared range [3-7], and only in few of them visible up-conversion emission is produced using a 970 nm source [8,9].

In general, codoping rare-earth ions with Yb^{3+} increases the efficiency of the UC process, and in some cases can induce up-conversion where it would not be possible with a single ion such as Tm^{3+} and Ho^{3+} even in a different host [2,10]. The large spectral overlap between Yb^{3+} emission ($^2F_{5/2} \rightarrow {}^2F_{7/2}$) and Ho^{3+} absorption ($^5I_8 \rightarrow {}^5I_5$) results in an efficient resonant energy transfer in Yb^{3+} - Ho^{3+} codoped systems. Thus, the luminescence properties of Ho^{3+} doped zirconium dioxide nanocrystals deserve further study. Furthermore, in ZrO_2: Er^{3+} a relation between the luminescent efficiency and particle size, the reduction of the organic remnants, and the phonon energy of the host has been reported [11,12]. For this section, ZrO_2:Yb^{3+}-Ho^{3+} nanocrystals with different concentrations of codopants were synthesized with surfactant (Pluronic F-127). The up-converted signal produced by the codoped nanocrystals present almost pure green emission centered at 540 nm. Obtaining stronger green signal was considered as an aim in this section, as well as the related Yb/Ho composition and decay time involved. Procedures to calculate color coordinate and maximum luminance after excitation were proposed. Up-converted signal are explained in terms of the energy transfer from donor (Yb) to acceptor (Ho). The energy transfer efficiency is analyzed, through samples, in order to determine correlation with ion concentration of Ho.

3.2. EXPERIMENTAL PROCEDURE

The synthesis of Er^{3+} and Yb^{3+}-Ho^{3+} doped ZrO_2 nanophosphors were prepared by a micelle method, with holmium chloride ($HoCl_3 \cdot 6H_2O$) and Pluronic F-127 (at molar ratio of 0.0082) added to the solution. All samples were annealed at 1000^{o}C and kept there for 5h. This process has been described in detail on section 2.2. In this instance erbium precursor is replaced with holmium precursor.

The set-up for the X-ray diffraction (XRD) and photoluminescence (PL) characterization is the same as described on section 2.2 for ZrO_2:Yb^{3+}–Er^{3+} samples. Transmission electron microscopy was carried out in a JEM-2200FS system with an accelerating voltage of 200 kV. The microscope is equipped with a Schottky-type field emission gun, an ultra high resolution (UHR) configuration (Cs=0.5 mm, Cc=1.1 mm, 0.19 nm point-to-point resolution), and an omega-type in-column energy filter. High angle annular dark field (HAADF) images were obtained using an annular dark field detector. The samples were grounded, suspended in isopropanol at room temperature, and dispersed with ultrasonic agitation. An aliquot of the solution was then dropped on a 3 mm diameter lacey carbon copper grid.

3.3. STRUCTURAL PROPERTIES

The XRD patterns for the ZrO_2:Yb^{3+}-Ho^{3+} nanocrystals are shown in Figure 3.1. The crystalline phase composition after 5 h annealing at 1000°C with surfactant are primarily tetragonal and slightly monoclinic, for both Yb^{3+} doped and Yb^{3+}-Ho^{3+} codoped samples. Table 3.1 lists the phase composition for different concentrations of the active ions estimated using the expression from equation 2.1. This confirms the influence that ion concentration has on the stabilization of the tetragonal phase (specifically the Yb ion), as was previously reported [13].

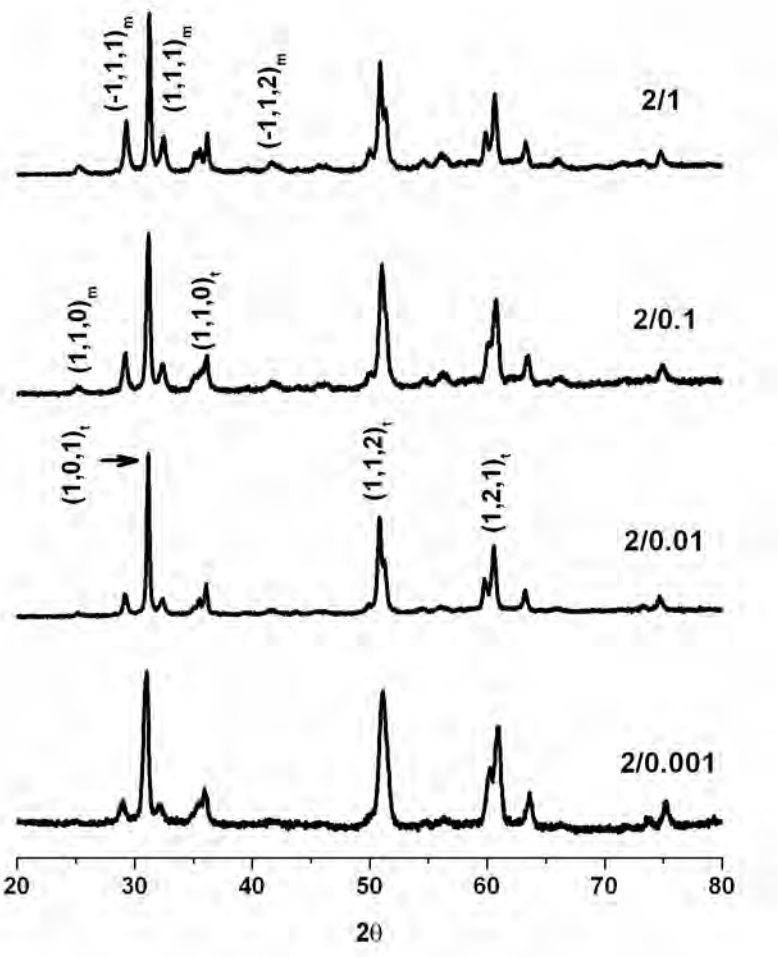

Figure 3.1: XRD patterns of ZrO_2:Yb^{3+} - Ho^{3+} nanocrystals for different concentrations of Ho^{3+} codoped with 2 mol% of Yb^{3+}.

Interestingly, the tetragonal phase for a pure Yb^{3+} doped sample changed from 65% to 77% after the addition of a very small quantity (0.01 mol%) of Ho^{3+}. However, the content of tetragonal phase was reduced for larger concentrations of Ho^{3+}, being 62 wt% for 1 mol% of Ho^{3+} and 2 mol% of Yb^{3+} doped samples. This behavior is in opposite to previous results reported recently [14], although the physical mechanism has not been elucidated. For concentrations lower than 0.01 mol%, the tetragonal phase concentration diminishes approaching its phase composition to one for a pure Yb^{3+} doped sample. For low dopant concentrations, the tetragonal crystalline structure is mostly affected by the annealing time and temperature.

Table 3.1: Phase composition and crystallite size of ZrO_2:Yb^{3+} - Ho^{3+} nanocrystals.

Sample concentration (mol%)		Phase composition (wt.%)		Cristallite size
Yb	Ho	Cm	Ct	(nm)
2	1	38.2	61.8	27.479
2	0.1	33.7	66.3	20.622
2	0.01	23.0	77.0	29.436
2	0.001	30.0	70.0	15.875
2	0	35.1	64.9	25.758

An increase in pattern broadness relating to 0.001 mol% of dopant can be appreciated on the XRD patterns in Figure 3.1. Such broadness suggests a notable decrease in crystallite size. Strain on the lattice also contributes to the broadening, but crystallite size is a more critical factor. Moreover, the strain effect is directly related to the crystallite surface area, which is dependent on crystallite size. This difference pattern broadness suggests that an increase in particle size dispersion arrests the crystallite growth, hindering the conversion from tetragonal to monoclinic. The stabilization of *t*-ZrO_2 via the crystallite size effect is based on the assumption that the free surface energy in nanocrystalline tetragonal zirconia is lower than that in normal monoclinic phase. Therefore, this additional effect is maintained in samples with lower crystallite size [15].

The crystallite size was calculated using Sherrer's equation from expression 2.2. The average crystallite size is 24 nm for the group of samples with constant value of 2 mol% Yb^{3+} with different concentrations of Ho^{3+}. With the lowest concentration of Ho^{3+}, 0.001 mol%, the average crystallite size decreased to 16 nm. The largest crystallite size was 29 nm and was obtained for 0.01 mol%. The crystallite sizes for different concentrations of Ho^{3+} are also shown in Table 3.1. These values seem to indicate that prepared samples do not present a consistent correlation between average crystallite size and an increase in the concentration of

Ho^{3+}. As will be discussed later, the best luminescent sample had both high tetragonal composition, and a smaller crystallite size.

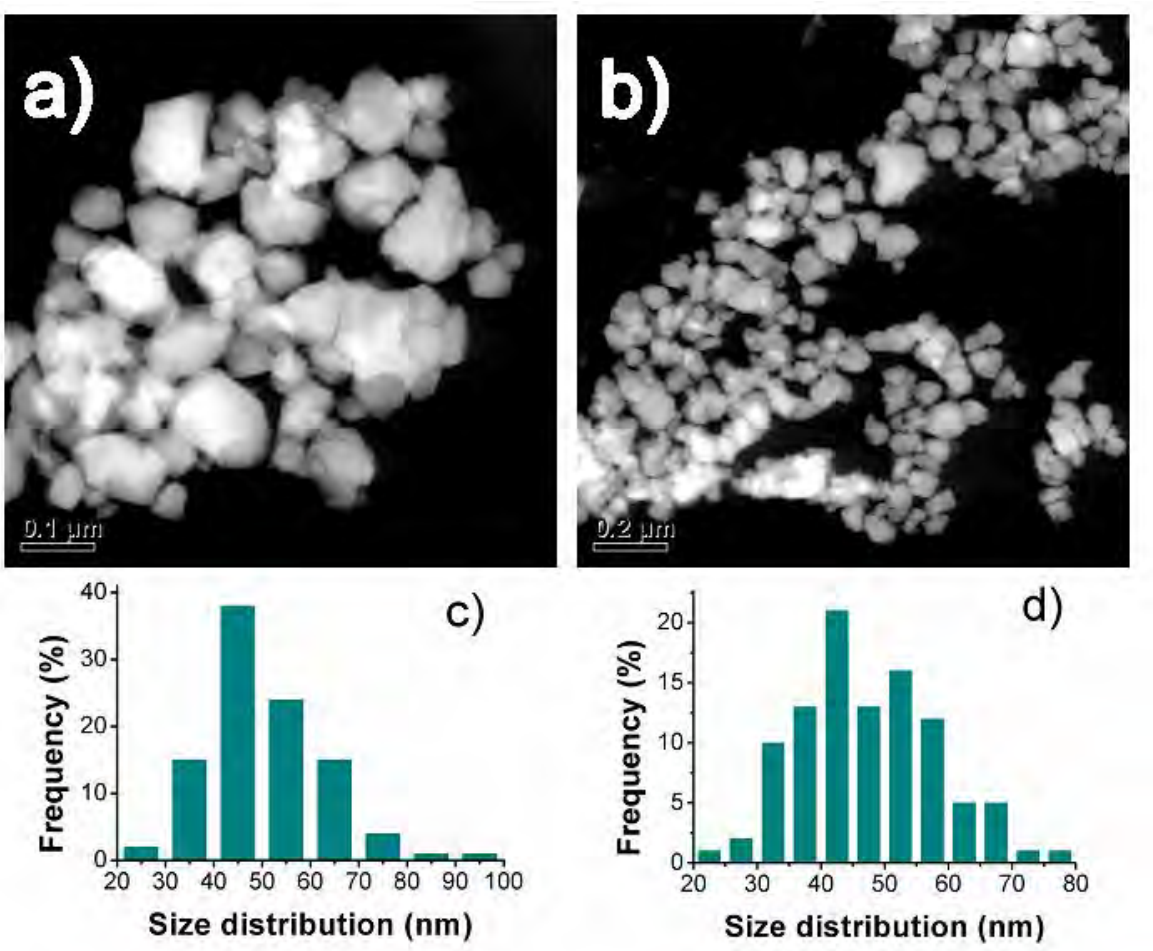

Figure 3.2: HAADF STEM images of ZrO_2:Yb^{3+} - Ho^{3+} nanocrystals for (a) 2/0.01 mol% of Yb^{3+}/Ho^{3+} and (b) 2/1 mol%. (c) and (d) show the crystallite size distribution for both samples.

The dispersion capability of the surfactant Pluronic F-127 can be observed in the HAADF STEM images shown in Figure 3.2. The introduction of surfactant keeps the nanocrystals well dispersed, even for a long annealing time. In addition, by reducing the annealing temperature both crystallite size and agglomeration are reduced [11]. From the size distribution chart, the average particle size is between 50 and 47 nm for 2/0.01 and 2/1 mol%, respectively. Compared to the size calculated with Sherrer's equation from the XRD (listed in Table 3.1), the average crystallites per particle is around 1.7. This implies that surfactant is beneficial for

the dispersion of powders, and can be concluded that samples prepared with Pluronic F-127 present higher crystallite distribution.

3.4. LUMINESCENCE PROPERTIES

The emission spectra of codoped ZrO_2:Yb^{3+} - Ho^{3+} nanophosphors (shown in Figures 3.3 and 3.4), exhibits four distinct emission bands resulting from the up-conversion process. The red band centered on 650 nm associated to the relaxation of $^5F_5 \rightarrow {}^5I_8$, and the NIR band centered on 760 nm attributed to the $^5F_4 + {}^5S_2 \rightarrow {}^5I_7$ relaxation, are one order of magnitude lower than the green band centered on 550 nm and attributed to the $^5F_4 + {}^5S_2 \rightarrow {}^5I_8$ relaxation of Ho^{3+}. There is also a weak band (not showed here) two orders of magnitude lower and centered on 490 nm associated to the $^5F_3 \rightarrow {}^5I_8$ Ho^{3+} transition. The strong green emission band contains about 98% of the total emitted signal obtained after excitation at 970 nm. All bands show a strong dependence on the concentration of both ions. Figures 3.3a and 3.4a show the up-converted signal obtained with constant 1 mol% of Ho^{3+} concentration and different concentration of sensitizer (Yb^{3+}). Both, green and NIR emission band increases with the increment of sensitizer. However, the highest signal emitted was obtained for 2 mol% of Yb^{3+}. For larger concentration, both bands were quenched but green band was quenched stronger. Interestingly, the intensity of the red band increases monotonically with the increment of sensitizer, see Figure 3.4a. The increment of Yb^{3+} concentration induces an increment of the signal intensity but does not produce any structural change in the emission spectra.

Figures 3.3b and 3.4b shows the up-converted signal obtained with a constant 2 mol% Yb^{3+} concentration, where maximum emission was obtained, and different concentration of Ho^{3+}. Interestingly, all bands increase in intensity when the concentration of Ho^{3+} is decreased, even for three orders of magnitude lower than 1 mol%. However, the red band reach its maximum at 2/0.01 mol% of Ho^{3+} and decrease for lower concentration. The visible up-converted spectra for each sample was integrated and normalized with the brightest sample, allowing analysis of luminescence intensity as a function of ion concentration, see Figure 3.5. The previous maximum green signal was obtained for 2 mol% of Yb^{3+} and 1 mol% of Ho^{3+}.

However, a 600% optimization can be observed for very low concentrations of Ho^{3+}. The highest emitted signal was achieved with a concentration of 2 mol% of Yb^{3+}, and only 0.001 mol% of Ho^{3+}, as is shown in Figure 3.5.

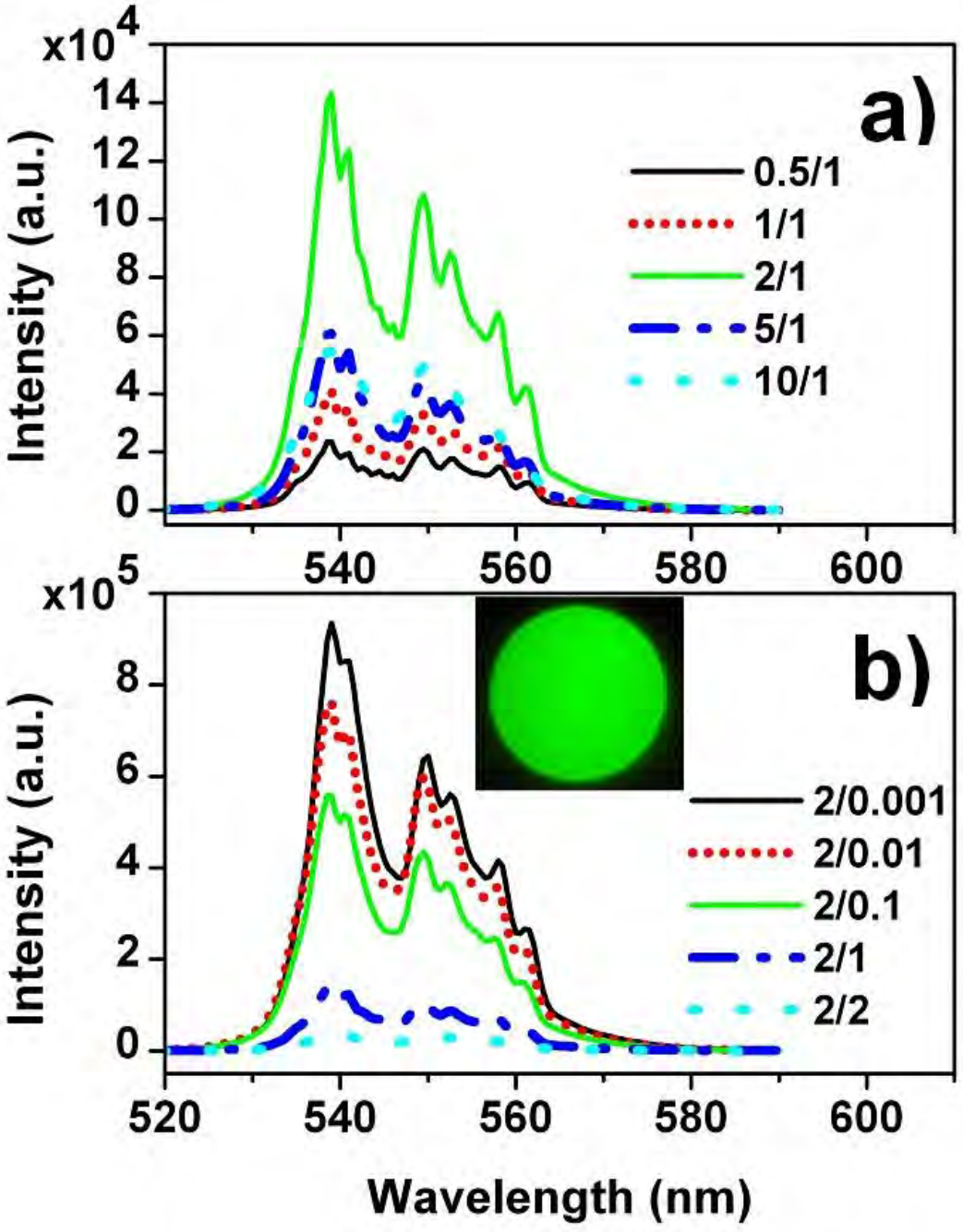

Figure 3.3: Emission spectra of ZrO_2:Yb^{3+} - Ho^{3+} nanophosphors with a) 1 mol% Ho^{3+} at different concentration of Yb^{3+}, and b) 2 mol% Yb^{3+} at different concentration of Ho^{3+}. Inset shows a picture of the bright emission of (Yb/Ho) 2/0.001 mol% codoped sample.

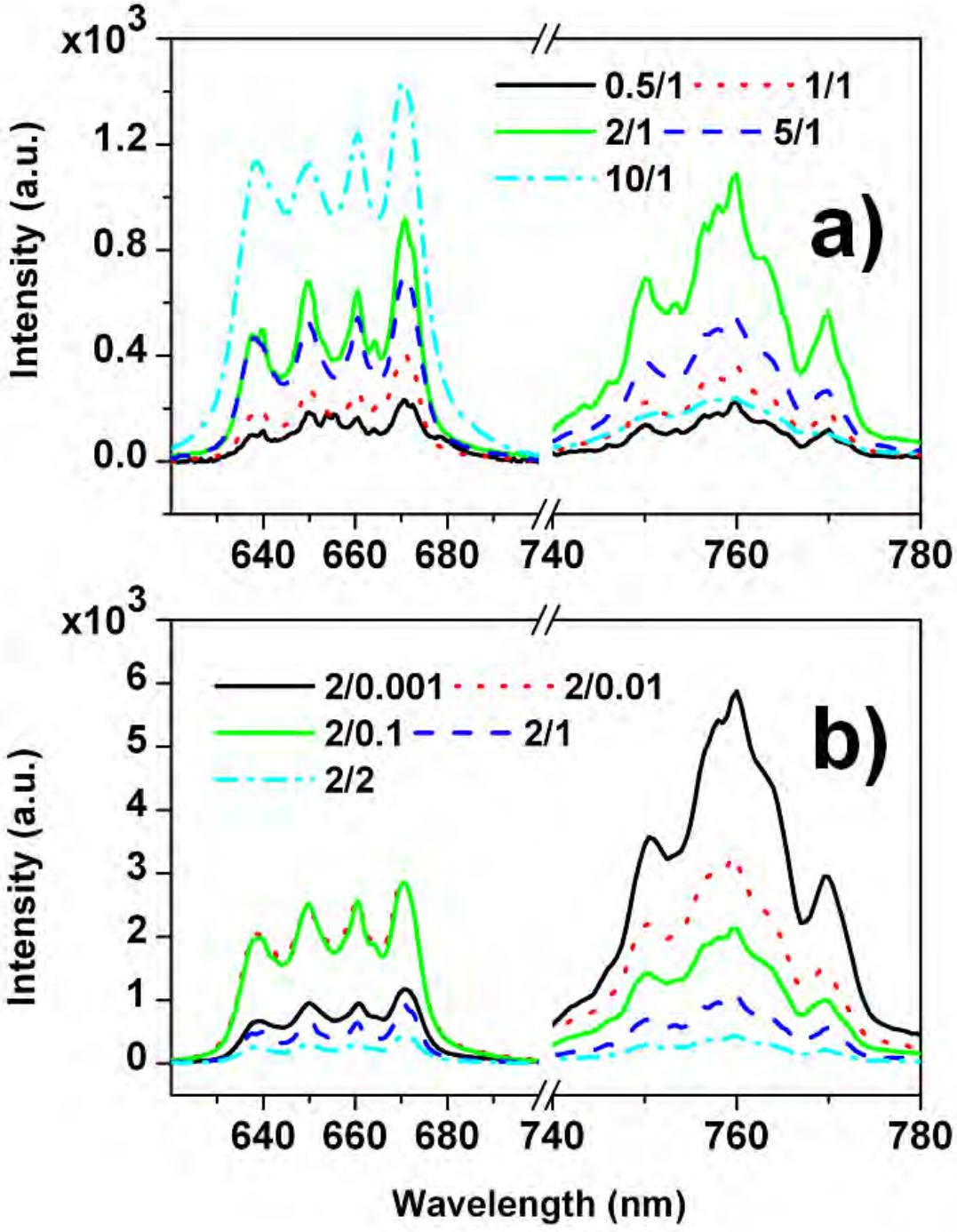

Figure 3.4: Red and NIR emission band of ZrO_2:Yb^{3+} - Ho^{3+} nanophosphors with a) 1 mol% Ho^{3+} and different concentration of Yb^{3+}, and b) 2 mol% Yb^{3+} and different concentration of Ho^{3+}.

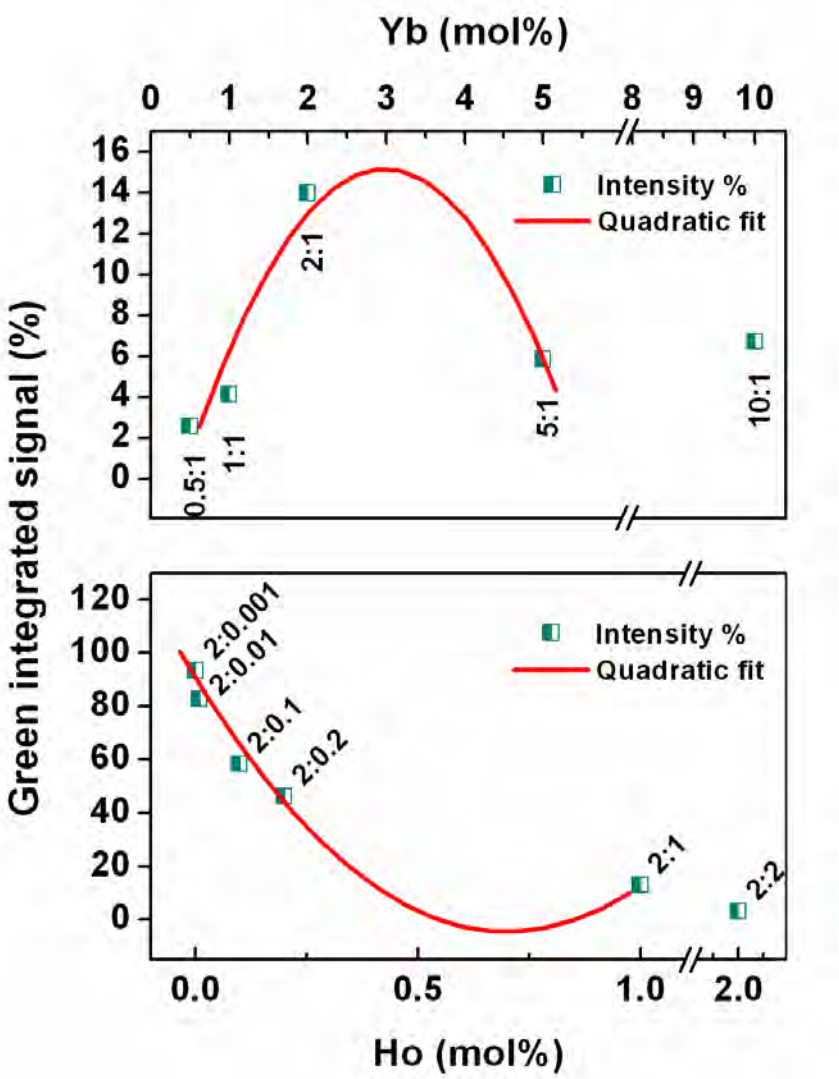

Figure 3.5: Integrated up-converted signal as a function of Yb^{3+} concentration with 1 mol% of Ho^{3+} (up) and Ho^{3+} concentration with 2 mol% of Yb^{3+} (down).

This strong increase in emitted signal can be attributed to the reduction of Ho^{3+} inter-ionic interactions and then a reduction of ion agglomeration. This means, a reduction of energy migration because of an increment of separation between Ho^{3+} ions. These results highlight the considerable influence of Ho^{3+} on the UC signal and remark the very low threshold of concentration for agglomeration. Although both figures show a remarkably different trend for ion concentrations, they both have a partial quadratic fit which suggests that energy transfer up-conversion (ETU) is the dominant transition, since it varies quadratically with ion concentration [16]. In this process, two different types of ions in close proximity are excited

to an intermediate level. They are coupled by a non-radiating process in which one relaxes to a lower state transferring the energy (donor), while the other ion take the energy (acceptor) being excited to an upper state. Additional evidence of the Yb^{3+} - Ho^{3+} energy transfer is observed by analyzing the intensity change of the characteristic Yb^{3+} emission centered at 1039 nm. Figure 3.6 shows the NIR emission spectra for 2 mol% of Yb^{3+} with and without 1 mol% Ho^{3+}. A clear decrease in NIR signal emitted is observed with the presence of Ho^{3+}, suggesting the presence of an ET process.

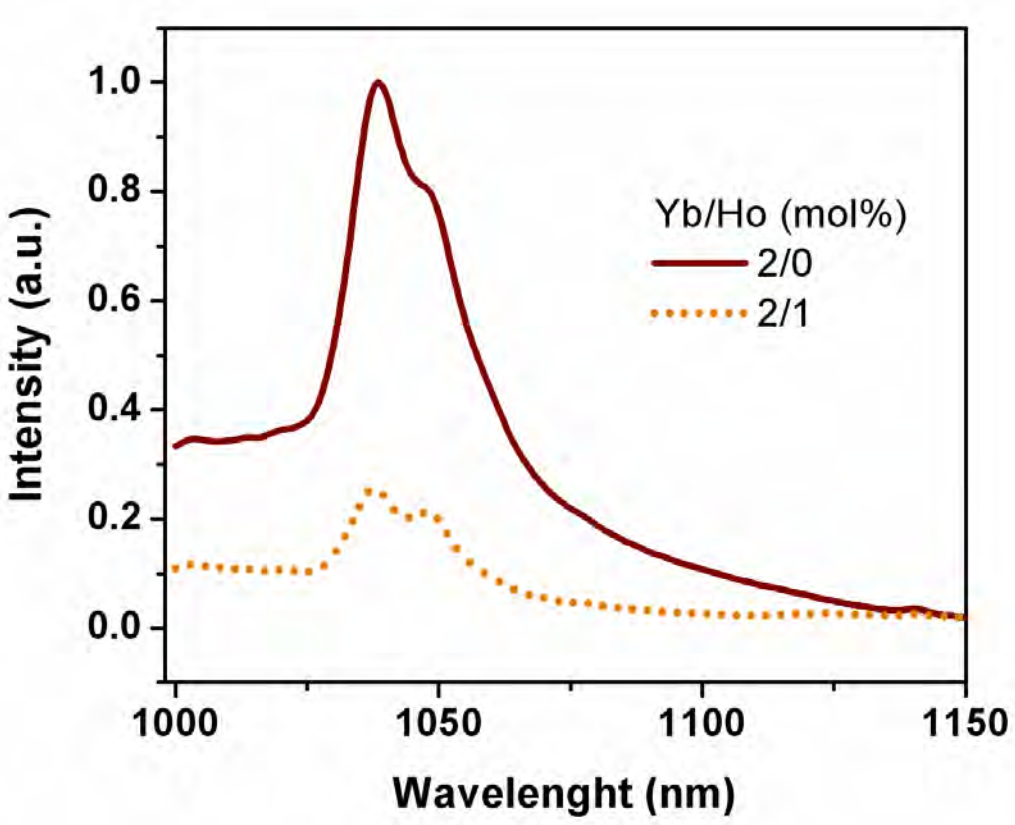

Figure 3.6: Characteristic emission of Yb^{3+} ion centered at 1039 nm.

Analyzing the integrated signal intensity I_{uc} as a function of the pumping intensity I_{pump}, it is possible to determine the number of photons involved in the UC process (previously considered an ETU). This dependence is expressed by the equation

$$I_{uc} = kI_{pump}^{n} \tag{3.1}$$

where *n* denotes the number of photons absorbed to produce the up-converted emission. Figure 3.7 shows the behavior of the integrated green emission band versus the excitation power for three different concentrations of codopants Yb/Ho at 2/0.001, 2/1, and 5/1 mol%. In all cases, the values of $n \approx$ 1.3, 1.7 and 1.9 suggest the presence of a two photon absorption mechanism in the UC emission, which is in agreement with previous results [2]. Notice that for low concentration of Ho^{3+} alternative processes become more relevant and could explain the small value of *n*.

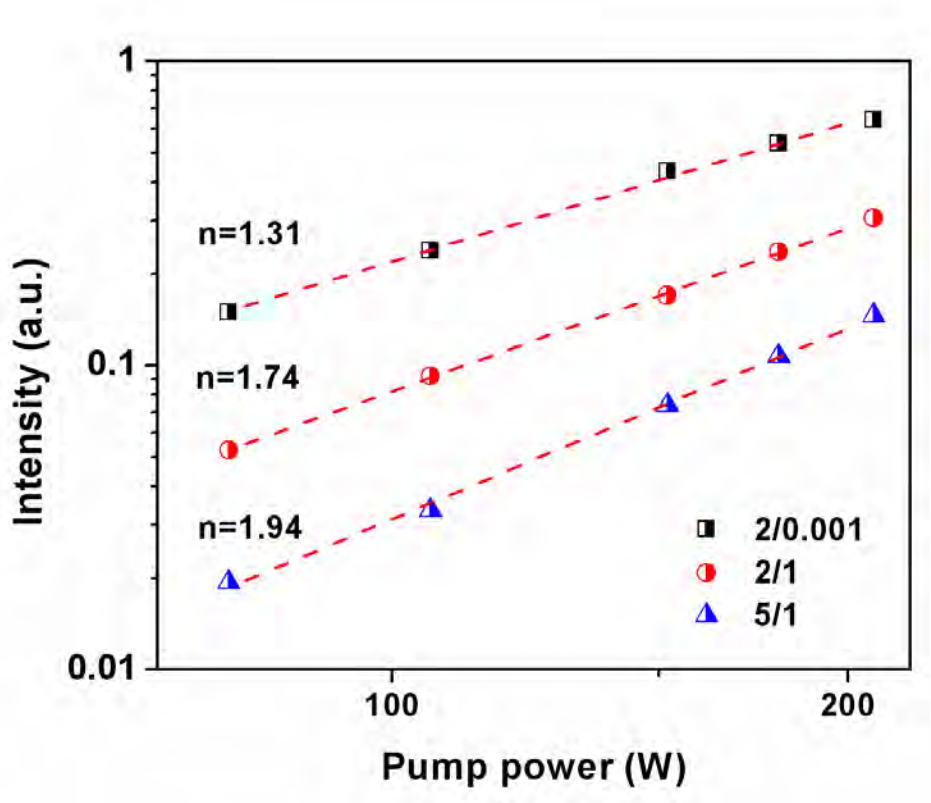

Figure 3.7: Dependence of the integrated up-converted signal intensity with pumping power excitation for different concentrations of Ho^{3+}.

3.4.1. UP-CONVERSION EMISSION MECHANISM

The proposed mechanism associated to the up-conversion emission of Ho^{3+} is described on the energy level diagram shown in Figure 3.8. Ho^{3+} ion (acceptor) is excited by the energy transfer (ET) from the $^2F_{7/2} \rightarrow {}^2F_{5/2}$ transition of Yb^{3+} (donor) that is excited directly by the pumping signal. Direct excitation of Ho^{3+} ion is also possible, however energy transfer is most

probably due to the large absorption cross section of Yb^{3+} and the phonon assisted resonance between $^2F_{7/2} \rightarrow {}^2F_{5/2}$ relaxation of Yb^{3+} and $^5I_8 \rightarrow {}^5I_6$ transition of Ho^{3+}, as is shown in the energy diagram on Figure 3.8. Most of the $^5I_6$ excited Ho^{3+} ions are promoted to $^5F_4 + {}^5S_2$ state by ET from the non-radiative relaxation of another excited Yb^{3+} ion, producing the bright green emission band after relaxation of Ho^{3+} ions to ground state ($^5F_4 + {}^5S_2 \rightarrow {}^5I_8$). The increment of up-converted signal with the decrement of Ho^{3+} concentration is the result of the elimination of Ho^{3+}agglomeration. Clustering by agglomeration is the tendency of active ions in a solid-state medium to form clusters rather than to be randomly spread. It allows energy migration between ions that can degrade or quench the fluorescence efficiency. These experimental results also suggest that the threshold for clustering interaction is 0.001 mol% of Ho^{3+} but depends on the kind of ion. In addition, the energy back transfer process ($^5F_4 + {}^5S_2$) (Ho^{3+}) + $^2F_{7/2}$ (Yb^{3+}) $\rightarrow {}^5I_6$ (Ho^{3+}) + $^2F_{5/2}$ (Yb^{3+}) was promoted for larger Yb^{3+} concentration (larger than 2 mol%). The presence of this phenomenon reduces the population on $^5F_4 + {}^5S_2$ and explains the fluorescence quenching of the green emission.

The low intensity of red and NIR emission suggest that transition associated have a very low probability. For example, a little part of the population on the $^5F_4 + {}^5S_2$ level decays to $^5I_7$ producing the NIR emission centered at 760 nm. Such transition is confirmed by its direct dependence with the population on $^5F_4 + {}^5S_2$ for both Ho^{3+} and Yb^{3+} concentration. Notice in Figure 3.4 that NIR emission follows the trend of the green emission. The red emission is associated to the transition $^5F_5 \rightarrow {}^5I_8$. Population on such energy level could be fed by non-radiative relaxation of $^5F_4 + {}^5S_2$. However, energy of about 6 phonons is required to match the energy gap (2,865 cm^{-1}). The most probably is that $^5F_5$ is fed by $^5I_7 \rightarrow {}^5F_5$ because of the ET from an Yb^{3+} ion. Population on $^5I_7$ is provided by $^5I_6$ with the help of the energy vibration of OH^- (3,450 cm^{-1}) whose energy matches the energy gap (3,476 cm^{-1}) between such levels. This proposed mechanism is consistent with the continuous increment of the red band for larger concentrations of Yb^{3+}, and the decrement of green and infrared emissions bands. The very week blue emission ($^5F_3 \rightarrow {}^5I_8$) corroborates the transition $^5I_5 \rightarrow {}^5F_3$. Although with very low

probability, this signal confirms the presence of a cascade phonon relaxation $^5F_5 \rightarrow {}^5I_4 \rightarrow {}^5I_5$, considering that is the only way to feed $^5I_5$.

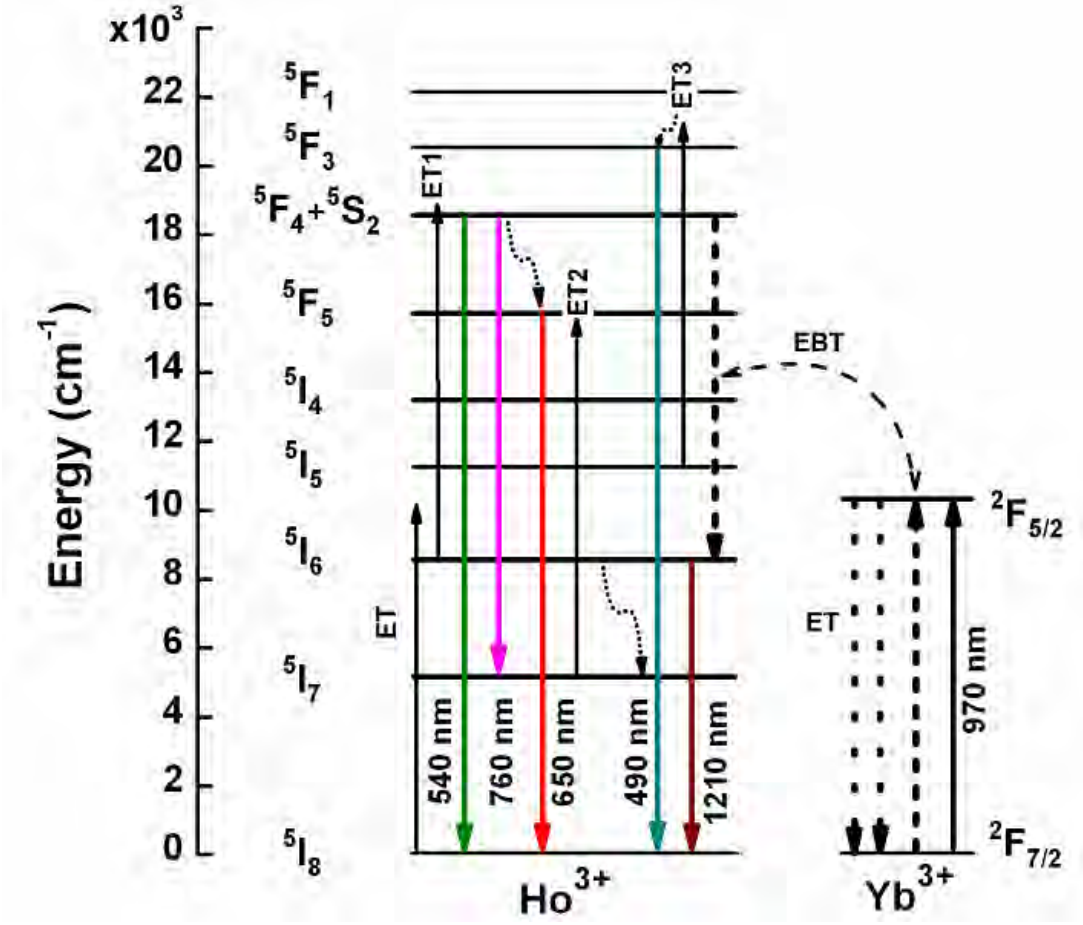

Figure 3.8: Energy level diagram showing the proposed mechanism for the up-conversion process.

3.4.2. LUMINESCENCE DECAY TIME

The luminescence decay times of Yb^{3+} - Ho^{3+} doped samples were obtained for typical samples and plots are shown in Figure 3.9. Decay time for signal centered at 540 nm can be fitted with a single exponential function for different concentration of Yb^{3+} and double exponential for different concentration of Ho^{3+}. The effective decay times were calculated according to the expression (2.12) and the obtained results are listed in Table 3.2. For constant concentration of Ho^{3+} (1 mol%) τ_{eff} is about 210 μs for 0.5, 1 and 5 mol% of Yb^{3+}, with a little increase for 2

mol% (τ_{eff} 220 μs) and a strong reduction for 10 mol% (τ_{eff} 168 μs). The apparent independence of τ_{eff} for the green band is in opposite of the behavior observed for visible emission on the system Yb^{3+}-Er^{3+} where a decrement was observed with the increment of Yb^{3+} concentration. These results suggest that dynamics of visible emission is dominated by migration $Ho^{3+} \leftrightarrow Ho^{3+}$ as a result of the formation of cluster or ion agglomeration. The little increment observed for τ_{eff} is probably the result of local clustering reduction with the increment of Yb^{3+}. However, the strong diminish for higher concentration of Yb^{3+} is probably the results of back transfer process as was discussed before. The existence of clusters is proposed by the increment of τ_{eff} with the reduction of Ho^{3+} concentration that in turn reduces cluster interaction, see Table 3.2. In this case, the largest decay time τ_{eff} was about 360 μs and was obtained for 0.001 mol% of Ho^{3+}, an indeed small concentration, suggesting the reduction of agglomeration.

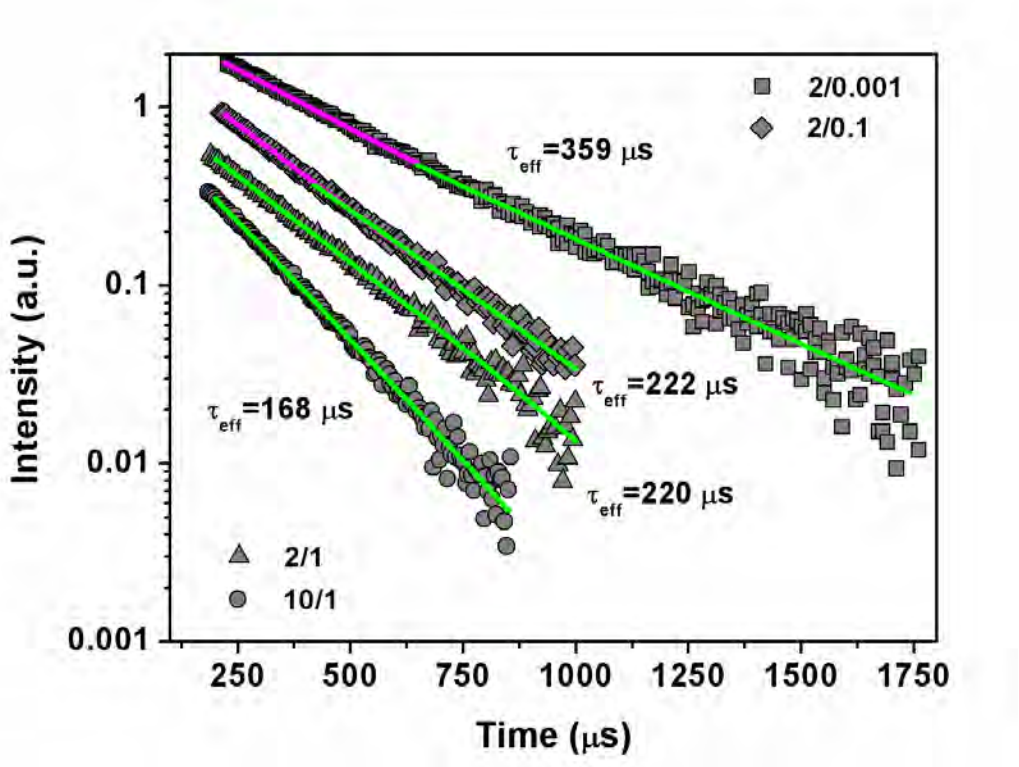

Figure 3.9: Fluorescence decay time of 540 nm emissions from the samples with different Yb^{3+}/Ho^{3+} concentration after excitation at 970 nm.

Notice the little deviation from single exponential of decay time plot for sample doped at 0.1 mol%, see Figure 3.9. Furthermore, fast decay time is the same as that of sample doped at 1 mol%. These results suggest that decay time observed for samples with constant Ho^{3+} (1 mol%) concentration is just the fast response. No slow component was observed as a result of the strong cluster formation. The slightly different value between fast and slow component observed for low concentration of Ho^{3+} could be the result of non-radiative relaxation to $^5F_5$ energy level due to phonon energy or back transfer induced by the relative high concentration of Yb^{3+} as was discussed before.

3.4.3. ENERGY TRANSFER EFFICIENCY

The highest luminescence decay time of Yb^{3+} characteristic emission centered at 1039 nm was about 840 μs, obtained for the lowest concentration of Ho^{3+}, from which start to reduce as concentration increases, though it diminishes faster if Yb^{3+} ion concentration increases. In both cases, such behavior is the result of the energy transfer from donor (Yb^{3+}) to acceptor (Ho^{3+}). The energy transfer efficiency was calculated by the expression (2.13) with RE = Ho, results are listed on Table 3.2. Samples with 1, 2 and 10 mol% of Yb^{3+}, no Ho^{3+} ion, were synthesized and their effective decay times were about 812, 883 and 259 μs, respectively. With these results the energy transfer efficiency η was calculated obtaining the largest one, in about 42%, for 2/2mol% (Yb/Ho) and diminishes by increasing Yb^{3+} concentration being only about 0.7% for 10 mol%.

These values suggest a mayor presence of migration $Yb^{3+} \leftrightarrow Yb^{3+}$ processes as a result of the larger ion concentration. Reduction of Ho^{3+} concentration reduces drastically the energy transfer efficiency being the lowest one, in about 5%, for 0.001 mol% of Ho^{3+}. Such reduction on energy transfer was expected considering the very low concentration of acceptors. One should be aware of the possibility that the presence of the acceptor could affects the donor luminescence by a mechanism other than ET (for example back transfer), and hence diminishes decay times from the quenched samples, resulting in larger ET efficiencies than the true values, due to the form of the equation 2.13. This result suggests that 2 mol% of Yb^{3+} could be a high concentration and probably can be reduced. However, it is necessary keep in

mind that the excess of donors can guarantee the energy transfer process. This set of values listed on Table 3.2 is grossly in agreement with previous report [17], but the overall results reported here indicate an improvement of the UC process by both factors, synthesis process and ion concentration.

Table 3.2: Effective decay times and energy transfer efficiency of $ZrO_2:Yb^{3+}$ - Ho^{3+} nanocrystals.

Sample concentration (mol%)		**Effective decay time (μs)**		**η_{ET} (%)**
Yb	**Ho**	**539 nm**	**1039 nm**	
0.5	1	206	667	--
1	1	213	669	17.6
2	1	220	694	21.4
5	1	211	606	--
10	1	168	257	0.77
2	0.001	359	841	4.75
2	0.01	284	820	7.13
2	0.1	222	805	8.83
2	1	220	694	21.40
2	2	198	509	42.35

3.4. REFERENCES

[1] A.C. Yanes, J.J. Velázquez, J. Del-Castillo, J. Méndez-Ramos, V.D. Rodríguez, "Colour tuneability and white light generation in Yb^{3+}–Ho^{3+}–Tm^{3+} co-doped SiO_2–LaF_3 nano-glass-ceramics prepared by sol–gel method", Journal of Sol-Gel Science and Technology **51**(1),4-9 (2009)

[2] E. De la Rosa, P. Salas, H. Desirena, C. Angeles and R.A. Rodriguez, "Strong green upconversion emission in ZrO_2 : Yb^{3+}-Ho^{3+} nanocrystals", Appl. Phys. Lett. **87**(24), 1912 (2005)

[3] A. Wnuk, M. Kaczkan, Z. Frukacz, I. Pracka, G. Chadeyron, M.F. Joubert, and M. Malinowski, in 5th International Conference on Excited States of Transition Elements, Elsevier Science Sa, Ladek Zdroj, Poland, p.353 (2001)

[4] T. Kishimoto, N. Wada, and K. Kojima, "Upconversion fluorescence in Ho^{3+} doped $ZnCl_2$ glass", Phys. Chem. Glasses **43**, 233 (2002)

[5] J. Silver, E. Barrett, P.J. Marsh, and R. Withnall, "Upconversion luminescent emission from holmium-doped yttrium oxide under 632.8 nm light excitation", J. Phys. Chem. B **107**, 9236 (2003)

[6] W. Ryba-Romanowski, S. Golab, G. Dominiak-Dzik, P. Solarz, and T. Lukasiewicz, "Conversion of infrared radiation into red emission in YVO_4:Yb,Ho," Applied Physics Letters **79**, 3026-3028 (2001)

[7] E. Osiac, S. Kuck, I. Sokolska, M. Osiac, and G. Huber, "Upconversion avalanche processes in Ho^{3+}-Yb^{3+}:YLF crystal", Rom. Rep. Phys. **60**, 937 (2008)

[8] X.F. Wang, S.G. Xiao, Y.Y. Bu, X.L. Yang, and J.W. Ding, "Visible photon-avalanche upconversion in Ho^{3+} singly doped beta-$Na(Y_{1.5}Na_{0.5})F_6$ under 980 nm excitation", Opt. Lett. **33**, 2653 (2008)

[9] J.C. Boyer, F. Vetrone, J.A. Capobianco, A. Speghini, and M. Bettinelli, "Yb^{3+} ion as a sensitizer for the upconversion luminescence in nanocrystalline $Gd_3Ga_5O_{12}$:Ho^{3+}," Chemical Physics Letters **390**, 403-407 (2004)

[10] A. Patra, P. Ghosh, P.S. Chowdhury, M. Alencar, B.W. Lozano, N. Rakov and G.S. Maciel, "Red to blue tunable upconversion in Tm^{3+}-doped ZrO_2 nanocrystals", J. Phys, Chem. B **109** 10142 (2005)

[11] T. Lopez-Luke, E. De la Rosa, P. Salas, C. Angeles-Chavez, L.A. Diaz-Torres and S. Bribiesca, "Enhancing the up-conversion emission of ZrO_2 : Er^{3+} nanocrystals prepared by a micelle process", J. Phys. Chem. C **111**, 17110 (2007)

[12] D. Solís, T. López-Luke, E. De la Rosa, P. Salas and C. Angeles-Chavez, "Surfactant effect on the upconversion emission and decay time of ZrO_2:Yb-Er nanocrystals", *J. Lumin.* **129**, 449 (2009)

[13] E. De la Rosa, D. Solis, L.A. Diaz-Torres, P. Salas, C. Angeles-Chavez and O. Meza, "Blue-green upconversion emission in ZrO_2:Yb^{3+} nanocrystals", J. Appl. Phys. **104**(10), 3508 (2008)

[14] E. De la Rosa-Cruz, L.A. Diaz-Torres, R.A. Rodriguez-Rojas, M.A. Meneses-Nava, O. Barbosa-Garcia and S. Salas, "Luminescence and visible upconversion in nanocrystalline ZrO_2 : Er^{3+}", Appl. Phys. Lett. **83**, 4903 (2003)

[15] G. Xu, X. Zhang, W. He, H. Liu, and H. Li, "The study of surfactant application on synthesis of YAG nano-sized powders", Powder Technology **163**, 202 (2006)

[16] F. Vetrone, J.C. Boyer, J.A. Capobianco, A. Speghini, and M. Bettinelli, "NIR to visible upconversion in nanocrystalline and bulk Lu2O3 : Er 3+," Journal of Physical Chemistry B 106, 5622–5628 (2002)

[17] H. Desirena, E. De la Rosa, A. Shulzgen, S. Shabet and N. Peyghambarian, "Er^{3+} and Yb^{3+} concentration effect in the spectroscopic properties and energy transfer in Yb^{3+}/Er^{3+} codoped tellurite glasses", J. Phys. D: Appl. Phys. **41**(09), 5102 (2008)

CHAPTER 4

LUMINESCENCE PROPERTIES OF

$ZrO_2:Yb^{3+}$, Tm^{3+} NANOCRYSTALS

4.1. INTRODUCTION

Among the oxide hosts, the zirconia matrix seems to be an ideal medium for preparation of highly luminescent materials because it is chemically and photochemically stable, has a high refractive index and low phonon energy [1]. Previously, we have described the influences of dopant concentration, crystallite size and crystal structure on the emission properties of erbium and holmium ions in oxide nanocrystals, as well as the influence of ytterbium over the emission. Here in this chapter, thulium ion is considered. Studies of the up-conversion process in thulium (Tm^{3+}) doped materials are of great interest because Tm^{3+} exhibits strong luminescence in the violet and blue region [2]. The main goal of this analysis is to study the up-conversion luminescence of Tm^{3+}:Yb^{3+} co-doped ZrO_2 matrix and how this property changes with changing co-dopant concentration. This report includes the investigations of how the preparation of nanoparticles and concentration of both ions affects the up-conversion emission properties of Yb^{3+} - Tm^{3+} co-doped ZrO_2 nanocrystals.

On this occasion, the annealing temperature was lowered to 800^{o}C in order to observe structural and luminescent effects by changes in size. In addition, a set of samples were prepared by sol-gel with surfactant added. This variant is similar to micelle method except that the hydrothermal treatment was omitted as to observe its possible effect on luminescence optimization. Samples were prepared by a micelle method using CTAB as surfactant. The study of this surfactant in this section has the purpose of comparing it with Pluronic F-127 used before, and decides which one is more effective in eliminating remnants resulted from the synthesis process, especially the OH, as these affect the optical properties. It is expected a difference between Pluronic F-127 and CTAB due to their dissimilar characteristics.

4.2. EXPERIMENTAL PROCEDURE

The synthesis of Yb^{3+}-Tm^{3+} doped ZrO_2 nanophosphors were prepared by a micelle method, with thulium chloride ($TmCl_3 \cdot 6H_2O$) and cetyl trimethyl ammonium bromide (CTAB) added as cationic surfactant at molar ratio concentration Mr = CTAB/ZrO_2 = 0.2. CTAB were also added

into another set of samples prepared by sol-gel process. All samples were annealed at 800^{o}C and kept there for 2h. Test samples were synthesized applying three annealing times (0, 2 and 5 h), for samples with and without surfactant. Both processes are described on section 2.2. In previous work reported by our group, it has been optimized the percentage of CTAB in ZrO_2 nanocrystals as to obtain the maximum emission efficiency of Er^{3+} [3].

The set-up for the X-ray diffraction (XRD) and photoluminescence (PL) characterization is the same as described on section 2.2 for ZrO_2:Yb^{3+}–Er^{3+} samples. Transmission electron microscopy (TEM) was carried out in same way as described on section 3.2 for ZrO_2:Yb^{3+}-Ho^{3+}.

4.3. STRUCTURAL PROPERTIES

The XRD patterns for the ZrO_2:Yb^{3+}-Tm^{3+} nanocrystals are shown in Figure 4.1. The crystalline phase composition of samples annealed for 2 and 5 hours at 800°C are considerably tetragonal and slightly cubic for samples prepared with and without hydrothermal treatment tagged as M and S, respectively. Table 4.1 lists the phase composition for each process and annealing times by using semi-quantitative phase analysis software. All samples annealed at 800^{o}C show tetragonal phase as dominant (*a* through *d*) for both with and without hydrothermal treatment, and for 1000^{o}C tetragonal phase forms 100% of the composition (*e*). Tetragonal phase is notably increased for 5h annealing time than that for 2h; however a major composition of tetragonal phase is presented without hydrothermal treatment, suggesting that its presence favors cubic phase. In addition, the results of the XRD patterns confirm the influence that Yb^{3+} concentration has on the stabilization of the tetragonal phase. As was previously reported, if ytterbium is absent in the system then the corresponding structure contains mainly the monoclinic phase [4]. So that, the effect of ytterbium concentration on the zirconia structure is to stabilize the tetragonal and cubic metastable phases avoiding the formation of the monoclinic. For low dopant concentrations, the tetragonal crystalline structure is most affected by the annealing time and temperature, since this phase increases when both parameters are incremented [3].

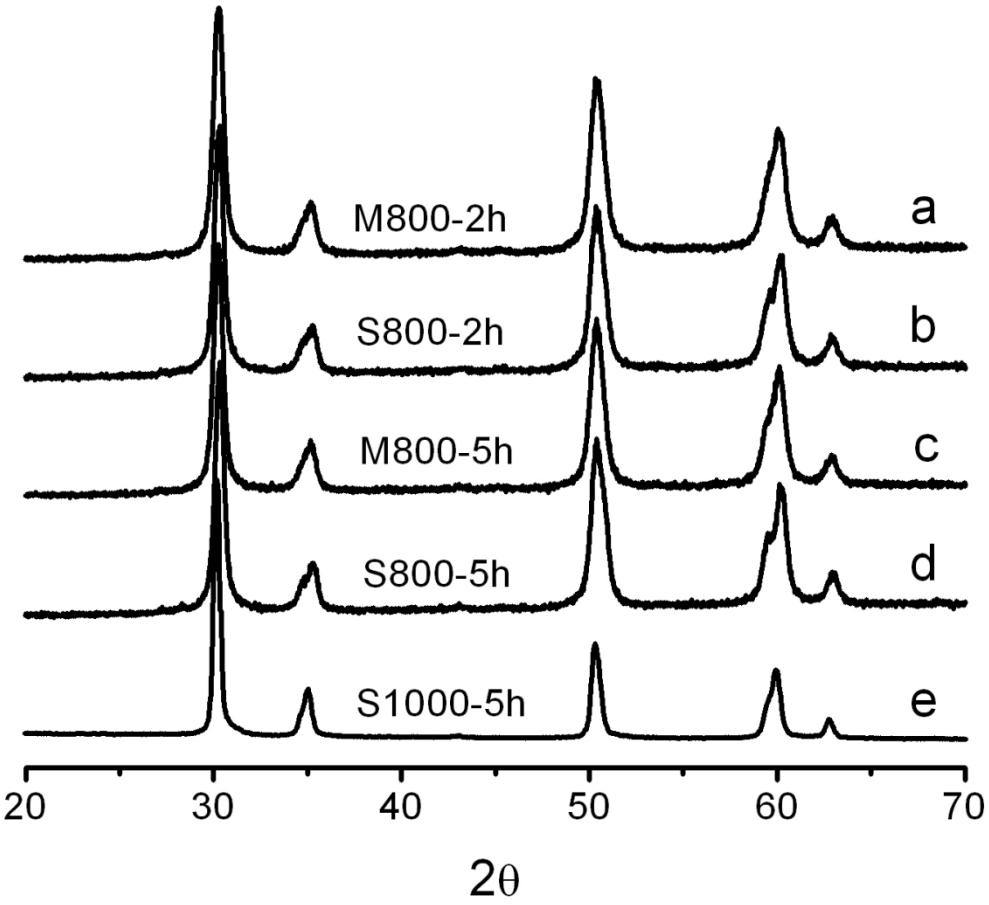

Figure 4.1: Figure 1: XRD patterns for (Yb^{3+}/Tm^{3+}) 2/0.5 mol% test samples with annealing times of 2h (a,b) and 5h (c-e), at 800^{o}C (a-d) and 1000^{o}C (e). Micelle and sol-gel methods are tagged as M and S respectively.

It is seems that tetragonal phase increases with increase the temperature and concentration of Yb^{3+} ions. The effect of increasing the tetragonal phase is due to removal of oxygen vacancies, which helps to reduce the nonradiative relaxation. It is well known that the stabilization of the fluorite-type zirconia lattice can be achieved by oxygen vacancies mechanism for trivalent dopants [5]. These results clearly indicate the crystal structure and crystal symmetry are depending on the annealing temperature and concentration of dopant ions. Therefore, with increasing the temperature of annealing the crystal size increases due to growth of particles. This dependence indicates the important role on the Yb^{3+} dopant content as a control for the crystal phase and crystal size. Results show how the crystal phase and crystal size can be controlled by changing the Yb^{3+} concentration and annealing temperature.

An increase in pattern broadness relating to annealing temperature (800^{o}C) can be appreciated on the XRD patterns *a-d* in Figure 4.1, implying a notable decrease in crystallite size compared with that of 1000^{o}C, indicated on pattern *e*. Strain on the lattice also contributes to the broadening, but crystal size is a more critical factor, that effect was described on previous chapter when Ho^{3+} was analyzed. The diameter of rare-earth ion (M^{3+}) is larger than that of Zr^{4+}, and hence such ion will induce the change of ZrO_2 lattice.

Table 4.1: Phase composition and crystallite size of 2/0.5 mol% ZrO_2:Yb^{3+} - Tm^{3+} nanocrystals.

Temperature (^{o}C)	Annealing time (h)	Method (M=micelle) (S=sol-gel)	Phase composition (wt.%)		Cristallite size (nm)
			Ct	Cc	
800	2	M	53.6	46.4	12.1018
800	2	S	75.2	24.8	14.1899
800	5	M	82.2	17.8	12.1026
800	5	S	88.9	11.1	14.1909
1000	5	S	100	-	21.6522

The crystallite size was calculated using Sherrer's equation 3.1, as used in chapter 3. The average crystallite size is 12.1 nm for samples synthesized by micelle method, and 14.1 nm by sol-gel. For the S1000-5h sample the average crystallite size increased to 21 nm. These values seem to indicate that average crystallite size does not present a significant dependency with annealing time increment, but it exists for annealing temperature. The dispersion capability of the surfactant CTAB can be observed in the TEM images shown in Figure 4.2. Particle size distribution can be obtained by TEM observation of Yb^{3+} - Tm^{3+} co-doped ZrO_2 nanocrystals prepared at 800^{o}C. The particles are in aggregated form and the average diameter is about 26 nm. Synthesis with optimum concentration of CTAB under 1000^{o}C annealing temperature usually keeps the nanocrystals well dispersed for a low annealing time [6]; though, in this

case, when the annealing temperature was reduced as to diminish crystallite size, agglomeration resulted unavoidable.

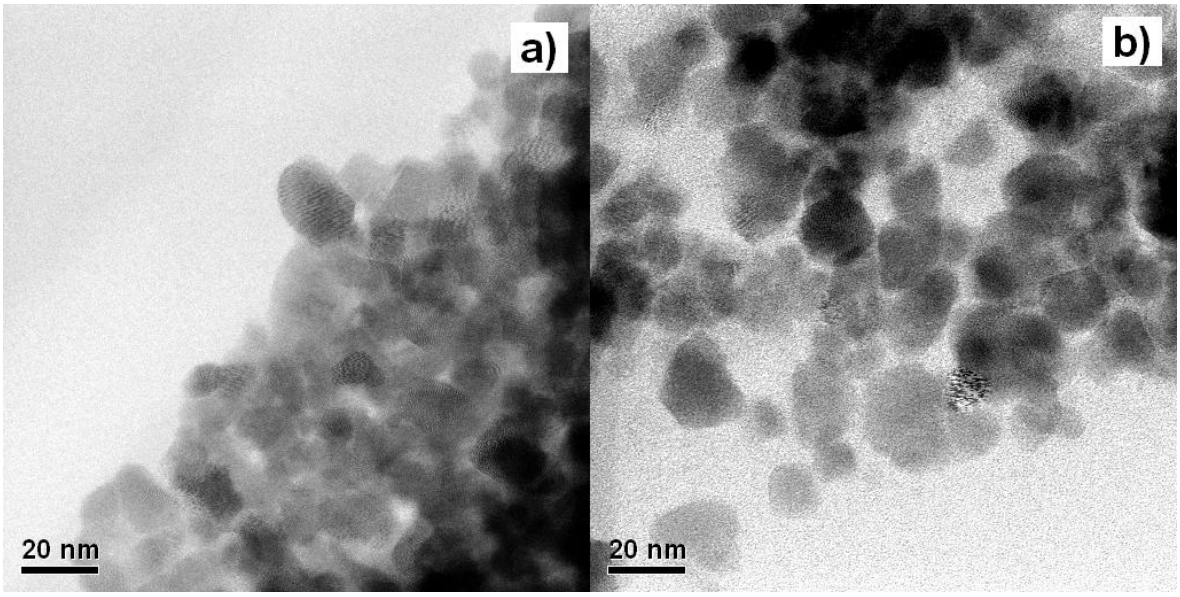

Figure 4.2: TEM images of ZrO_2:Yb^{3+} - Tm^{3+} nanocrystals for 2/0.5 mol% of Yb^{3+}/Tm^{3+} by micelle (a) and sol-gel (b) methods.

For relative low annealing temperature CTAB does not exhibit effect to the dispersion enhancement of powders, therefore the fact that surfactant helps to obtain better crystalline structure and better dispersed nanocrystallites, as considered previously with Pluronic F-127 [7,8], could not be concluded at least for 800^{o}C annealing temperature.

4.4. LUMINESCENCE PROPERTIES

The emission spectra of codoped ZrO_2:Yb^{3+} - Tm^{3+} nanophosphors, shown in Figures 4.3 and 4.4, exhibits four distinct emission bands associated to different transition of Tm^{3+} resulting from the up-conversion process. One weak emission on the UV side of the spectra peaked at 368 nm associated to the $^1D_2 \rightarrow {}^3H_6$ transition. One red band centered on 660 nm and attributed to the $^3F_2 \rightarrow {}^3H_6$ transition. And two dominant bands, the near infrared and the blue bands centered at 800 and 470 nm attributed to the $^3H_4 \rightarrow {}^3H_6$ and $^1G_4 \rightarrow {}^3H_6$ relaxations of Tm^{3+}, respectively. Figure 4.3 shows the up-converted signal obtained for different Yb^{3+} and

constant Tm^{3+} concentration. An increment of the emitted signal can be observed with the increment of Yb^{3+} concentration (for concentration lower than 4 mol%), but all emission bands increase equally. Notice the little change on the ratio of two central peaks from blue band, peak centered at 475 nm increases while the one centered at 487 nm decreases. However, the overall effect is a quenching of the blue band for a concentration higher than 2 mol%. Furthermore, in addition of the characteristic peaks of the blue band (452, 463, 473 and 486 nm due the stark splitting of the $^1G_4 \rightarrow {}^3H_6$ transition) the peak centered at 501 nm cannot be associated to any transition of Tm^{3+}. We assume such peak is ascribed to the cooperative emission from an Yb^{3+} - Yb^{3+} pair interaction. That will be discussed on a later section.

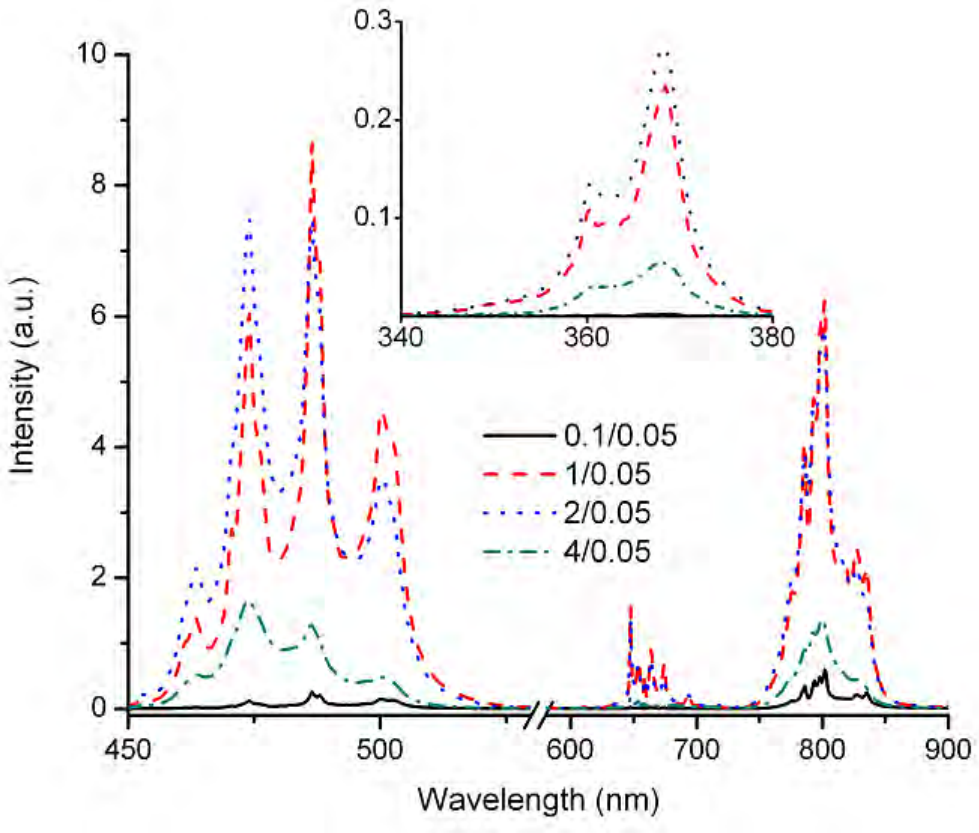

Figure 4.3: Emission spectra of the ZrO_2:Yb^{3+} - Tm^{3+} nanophosphors for different concentrations of Yb^{3+} with 0.05 mol% of Tm^{3+}.

Figure 4.4 shows the up-converted signal for samples prepared with different concentration of Tm^{3+} and constant 2 mol% of Yb^{3+}, where maximum blue emission was obtained. All bands

show a strong dependence on the concentration of Tm^{3+}. In such a figure, the emissions were scaled by a factor of 5x and 15x for 0.5 and 1.5 mol% of Tm^{3+}, respectively. Interestingly, when the concentration of Tm^{3+} is increased the intensity of blue band decreases while the infrared band increases. However, the overall effect is a quenching of the signal emitted.

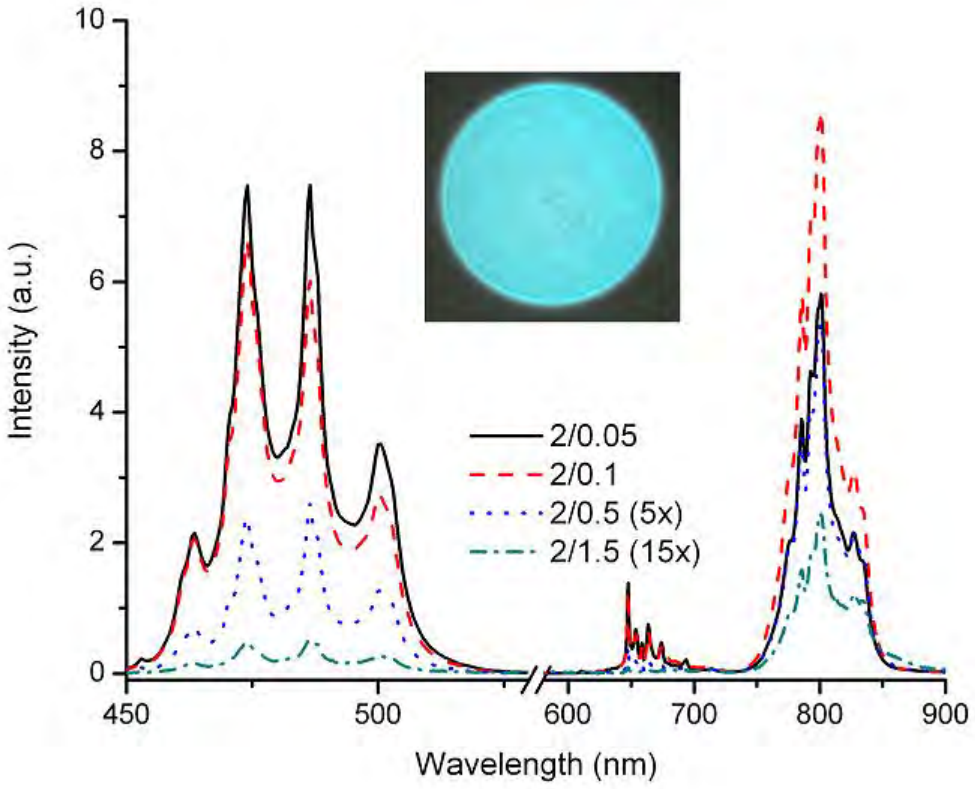

Figure 4.4: Emission spectra of the ZrO_2:Yb^{3+} - Tm^{3+} nanophosphors for different concentrations of Tm^{3+} with 2 mol% of Yb^{3+}.

The up-converted spectra for each sample was integrated and normalized to the brightest sample, allowing analysis of luminescent intensity in relation to ion concentration (depicted in Figures 4.5 and 4.6). The highest overall emission was achieved with a concentration of 2 mol% of Yb^{3+} and only 0.1 mol% of Tm^{3+}, although in this case the infrared band is dominant, as is shown in Figure 4.5. The strongest blue emission band contains about 34% of the total emitted signal and was obtained with 2 mol% of Yb^{3+} and 0.05 mol% of Tm^{3+}. However, in this case the overall signal emitted is only 80% of the highest one. Similar optimization can be

observed for 2/0.1 and 1/0.05 mol% samples resulting blue emissions of about 29 and 30% of the overall highest emitted signal, respectively, as is shown in Figure 4.5.

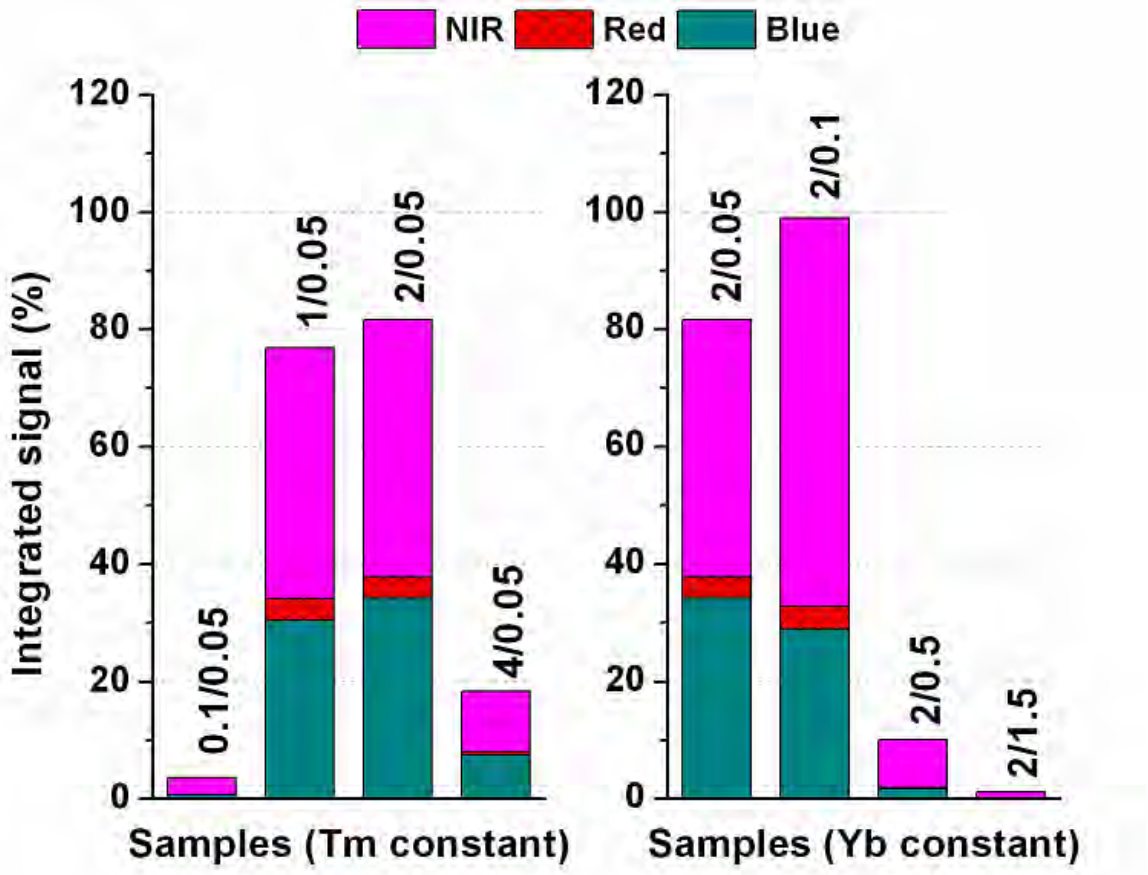

Figure 4.5: Normalized integrated signal by sample of ZrO_2:Yb^{3+} - Tm^{3+} nanophosphors with different concentration of Yb^{3+} and Tm^{3+}.

Figure 4.6 depicts only the normalized blue up-converted intensity as a function of Yb^{3+} concentration (with 0.05 mol% of Tm^{3+}), and as a function of Tm^{3+} concentration (with 2 mol% of Yb^{3+}). The increment on the emitted signal for 2/0.05 sample can be attributed to the reduction of Tm^{3+} inter-ionic interactions due to the agglomeration formation. These results highlight the considerable influence of Tm^{3+} on the UC signal and the low threshold for the agglomeration formation. Although both graphs show a remarkably different trend for ion concentrations, they both have a quadratic fit which suggests that energy transfer up-conversion (ETU) is the dominant cooperative transition, since it varies quadratically with ion

concentration [9]. In this process, two ions in close proximity are excited to an intermediate level. They are coupled by a non-radiating process in which one relaxes to a lower state, while the other is excited to an upper state. This behavior is comparable to the Ho^{3+} case described on previous chapter.

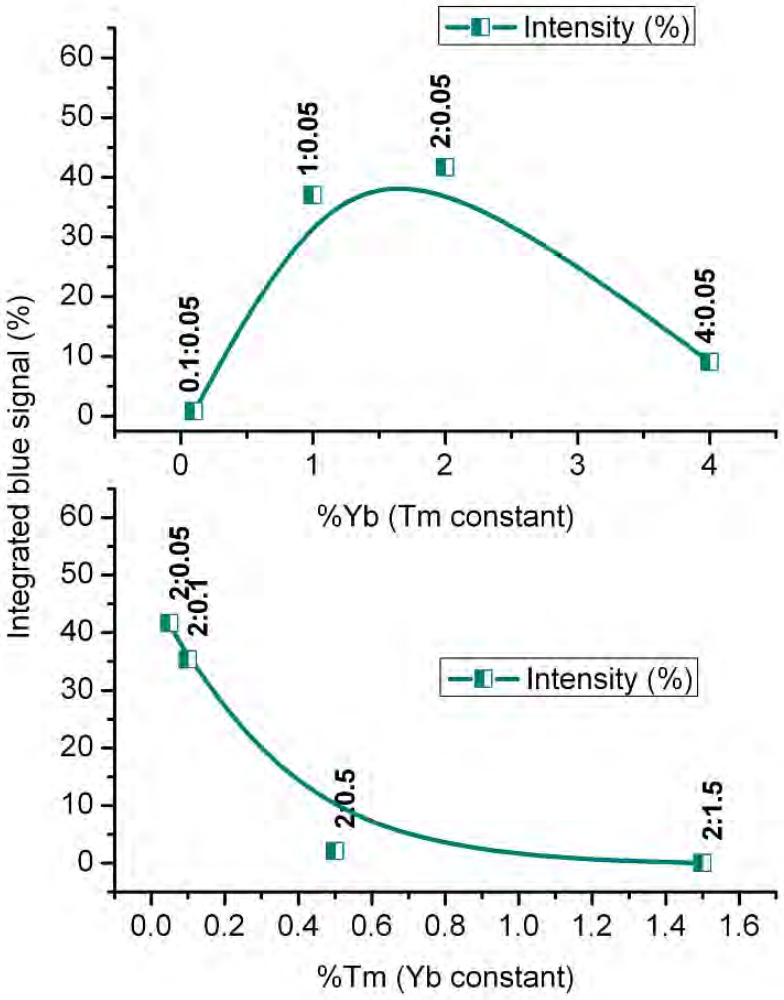

Figure 4.6: Integrated blue up-converted signal as a function of Yb^{3+} concentration (with 0.05 mol% of Tm^{3+}) and Tm^{3+} concentration (with 2 mol% of Yb^{3+}).

Figure 4.7 shows the NIR spectra of Yb^{3+} emission centered at 1039 nm. For the set of samples with constant Tm^{3+} concentration (0.05 mol%) the emission band changes from 0.1 to 1 mol%, been more significant for 2 and 4 mol% concentration of Yb^{3+}. It is suitable to ascribe this notable change in the emission pattern to a crystal lattice modification. In other words,

there is a different crystalline phase composition for each Yb^{3+} ion concentration used for co-doping. Additional evidence of the Yb^{3+} - Tm^{3+} energy transfer could be observed by analyzing the intensity change of the standard Yb^{3+} emission. Considering the second group (with constant 2 mol% Yb^{3+}) a notable intensity reduction could be appreciated in the signal emitted for 0.5 and 1.5 mol% of Tm^{3+}, see figure 4.7. With a minute increment from 0.1 to 0.5 mol% the overall intensity signal were reduced about 85%. The clear decrease in Yb^{3+} emitted signal observed with the increment of Tm^{3+} suggests the presence of an ET process.

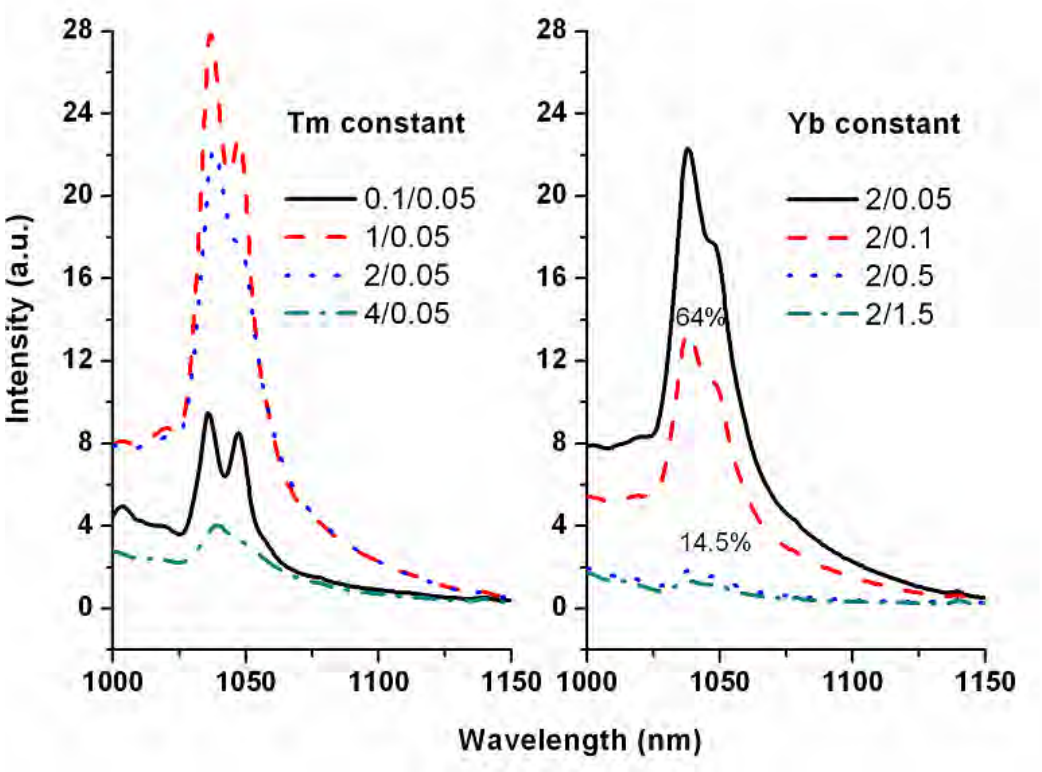

Figure 4.7: Characteristic emission for Yb^{3+} ion peaked at 1039 nm.

4.4.1. UP-CONVERSION EMISSION MECHANISM

The proposed mechanism associated to the up-conversion emission of Tm^{3+} is described on the energy level diagram shown in Figure 4.8. Tm^{3+} ion (acceptor) is excited by the energy transfer (ET) from the $^2F_{7/2} \rightarrow {}^2F_{5/2}$ transition of Yb^{3+} (donor) that is excited directly by the pumping signal. Phonon assisted resonance between $^2F_{5/2} \rightarrow {}^2F_{7/2}$ relaxation of Yb^{3+} and $^3H_6 \rightarrow {}^3H_5$ transition of Tm^{3+}permits the first excited level, from which ions are then relaxed non

radiatively to $^3F_4$, forming a reservoir level. The energy gap between levels $^3H_5$ and $^3F_4$ is ~2200 cm^{-1}, which can be resonant with some stretching bands associated with different residual components such as one phonon of CO_2 (2350 cm^{-1}) and two of OH (from the 1200 – 1400 cm^{-1} band) or CH=CH (1050 cm^{-1}); those are more feasible than the ~5 phonons required from the host. Part of $^3F_4$ ions decay to ground state producing emission at 1650 nm ($^3F_4 \rightarrow {}^3H_6$), as is shown in the energy diagram on Figure 4.8.

Tm^{3+} ions from $^3F_4$ excited level are partly promoted to $^3F_2$ state by ET from the non-radiative relaxation of another excited Yb^{3+} ion, from which undergoes the $^3F_2 \rightarrow {}^3H_6$ transition that produces the weak 660 nm emission band. Through unstability of $^3F_2$ level, its population rapidly decays to $^3H_4$ non radiatively producing the infrared emission band ($^3H_4 \rightarrow {}^3H_6$), peaked at 800 nm. Population on the metastable $^3H_4$ level from Tm^{3+} is promoted to $^1G_4$ by ET from another excited Yb^{3+} ion, from which a radiative relaxation occurs, related to the blue emission peaked at 470 nm resulting from $^1G_4 \rightarrow {}^3H_6$ transition of Tm^{3+}. There is a weak UV emission band peaked at 368 nm ascribed to $^1D_2 \rightarrow {}^3H_6$ transition of Tm^{3+} that is highly dependent from $^1G_4$ population, from which is promoted by ET from another excited Yb^{3+} ion, and thereby is directly related with Yb^{3+} concentration due to several successive ET processes required to excite this level.

Under these conditions, a cross-relaxation between Tm^{3+} ions themselves along the channel ($^3H_4 + {}^3H_6$) → ($^3F_4 + {}^3F_4$) is possible. Cross-relaxation forms an efficient feedback mechanism that connects the emitting level $^3H_4$, the reservoir level $^3F_4$ and the ground level, thus enhancing efficiently the population in the reservoir level. This cross-relaxation channel populates the $^3F_4$ level and favors the population of the $^3H_4$ level, and possibly makes additional contribution to the 660 nm band. As for $^3F_4$ level such feeding mechanism explains the relative incremented luminescence band in the 470 nm range corresponding to the $^1G_4 \rightarrow {}^3H_6$ transition in the Tm^{3+} ion (see Figure 4.4) with the decrement of Tm^{3+} concentration to 0.05 mol%. Considering this scenario, a complementary blue up-converted signal is possible

with the increment of Yb^{3+} concentration, which they transfers energy to more Tm^{3+} ions that undergoes this cross-relaxation process, before emission quenching occurs.

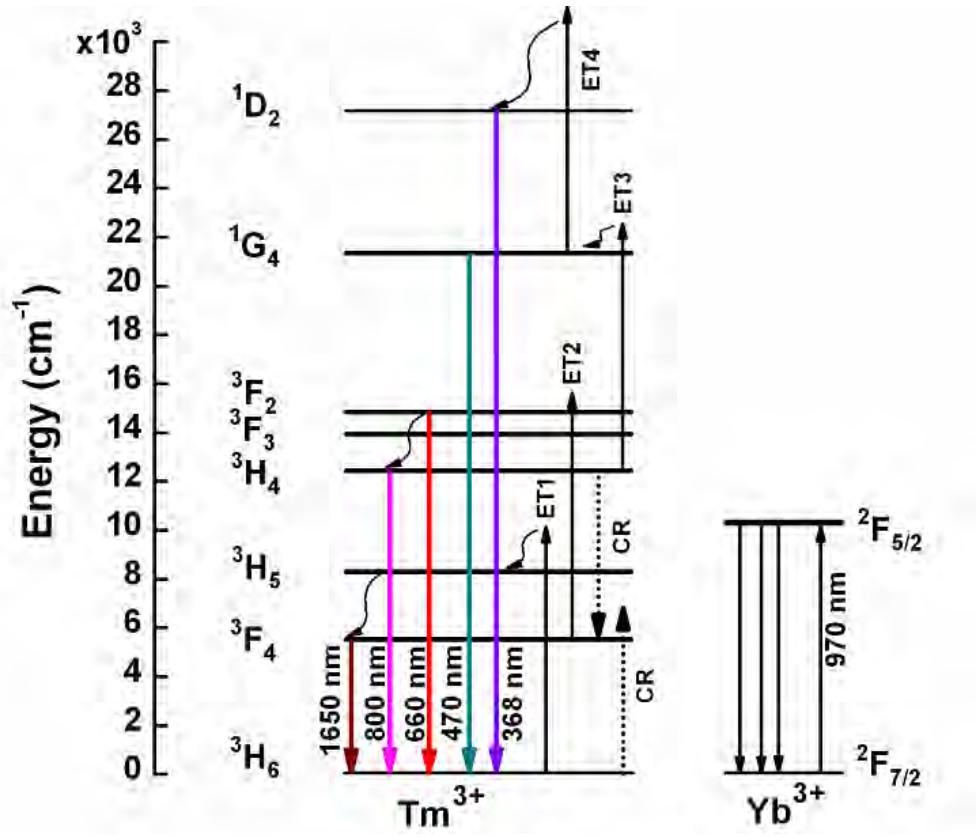

Figure 4.8: Energy level diagram showing the proposed mechanism for the up-conversion process.

In order to analyze the UC mechanism which populates the $^1G_4$ level, the pump power dependence of the emission from $^1G_4 \rightarrow {}^3H_6$ level at 470 nm was investigated on excitation intensity at 970 nm according to equation 3.1 and the results are shown in Figure 4.9. The experimental data (inverted triangles) have been fitted with a straight line with slope of 2.5≈3 which indicates a three photon process related to blue UC emission from Tm^{3+}. Similar situation occurs for 660 nm band (circles), with a slope of 2.2, that hint suggest that it proceeds from $^3F_2$ level after two-photon absorption process. Both emissions are stimulated by the cross-relaxation that is taking place in the system which propitiates more population in $^3F_2$ and $^1G_4$ levels.

The 800 nm band (squares) exhibits a slope of 1.5≈2 that is in agreement with two-photon absorption process as well. Moreover, this band undergoes a lack of contribution from $^3H_4$ by the suggested cross-relaxation process. For UV band peaked at 368 nm data (rhombuses) manifests a slope of 3.3≈4 which is related to a four-photon absorption process. This emission band is completely dependent of the $^1G_4$ level which is populated by an energy transfer (ET3) from $^3H_4$, thus the last energy transfer required (ET4) to feed $^1D_2$ should be highly phonon-coupled resulting in a deficient approximation to expected value. Finally, the pump power dependence of the emission at 501 nm was investigated and the result is also shown in Figure 4.9 (triangles). The experimental data has been fit with a straight line with slope of 2.1, which reveals that this emission line is a two-photon (or pair) absorption process which indicates this is a cooperative emission.

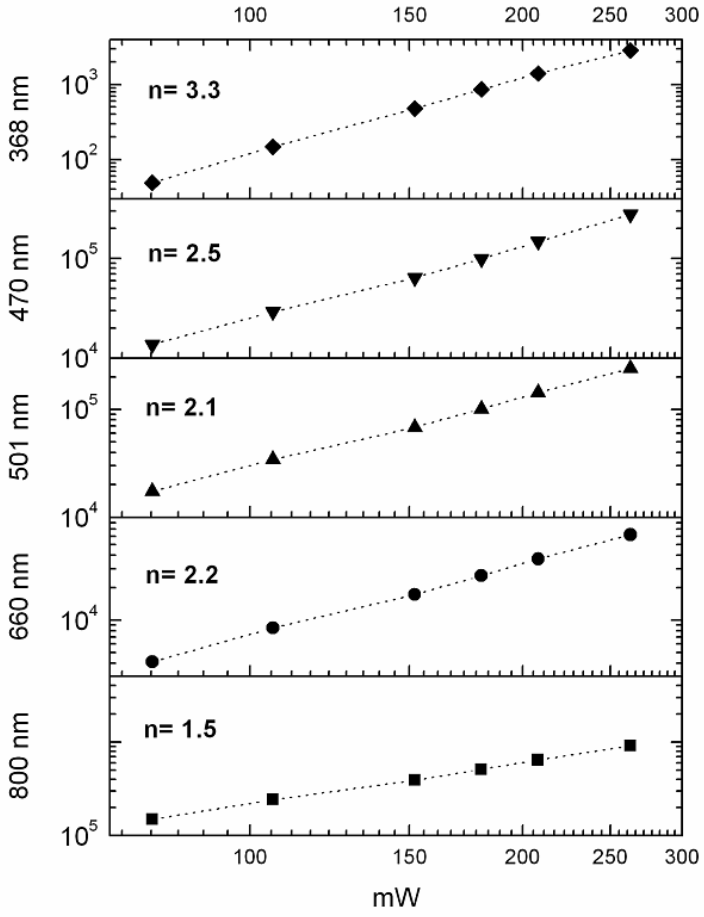

Figure 4.9: Dependence of the up-converted signal intensity with pumping power excitation for different emissions bands of Tm^{3+} for 2/0.05 sample.

4.4.2. LUMINESCENCE DECAY TIME

The effective decay times of Yb^{3+} - Tm^{3+} doped samples were calculated according to the expression (2.12) and the obtained results were plotted and shown in Figure 4.10.

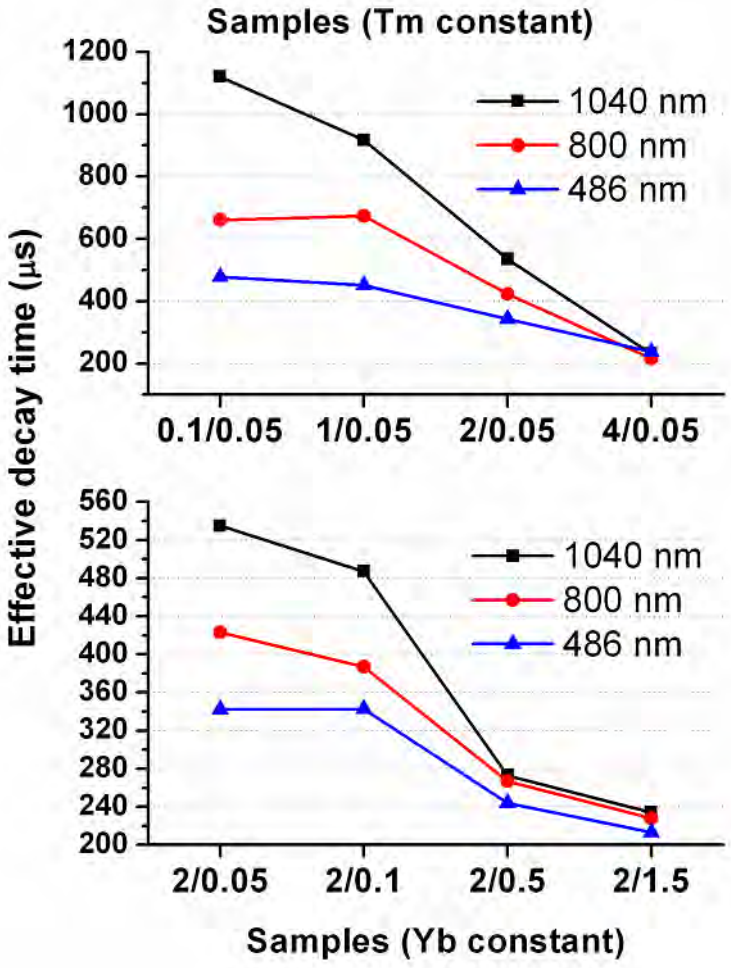

Figure 4.10: Effective decay time values for 486, 800 and 1040 nm emissions from samples with different Yb^{3+}/Tm^{3+} content after excitation at 970 nm.

For constant concentration of Tm^{3+} τ_{eff} at 486 nm are 478, 451, and 342 μs for 0.1, 1, and 2 mol% of Yb^{3+}, with the longer increase for 0.1 mol% and a moderate reduction for 4 mol% (τ_{eff} 248 μs). This dependence of τ_{eff} for the blue band is in agreement with the behavior observed for visible emission on the system Yb^{3+}-Er^{3+} where a decrement was observed with the

increment of Yb^{3+} concentration, as was reported recently [10]. The continuous decrease of decay time suggests the presence of luminescent quenching via energy migration Yb^{3+} - Yb^{3+} produced by the cluster or agglomeration formation of Yb^{3+} ion due to the increment of concentration. For constant concentration of Yb^{3+} τ_{eff} at 486 nm are 342 and 343 μs for 0.05, and 0.1 mol% of Tm^{3+}, with a high reduction for 0.5 and 1.5 mol% (τ_{eff} 244 and 213 μs). This reduction also suggests the presence of agglomeration of Tm^{3+} and then quenching of the luminescence via cross-relaxation and Tm^{3+} - Tm^{3+} migration. Thus, the existence of clusters was confirmed by the following aspects, the increment of τ_{eff} with the reduction of Yb^{3+} (agglomeration of Yb^{3+} ions) and the fast decrement of τ_{eff} with the low increment of Tm^{3+} concentration (see Figure 4.10).

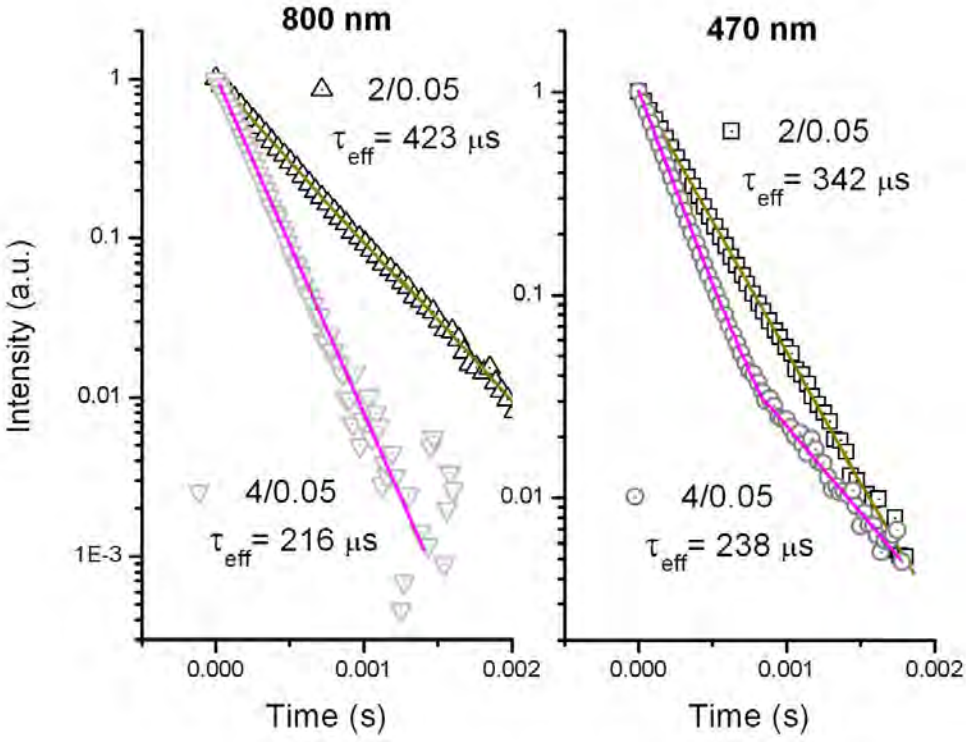

Figure 4.11: Decay kinetics for 486 and 800 nm emissions from optimized (2/0.05) and quenched (4/0.05) samples after excitation at 970 nm.

These results suggest that dynamics of visible blue emission is dominated by cross-relaxation and migration $Tm^{3+} \leftrightarrow Tm^{3+}$ as a result of the cluster formation. The τ_{eff} at 486 nm are

relatively long considering that are associated mainly by a three-photon absorption process, and become similar to those from 800 and 1040 nm on latter part of scheme from Figure 4.10 due to quenching of the luminescence. For constant concentration of Tm^{3+}, the τ_{eff} at 800 nm emission exhibits similar behavior as 486 nm band, though there is a little longer decay for 1/0.05 sample than that of 0.1/0.05 (661 and 674 μs respectively). The little increment observed for τ_{eff} is probably resulting of clustering reduction of Tm^{3+} ion with the decrement of Yb^{3+}.

The lengthened τ_{eff} at 486 nm from the $^1G_4$ level upon IR excitation is associated with the additional contribution by the cross-relaxation mechanism of excitation leading to the population of this level via the intermediate long-lived level $^3F_4$. We infer that a cross-relaxation (CR) foments the fact that at the long-lived intermediate level $^3F_4$ of the Tm^{3+} ion the quenching action is not manifest at higher intermediate levels, for example, $^3F_2$ and $^3H_4$.

Table 4.2: NIR decay times for constant Yb^{3+} of ZrO_2:Yb^{3+} - Tm^{3+} samples and energy transfer efficiency.

Yb/Tm sample [%mol]	τ_{NIR} [μs]	η_{ET} [%]
2/0.05	535	53.47
2/0.1	487	57.65
2/0.5	273	76.26
2/1.5	234	79.65

It is possible to observe the contribution lack of this CR on τ_{eff} at 486 nm by comparing decay kinetics between 2/0.05 and 4/0.05 samples, which are shown on Figure 4.11. For 2/0.05 sample a single decay slope is presented in both 486 and 800 nm emissions. However, at 486 nm two components are formed as the Yb^{3+} concentration was increased to 4 mol%. It is suggested that fast component is ascribed to cross-relaxation and its reduction to the detriment of effective decay kinetics does not occur for 800 nm band. An slightly increment of

Tm^{3+} concentration reduces drastically the decay time for samples with constant 2 mol% of Yb^{3+}, showed on Figure 4.10. An increased number of acceptors increase the energy transfer and with it the decay times should increase. Table 4.2 shows the evidence of this increment in energy transfer for samples with constant 2 mol% of Yb^{3+} concentration. It is thus that those short values of decay time suggest the presence of energy migration processes. In addition, it should be noted that these samples have more organic remnants and surface defects due to treatment at 800^{o}C and low annealing time, and consequently could exhibit more phonon interaction.

4.5. COOPERATIVE EMISSION

The electronic configuration of Yb^{3+} makes the *4f* electrons less shielded than other ions of the lanthanide series, showing higher tendency to interact with neighbor ions. It has been reported that the interaction of two Yb ions produce visible emission. This emission is named cooperative up-conversion (CUC) and was first observed by Nakazawa in $YbPO_4$ [11]. Recently CUC emission was explained in terms of the relaxation of a virtual state formed by the ionic interaction of two Yb^{3+} ions bridged by an oxygen atom and enhanced for the high surface area of nanocrystals [12,13]. In this case, the overlapping between the Yb *4f* and the O *2p* orbitals enhance the interaction of neighboring active ions and subsequently the cooperative absorption. This effect can be promoted in nanocrystals due to the high surface area and surface reconstruction [14]. It means oxygen has an active role in the formed dimmer and not a passive role as it has been assumed when the Yb–Yb pair is considered [15-17], which subsequently emits a photon with the sum of energies.

The absorption spectra of ZrO_2:Yb^{3+} nanophosphors has been described based on previous results by our group, and it shows the characteristic broad absorption band with peaks centered at 910, 942, 972 and 1002 nm corresponding to the stark splitting of $^2F_{7/2} \rightarrow {}^2F_{5/2}$ transition of Yb^{3+} ion. In addition, a broad absorption band centered at ~460 nm was observed, produced by the simultaneous excitation of two Yb^{3+} ions. In this case, the pair Yb^{3+}-Yb^{3+} can be considered as a new ion with three energy levels: the ground state; the

typical energy level at ~10,300 cm^{-1} characteristic of a single ion; and an energy level at ~21,700 cm^{-1} associated to a cooperative absorption. Because this cooperative absorption band is strong and corresponds to the second harmonic of the infrared (IR) band it is considered as the physical evidence of the process described above. This was confirmed by obtaining the self-convolution of the NIR absorption band that matches exactly with the experimental cooperative absorption band. Cooperative up-conversion (CUC) emission was recently reported in ZrO_2:Yb^{3+} - Tm^{3+} nanocrystals as well as preliminary results of such effect on ZrO_2:Yb^{3+} for low concentrations [18,19]. Our group has previously reported a systematic characterization of CUC emission as a function of Yb^{3+} concentration [20].

Visible emission of Yb^{3+} - Tm^{3+} doped samples is shown in Figures 4.3 and 4.4. CUC emission occurs at 501 nm. It is approximately twice the energy of the IR luminescence of single Yb^{3+} ion suggesting that is the result of the radiative relaxation of excited Yb^{3+} pairs. The peaks at 474 and 486 nm are characteristic of Tm^{3+} emission $^1G_4 \rightarrow {}^3H_6$. CUC emission is overly intense in Tm^{3+} and imperceptible in Er^{3+} co-doped Yb^{3+} systems due to the fact that in Yb^{3+}- Er^{3+} pair the excitation is more efficient than in Yb^{3+} - Tm^{3+} pair because of the smaller resonance difference ΔE, along with its deficient energy transfer from $^3H_5$ level of Tm^{3+}. In the channel of transfer Yb^{3+} ($^2F_{5/2} \rightarrow {}^2F_{7/2}$):$Er^{3+}$ ($^4I_{15/2} \rightarrow {}^4I_{11/2}$), ΔE = 100 cm^{-1}, and in the channel of Yb^{3+} ($^2F_{5/2} \rightarrow {}^2F_{7/2}$):$Tm^{3+}$ ($^3H_6 \rightarrow {}^3H_5$), ΔE = 2000 cm^{-1}.. Moreover, the number of pump photons required in CUC emission was analyzed before (Figure 4.8). For CUC emission $n \approx 2$ confirming that such emission is the result of two-photon process.

4.5.1. VISIBLE EMISSION IN ZrO_2:Yb^{3+} WITH RARE EARTH REMNANTS

In fact, ZrO_2:Yb^{3+}-Tm^{3+} nanocrystal is the only studied system (at clear sight) that presents both CUC of Yb^{3+} and characteristic visible emission. CUC emission was not observed in the Yb^{3+}-Er^{3+} codoped system, even for concentration of Er^{3+} as lower as 0.1 mol%. Given the possibility that all the systems studied exhibit CUC emission since they are doped with Yb^{3+}, we proceeded to analyze the samples used for calculations of energy transfer efficiency. These samples are mainly doped with Yb^{3+}, so that the existence of other ions would be possible as traces. Thus, ZrO_2:Yb^{3+} sample doped at 2 mol% of Yb^{3+} and Er traces (Yb_{Er}) was

prepared and the visible emission of the system is shown in Figure 4.12. For the analysis, Yb^{3+} - Ho^{3+} and Yb^{3+} - Tm^{3+} spectra is added as guiding. Emissions related to Ho and Tm appeared in the emission, which origin could not be attributable to a purity control lack during synthesis due to the fact that all implements were new and never exposed to rare-earth precursors. We conclude that this type of contamination is originated by purity of Yb precursor (99.999%). It is important to point out that emission was clear and easy to be seen. Seven peaks are observed in the blue-green emission band. The line at 524 nm are characteristic of the $^2H_{11/2}$ + $^4S_{3/2}$ → $^4I_{15/2}$ transition of Er^{3+} due to the energy transfer from Yb^{3+} to Er^{3+} ion. Peaks at 540 and 550 nm as well as 560 nm shoulder are ascribed to $^5F_4$ + $^5S_2$ transition of Ho^{3+}. Bands centered at 474 and 486 nm are characteristic of the stark splitting $^1G_4$ → $^3H_6$ transition of Tm^{3+}, emission similar than the one obtained in the system ZrO_2:Tm^{3+}-Yb^{3+}. Finally the CUC emission at 501 nm is observed as a result of the Yb^{3+}- Yb^{3+} presence.

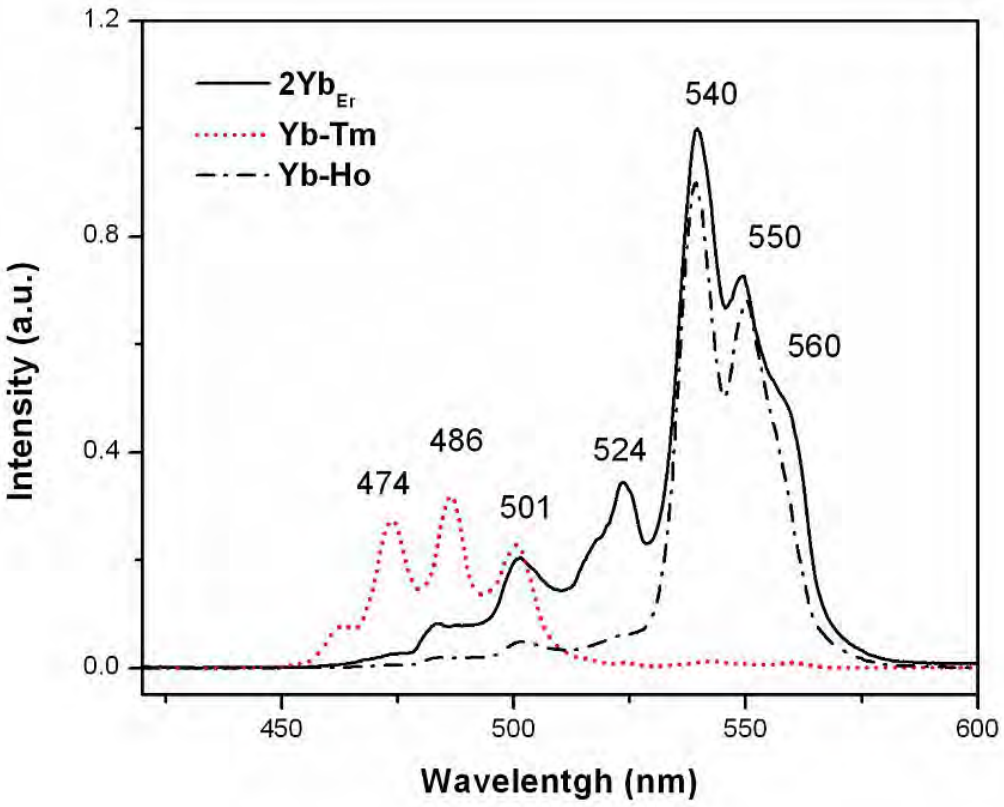

Figure 4.13: Excerpt of visible spectrum of Yb^{3+} (2 mol%) with traces of Er^{3+}. Emission bands of Ho^{3+} and Tm^{3+} are included as a guiding. All spectra are self-normalized and suitably scaled.

A sample with 2 mol% of Yb^{3+} and Ho traces (Yb_{Ho}) were consequently synthesized and its spectrum analyzed as to observe the CUC emission band, as is shown in Figure 4.13. Emissions related to transitions of Tm^{3+} appeared in the emission; however, it is difficult to determine the presence of Er^{3+} in the system. It can be suggested that Ho traces had better efficiency than those rare-earth remnants, as it was Yb^{3+} - Ho^{3+} the only system that presents notable luminescence at 0.001 mol% of Ho^{3+}. Once more, the CUC emission at 501 nm is observed as a result of the Yb^{3+}- Yb^{3+} presence. Because the presence of Er^{3+} and Tm^{3+} impurities were not detected in the absorption spectra, there has to be very low concentration. It is noticeable the strong intensity considering that concentration is probably of traces. This fact suggest a very efficient up-conversion processes involving traces of Tm^{3+} and Er^{3+} ions having the Yb^{3+} ions as sensitizers.

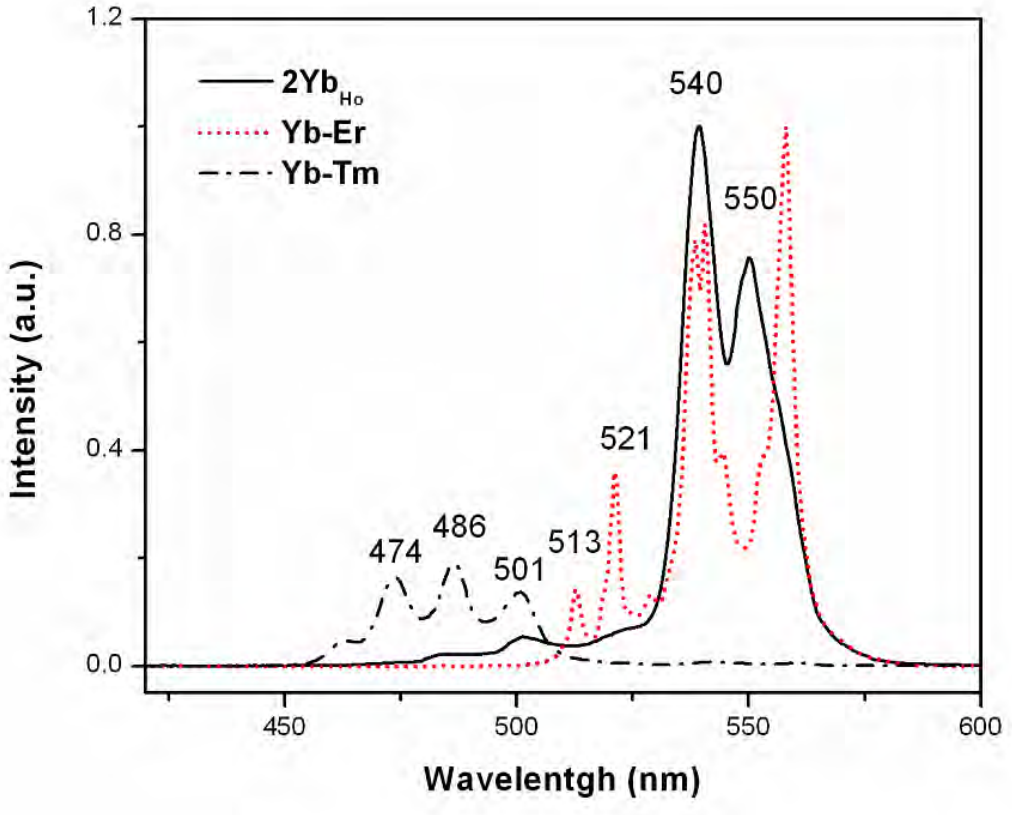

Figure 4.14: Excerpt of visible spectrum of Yb^{3+} (2 mol%) with traces of Ho^{3+}. Emission bands of Tm^{3+} and Er^{3+} are included as a guiding. All spectra are self-normalized and suitably scaled.

Finally, a sample with 2 mol% of Yb^{3+} and Tm traces (Yb_{Tm}) was synthesized and its spectrum analyzed as to observe the CUC emission band, as is shown in Figure 4.14. Figure shows peaks at 463, 474 and 486 nm ascribed to characteristic transitions of Tm. Peaks related to Er^{3+} transitions appeared in the emission, but out of which the peaks at 560 and 543 nm are easily identified. The peak in 524 nm exhibits an unusual shape, possibly by the notable Tm - Er interaction and the absence of any peaks from Ho. Furthermore, the peak at 501 nm ascribed to CUC emission of Yb^{3+} pairs is well defined, and resulted to be the most intense among the emission peaks related to Yb^{3+} - Tm^{3+} system.

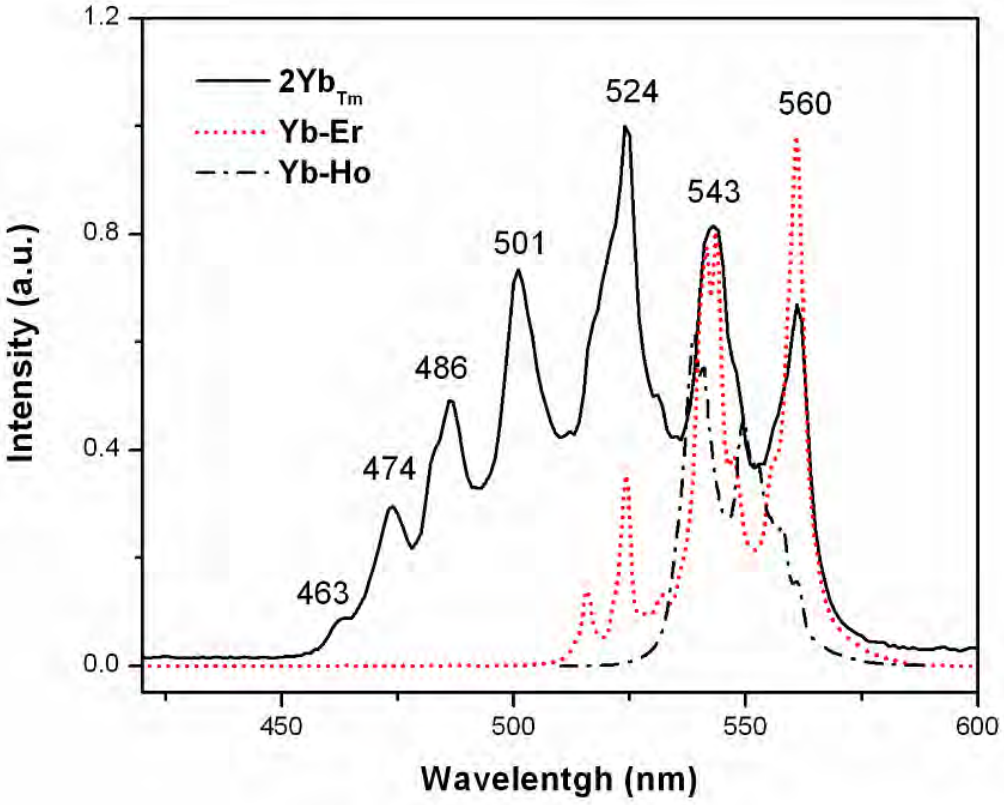

Figure 4.14: Excerpt of visible spectrum of Yb^{3+} (2 mol%) with traces of Tm^{3+}. Emission bands of Er^{3+} and Ho^{3+} are included as a guiding. All spectra are self-normalized and suitably scaled.

Therefore we can conclude that the emission from traces is intense, highly efficient and that are caused by contamination of the sample. The fact that the samples exhibit different spectra, suggests that such contamination originates from the laboratory implements and the dominant ion trace is related to the system that was being synthesized. Nonetheless, minor

traces are present and their quantity is even lower, originated by purity of Yb precursor. From the graphs, it is suggested that CUC emission only occurs with the presence of Tm, which is present in all studied samples.

4.5.2. LUMINESCENCE DECAY TIME IN ZrO_2:Yb^{3+} WITH RARE-EARTH REMNANTS

The luminescent decay time τ of emission at 501 nm was measured to analyze the dynamics of up-conversion, and resulted values are in Table 4.3. It is expected that $\tau_{cuc} \approx 0.5\tau_{nir}$ if only CUC and NIR emission are considered. Decay times of both NIR and CUC for Yb^{3+} doped samples with impurities of Er, Ho and Tm were considered. Decay time of NIR signal diminishes as the concentration increases; this can be noticed clearly on set with Ho remnants.

Table 4.2: Effective decay times for both NIR and CUC emission for Yb^{3+} doped samples with rare-earth remnants. τ_{NIR}/τ_{CUC} ratio are listed for each sample.

Yb [%mol]	Remnant	τ_{NIR} [μs]	τ_{CUC} [μs]	τ_{NIR}/τ_{CUC}
1	Er	1150	496	0.431
2	Er	869	442	0.508
4	Er	860	408	0.474
1	Ho	812	414	0.510
2	Ho	883	454	0.514
5	Ho	447	404	0.903
10	Ho	259	243	0.938
2	Tm	1150	557	0.484

For 2 mol% doped samples with holmium remnants τ_{nir} = 812, 883, 447 and 259 μs; and for CUC emission τ_{cuc} = 414, 454, 404 and 243 μs respectively. The τ_{nir} behavior suggest the

formations of clusters by the increment of concentration, part of those clusters are due to pair formation. Effect of impurities such as OH^- promoting non-radiative processes can be discarded considering the strong effect of clustering. The ratio $\tau_{cuc}/(\tau_{eff})_{nir} \sim 0.5$ for samples with 2 mol% of Yb^{3+} confirms that CUC emission results from the simultaneous excitation of both active ions in the Yb pairs. Similar ratio is obtained for 4 mol% sample with Er impurities and for 1 mol% with both Ho an Er impurities respectively. Clustering, and then luminescent quenching of both single and pair emission, is confirmed by the reduction of decay times of both emitted signals and the little deviation of single exponential of NIR signal. With these results we conclude that CUC is only highly efficient on Yb-Tm system. The smaller resonance difference ΔE in the first channel of energy transfer between the donor and the acceptor allow mainly the persistence of a greater amount of Yb^{3+}-Yb^{3+} pairs.

4.6. REFERENCES

[1] A. Patra, C.S. Friend, R. Kapoor, P.N. Prasad, "Upconversion in Er^{3+}:ZrO_2 Nanocrystals", J. Phys. Chem. B **106**, 1909-1912 (2002)

[2] S. Heer, O. Lehmann, M. Haase, H.U. Gudel, Angew, "Blue, Green, and Red Upconversion Emission from Lanthanide-Doped $LuPO_4$ and $YbPO_4$ Nanocrystals in a Transparent Colloidal Solution", Angew. Chem. Int. Ed. **42**, 3179 (2003)

[3] T. Lopez-Luke, E. De la Rosa, P. Salas, C. Angeles-Chavez, L.A. Diaz-Torres, S. Bribiesca, "Enhancing the up-conversion emission of ZrO_2 : Er^{3+} nanocrystals prepared by a micelle process", Journal of Physical Chemistry C **111**, 17110-17117 (2007)

[4] E. De la Rosa-Cruz, L.A. Diaz-Torres, R.A. Rodiguez-Rojas, M.A. Meneses-Nava, O. Barbosa-Garcia, P. Salas, "Luminescence and visible upconversion in nanocrystalline ZrO_2 : Er^{3+}", Appl. Phys. Lett. **83**(24), 4903 (2003)

[5] P. Li, I.W. Chen, J.E. Penner-Hahn, "Effect of Dopants on Zirconia Stabilization–An X-ray Absorbtion Study: II, Tetravalent Dopants", J. Am. Ceram. Soc. **77**, 1281 (1994)

[6] T. López-Luke, E. De La Rosa, D. Solis, P. Salas, C. Angeles-Chavez, J. A. Montoya, L. A. Diaz-Torres, and S. Bribiesca, "Effect of the CTAB concentration on the upconversion emission of ZrO_2:Er^{3+} nanocrystals", Optical Materials **29**(1),31-37 (2006)

[7] D. Solís, T. López-Luke, E. De la Rosa, P. Salas and C. Angeles-Chavez, "Surfactant effect on the upconversion emission and decay time of ZrO_2:Yb-Er nanocrystals", Journal of Luminescence, **129**(5), 449-455 (2009)

[8] R.C. Garvie and P.S. Nicholson, "Structure and Thermomechanical Properties of Partially Stabilized Zirconia in the CaO-ZrO_2 System", J. Amer. Ceram. Soc. **55**, 152 (1972)

[9] F. Vetrone, J.C. Boyer, J.A. Capobianco, A. Speghini, and M. Bettinelli, "NIR to visible upconversion in nanocrystalline and bulk Lu_2O_3 : Er^{3+}," Journal of Physical Chemistry B **106**, 5622–5628 (2002)

[10] H. Desirena, E. De la Rosa, A. Shulzgen, S. Shabet and N. Peyghambarian, "Er^{3+} and Yb^{3+} concentration effect in the spectroscopic properties and energy transfer in Yb^{3+}/Er^{3+} codoped tellurite glasses", J. Phys. D: Appl. Phys. **41**(09), 5102 (2008)

[11] E. Nakazawa; S. Shionoya, "Cooperative Luminescence in $YbPO_4$", Phys. Rev. Lett. **25**, 1710-1712 (1970)

[12] T. Ishii, "First-principles calculations for the cooperative transitions of Yb^{3+} dimer clusters in $Y_3Al_5O_{12}$ and Y_2O_3 crystals," The Journal of Chemical Physics **122**, 024705-024706 (2005)

[13] H. J. Schugar, E. I. Solomon, W. L. Cleveland and L. Goodman, "Simultaneous pair electronic transitions in Yb_2O_3", J. Am. Chem. Soc. **97**:22, 6442-6450 (1975)

[14] F. S. De Vicente, A. C. De Castro, M. F. De Souza, and M. S. Li, "Luminiscence and structure of Er^{3+} doped zirconia films deposited by electron beam evaporation", Thin. Solid Films **418**, 222-7 (2002)

[15] E. Nakazawa and S. Shionoya, "Cooperative Luminescence in $YbPO_4$," Physical Review Letters **25**, 1710 (1970)

[16] F. Auzel, D. Meichenin, F. Pellé, and P. Goldner, "Cooperative luminescence as a defining process for RE-ions clustering in glasses and crystals," Optical Materials **4**, 35-41 (1994)

[17] P. Gerner, O. S. Wenger, R. Valiente, and H. U. Güdel, "Green and Red Light Emission by Upconversion from the near-IR in Yb3+ Doped CsMnBr3," Inorganic Chemistry 40, 4534-4542 (2001)

[18] A. Patra, S. Saha, M. Alencar, N. Rakov, G. Maciel, "Blue upconversion emission of Tm^{3+}-Yb^{3+} in ZrO_2 nanocrystals: Role of Yb^{3+} ions", Chem. Phys. Lett. 407, 477 (2005).

[19] E. De la Rosa, P. Salas, L.A. Diaz-Torres, A. Martinez, C. Angeles, "Strong visible cooperative up-conversion emission in ZrO2 : Yb^{3+} nanocrystals", J. of Nanosc. and nanotech., **5**, 1480-1486 (2005)

[20] E. de la Rosa, D. Solis, L. A. Diaz-Torres, P. Salas , C. Angeles-Chavez, O. Meza, "Blue-green upconversion emission in ZrO_2:Yb^{3+} nanocrystals," Journal of Applied Physics, 104(10), 6 (2008)

CHAPTER 5

APPLICATIONS

5.1. INTRODUCTION

The past couple of years have seen significant advances in the synthesis and creation of metal, oxide, and semiconductor nanocrystals. Proof of this can be seen in the increasing amount of literature on the synthesis of different sizes and shapes of nanocrystals. The advances in synthesis have surpassed our understanding of fundamental factors (such as growth mechanisms) and have generated a whole range of new nanocrystalline materials with forms and shapes that had not previously been imagined. This period has also brought forth developments in our understanding of the fundamental properties of nanocrystalline matter. Several devices relying on the unique properties of nanocrystals have been produced in lab settings towards their potential applications [1]. Proof of concept experiments have been carried out to test chemically prepared nanocrystals in single electron devices; for example capacitors [2] and nano switches [3]. A more tangible application for nanocrystals is their potential use as vapor sensors prepared by multilayer deposition [4] or spin coating techniques [4-7]. These devices produce a reversible and rapid response to different kinds of vapors. In other cases, sensitivity on a part per million scale has been achieved [8]. Superparamagnetic oxide nanoparticles have therefore found several biomedical applications as they possess no known toxicity [9]. It has been proposed that hyperthermia, magnetic field induced heating of superparamagnetic particles, could be used to destroy diseased cells and thereby treat cancer. Numerous studies have been carried out towards achieving this goal [10,11].

In the field of biomedical optics, of interest to us, quantum dots have been used as luminescent tags by certain advantages over conventional fluorescent dyes. They are highly photo-stable, possess large Stoke shifts and emit in a narrower range (with emission peak widths a third of the width of molecular species). It is possible to simultaneously obtain intense emission at several different wavelengths by exciting at a single wavelength by using nanocrystals of the same material but different sizes. Furthermore, emission from quantum dots is not easily susceptible to quenching. Several *in vivo* [12,13] and *in vitro* [1416] studies have been carried out using quantum dots as either specific or non-specific labels. The

intrinsic advantage of quantum dots lies in its broadband absorption and customizable emission wavelength as mentioned above. However, its down-conversion fluorescent nature and unique property of augmented absorption at higher energies makes requisite the use of excitation wavelengths in the UV-visible range to achieve emissions of optimal fluorescent intensity. Unfortunately, this advantage is effectively negated by the pronounced effect of tissue attenuation and auto fluorescence at these shorter wavelengths [17-19].

Up-conversion nanophosphors on the other hand utilize excitation energies within the tissue transparency window (NIR spectral region), thereby minimizing attenuation and auto fluorescence, improving signal-to-noise ratio. A parallel consequence is that penetration depth is also increased from a few mm for UV to as deep as 15 cm in fibrofatty tissues [19]. Excited with a 980nm NIR laser, lanthanide-doped NaYF4 nanocrystals demonstrated strong up-conversion fluorescence at green (540 nm) and red (653 nm) wavelengths, with a magnitude seven orders above CdSe-ZnS quantum dots [18,20]. Cells and tissues are virtually transparent to NIR light, hence are less likely to be damaged by irradiation as compared to UV light. In terms of toxicity, the rare earth elements used in synthesizing up-conversion nanoparticles (Ytterbium, Erbium, Thulium) are of lower toxicity than quantum dots, which typically comprise semi-conductor metals known to be toxic in their elemental forms [17,20].
As do quantum dots, the up-conversion nanocrystals also demonstrate high resistance to photo bleaching [21]. For these reasons, it is judged that overall up-conversion nanocrystals are significantly advantageous for use as fluorescent probes vis-a-vis quantum dots and organic fluorophore molecules.

5.1.1. TOWARDS APPLICATIVE LUMINESCENT OXIDE NANOPARTICLES

In the phosphor research field there are some working hypotheses. One of them is that “luminescence efficiency of fine (nano) particle phosphor is low”. When the particle size of a phosphor material is reduced, luminescence efficiency decreases significantly [22]. To summarize, we confirm that the luminescence efficiency of fine (nano) particle phosphor is indeed low. Therefore, does the nanophosphor have any practical use?

There are still some trials remaining that can help improve the luminescence efficiency of the nanophosphors using precise process control. Nishisu et al. reported the synthesis of 300–400 nm Y_2O_3: Eu spherical phosphor by a uniform coprecipitation method [23]. The luminance of the nanophosphor, by 147 nm excitation, is comparable to that of a conventional sample synthesized at high temperature. Kakihana et al. reported synthesis of high-luminance 200–300 nm Y_2O_2S: Eu phosphors by complex homogeneous precipitation methods [24]. Masui et al. synthesized new layered $Gd_2O_2CO_3$:xTb^{3+} green phosphor in $0.476{\cdot}Li_2CO_3$–$0.270{\cdot}Na_2CO_3$–$0.254{\cdot}K_2CO_3$. This nanophosphor shows higher luminance than that of commercial lamp phosphors [25]. From these processing studies can be concluded that the choice of the precursor and the optimization of heating conditions that prevent the aggregation are very important.

The emitted color by our most luminescent Yb^{3+} - Ho^{3+} sample (2/0.001 mol%) was analyzed by determining the chromatic coordinate in the CIE 1931 space (CIExy) using its spectrum data. The obtained value was (0.289, 0.699) that is almost constant along the different concentrations of Yb^{3+} - Ho^{3+} samples. This is because the other bands represent only about 2% of the emitted signal. Luminance from 2/0.001 mol% sample was calculated obtaining a value of 240 ± 16.8 lux. $8.7X10^{-3}$ lm was achieved after converting to lumen (a more appropriate unit). To get an idea of efficiency, we used the 370 mW power from the CW laser diode at excitation point, obtaining the perfectible value of $23.6X10^{-3}$ lm/W.

Once it is know that the issue of the intensity is an increasingly viable feature, the second point to consider is related to the range of colors that can be obtained from a nanophosphor by a single source of excitation. Having the ability to manipulate the color of phosphorus, makes their use as bio-markers becomes more attractive and useful. Therefore we focus on this issue trying to tune white light.

Solid-state white lighting is an application that comes from control of chromaticity, as this is a special case of color tuning. They are promising candidates for white LED applications.

Rayleigh scattering decreases in proportion to particle size by sixth orders. Therefore, the nanoparticles dispersed in resins scatter light less vigorously and become transparent. Rare earth complex phosphors are dispersed in plastics [26]. Fukui et al. reported nanocluster phosphors containing rare earth ions [27]. Isobe et al. reported the transparent phosphor sheet of nano ZnS:Mn and $Y_3Al_5O_{12}$:Ce dispersed in resins [27].

As mentioned, white LEDs are one of the promising applications for nanophosphors. In this chapter we are interested to produce white light emission based on rare earth doped nanocrystals. The general properties of rare-earths and their electronic states and transitions are well understood. These interactions can enhance or inhibit performance and provide mechanisms for manipulating the optical properties of the material. ZrO_2:Tm^{3+}- Yb^{3+}- Er^{3+}- Ho^{3+} nano-crystalline samples were synthesized by the sol-gel method and up-conversion emission properties were analyzed as a function of different concentrations of rare-earth ions. The samples were pumped at 970 nm with a semiconductor laser source. The addition of different ion concentrations affects the shape and peak intensities of the measured blue, green and red bands. Results showed in this section tend to demonstrate a feasible control of the emission chromaticity coordinates, and present an approximation to the equipotential white chromaticity coordinates.

On this chapter is presented the technique in which we studied the problem of color tuning, as well as the methodology used to achieve the objective.

5.2. COLORIMETRIC CONSIDERATIONS

A human observer has no way of knowing the spectral composition of a colored object from its appearance. Colorimetry provides a system for color measurement based on the concept of equivalent-appearing stimuli. In a color match, two differing fields of spectral radiation appear identical, that is the base of a *metamer*. The match represents a unique neural state in which neural signals generated by the fields are identical.

(a) Metamers

Metameric lights are lights that have dissimilar spectra that are seen as the same by the observer. In a typical color-matching experiment using additive lights, the metamers are presented in a bipartite field. For 2^{o} foveal fields, metamers have three important properties that allow the treatment of color mixture as a linear system (Grassmann, 1853):

1. The additive property. When identical radiation is added to both sides of a color mixture field, the metamerism is unchanged.
2. The scalar property. When both sides of the color mixture field are changed by the same proportion in radiance, the metamerism is unchanged.
3. The associative property. A metameric mixture may be substituted for a light without changing the metameric property of the color fields.

According to Grassmann's laws, a color match is invariant under a variety of experimental conditions that may alter the appearance of the matching fields. Metameric matches will hold with the addition of a chromatic surround or following pre-exposure to a moderately bright chromatic field.

(b) Trichromacy

A fundamental property of normal human color vision is the existence of color matches that differ in spectral composition. It is possible to find a metamer for any light (the spectral power distribution, or SPD) by varying the energies of three fixed lights, called primaries. The terms trichromat and trichromacy refer to this property of human color vision. There is wide freedom of choice for primaries. A formal requirement is that one primary cannot be metameric to a mixture of the other two. It is desirable in practice that the primaries be spectrally separated as much as possible and that the matching field is at a mid-photopic level. The choice of primaries is dictated largely by experimental convenience. Primaries may or may not be spectral (i.e., with discrete distribution). However, in the development of a

colorimetric system, the test lights should be spectral or near-spectral in order to derive the largest color gamut.

It has become customary to present the results of color mixture experiments as color equations. Suppose we have three primaries, P_1, P_2, P_3 and a test light, S, arranged in a bipartite field. We find that a mixture of S and P_3 appears identical to a mixture of P_1 and P_2, when the radiant energies of S, P_1, P_2, P_3 are P_S, $P_{S,1}$, $P_{S,2}$ and $P_{S,3}$ respectively. This is written:

$$P_S S \oplus P_{S,3}\,\mathrm{P}_3 \equiv P_{S,1}\,\mathrm{P}_1 \oplus P_{S,2}\,\mathrm{P}_2 \tag{5.1}$$

Where $\cong$ means visually identical and $\oplus$ means physical mixture. The quantities $P_{S,1}$, $P_{S,2}$ and $P_{S,3}$ are called the tristimulus values. Their subscripts identify the test light (S) and the primaries (1, 2 or 3). Using Grassmann's law we treat this mixture equation as an algebraic equation and express the match in terms of S:

$$P_S S = P_{S,1}\,\mathrm{P}_1 + P_{S,2}\,\mathrm{P}_2 - P_{S,3}\,\mathrm{P}_3 \tag{5.2}$$

The minus sign reflects the fact that, in the color match, primary P_3 was added to the test light. Given a set of primaries, (P_1, P_2, P_3), a color match can be made to all lights, of any spectral power distribution. When the test light has a narrow spectral band, one of the primaries is either negative (physically superimposed with the spectral test light to match the remaining two primaries) or zero. When the test light has a broad spectral power distribution the three primaries may all be positive. As a consequence of Grassmann's law, the match for a broad spectral power distribution can be considered the sum of constituent narrowband spectral matches. Consider a distribution of unit energy at every spectral wavelength (the equal energy spectrum, abbreviated EES). According to the additivity law, the color match for this distribution is considered to be the sum of matches within unit energies of the spectral wavelengths.

5.2.1. PRINCIPLES AND PROCEDURES

The importance of trichromacy in industry is the prediction of visual equivalence for a wide array of spectral power distributions. The colorimetric data provides a numerical value at unit

wavelength steps, which can be used to calculate tristimulus values for any spectral power distribution.

In 1931, the CIE (Commission Internationale de l'Eclairage) defined a standard observer for colorimetry, based on 2^{o} color matching. The 2^{o} observer is recommended for fields up to 4^{o}. A 10^{o} observer was defined in 1964 (CIE, 1964). The characteristics of the large-field observer are recommended for visual stimuli whose extent exceeds 4^{o}, but should only be used for high photopic illuminances. Revision and evaluation of the standard observers remains a current interest for the CIE.

The 1931 CIE standard observer incorporates both colorimetric and photometric behaviors. The initial dataset consisted of averaged chromaticity coefficients obtained by Wright (1929) and Guild (1931). These were expressed in Wright's primaries and normalized to the Standard Illuminant B. The luminous units of the primaries were adjusted to be consistent with the location of Standard Illuminant B and with the luminosity of the 1924 CIE standard photometric observer. Two equivalent statements of the color-matching behavior of the 1931 CIE standard observer were embodied in the (R,G,B) and (X,Y,Z) systems of units. The CIE 1931 color space is intended to describe all colors visible to the naked eye and can be displayed as a three-dimensional cube, although it is usually depicted in two dimensions. In 1931, the CIE established a formal procedure for color matching. Taking the curves for different laboratories and mapping them to the same primary set, three curves were obtained called $\bar{x}$, $\bar{y}$, $\bar{z}$, formally adopted by the CIE in that same year. The three curves are called color matching functions or correspondence color-matching functions. These define a specific standard observer called CIE 1931 Standard Colorimetric Observer, usually called the 2^{o} observer (Figure 5.1 [28]).

The three functions indicate the amount of each primary that is needed to match the color of one watt of radiant power at the indicated wavelength. It has been established so that the areas under the three curves are equal to each other. The three tristimulus values are set up

in such a way so that they are equal for the color white. The triad of tristimulus values X, Y, and Z for a given color is calculated from the integration of the product of the equalization functions $\bar{x}$, $\bar{y}$, $\bar{z}$, the chromatic stimulus $\Phi\lambda$ and a numerical constant *k* which defines the SPD under analysis [29], as follows.

$$X = k\int_{380\,nm}^{780\,nm}\phi_\lambda(\lambda)\bar{x}(\lambda)d\lambda,\quad Y = k\int_{380\,nm}^{780\,nm}\phi_\lambda(\lambda)\bar{y}(\lambda)d\lambda,\quad Z = k\int_{380\,nm}^{780\,nm}\phi_\lambda(\lambda)\bar{z}(\lambda)d\lambda \tag{5.3}$$

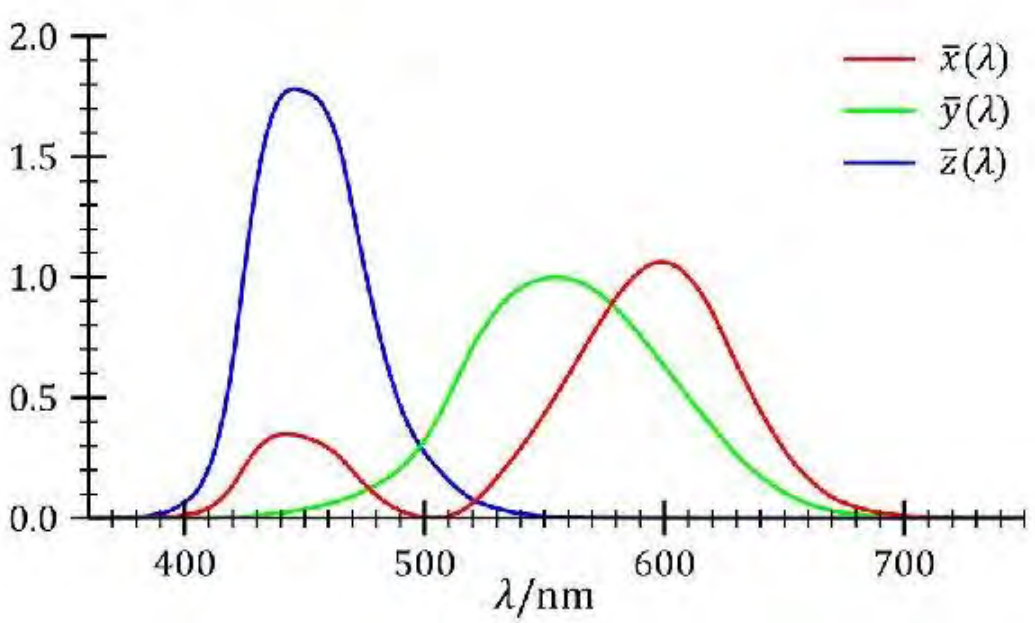

Figure 5.1: CIE 1931 Standard Colorimetric Observer graph. Response curve for color matching functions $\bar{x}$, $\bar{y}$, $\bar{z}$.

The CIE XYZ color space was deliberately designed so that the Y parameter was a measure of the brightness or luminance of a color. The chromaticity of a color was then specified by the two derived parameters x and y, two of the three normalized values which are functions of all three tristimulus values X, Y, and Z. For the xy subspace new x and y chromaticity values are obtained by:

$$x = \frac{X}{X+Y+Z} \qquad y = \frac{Y}{X+Y+Z} \tag{5.4}$$

The corresponding chromaticity diagram is shown in Figure 5.2 [30]. The outer curve is called locus and marks the boundary spectrum, showing the corresponding wavelengths. The straight line at the bottom between the blue and red is the purple line. This line indicates all additive mixtures of red and blue (purple tones) and determines the colors outside the visible spectrum. The three imaginary primaries coordinates on the diagram that give rise to the CIE 1931 chromaticity coordinates are (1,0), (0,1) and (0,0), respectively. The diagram has some interesting properties: A distance on the xy chromaticity diagram does not correspond to the degree of difference between two colors. Light with a flat energy spectrum corresponds to the point (x,y) = (1/3,1/3) (equipotential white). All the colors that lie in a straight line between the two points can be formed by mixing the two colors. The entire gamut of human vision cannot be completely covered using only three real sources. The diagram represents all of the chromaticity visible by an average person.

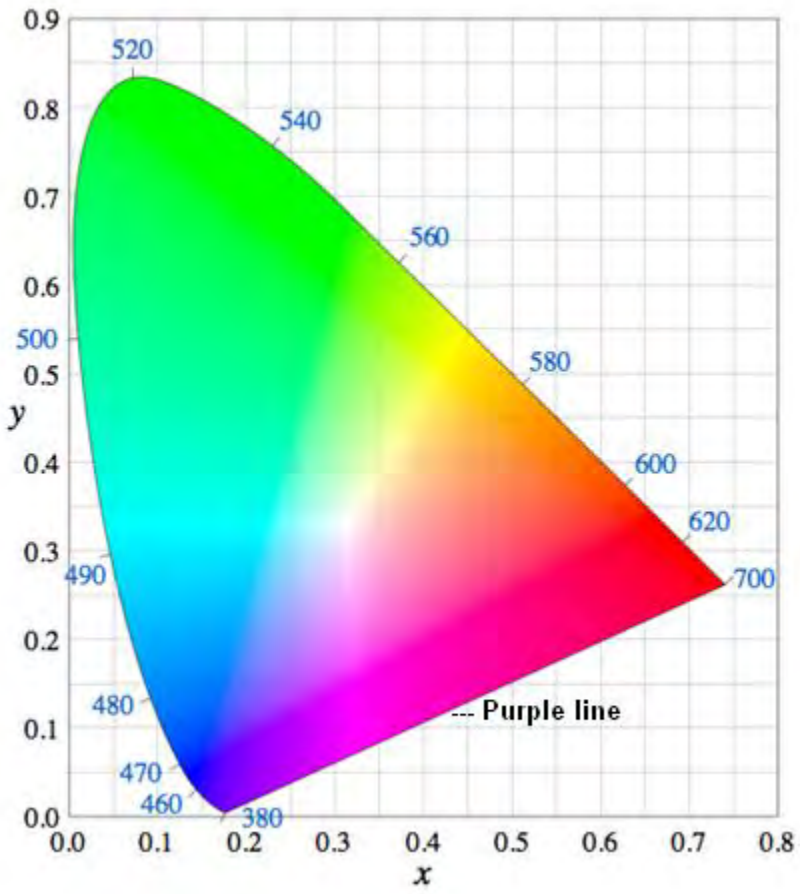

Figure 5.2: CIE xy chromaticity diagram.

5.3. SYNTONIZED WHITE UP-CONVERTED EMISSION BY Tm^{3+}-Yb^{3+}-Er^{3+}-Ho^{3+} CODOPED ZrO_2 NANOCRYSTALS

The nano-crystalline phosphors under study are composed of zirconium dioxide (ZrO_2) acting as a host material supporting a combination of ytterbium, erbium and thulium ions that form the active material. Phosphors were produced by the micelle method and have the following composition: a • Yb_2O_3 - b •Er_2O_3 - c • Tm_2O_3 - d • Ho_2O_3 - (100-a-b-c-d) • ZrO_2 (% mol). A complete description of synthesis and sintering is detailed in chapter 2.

These samples were produced with different concentrations of doping agents, thus obtaining a variety of spectra after excitation at 970 nm with a diode laser. The resulting emission color is difficult to predict when the system involves more than two ions, mainly due to the complex excitation dynamics. Up-conversion phenomena involve the excitation of active ions (lanthanides) to a higher level than could be achieved by absorbing a single photon, with the required additional energy transferred from other active ions within the crystal. The crucial aspect to our analysis is the emission spectrum of the samples. Using a spectrophotometer, the spectral power distribution (SPD) can be obtained from each sample, and the combination of ion concentrations for obtaining a particular color can be inferred.

5.3.1. METHODOLOGY

Luminescence characterization for a multi-doped crystal is time consuming and usually requires a significant amount of measurements and samples. Taking into consideration the knowledge previously obtained during the study of co-doped systems, a faster approach could be feasible. In order to obtain the behaviour of the system in the shortest time possible, as well as rapidly implementing results, a new methodology was created and is explained next. The chart from Figure 5.3 summarizes the activities involved.

The first step is considering any previous knowledge on the up-conversion (UC) of required ions. The next step is the synthesis of samples. Acquisition of spectra using a spectrometer is the third step, from which chromatic coordinates are then calculated by means of software and obtains coordinates in the CIE 1931 color space. From the spectra obtained for each sample, we proceed to calculate numerically the color coordinates using equation (5.3). The CIE recommends the use of the entire visible spectrum (360 to 830 nm in 1 nm intervals) for the calculation of tristimulus values, but for practical purposes, we can use a narrower field of 380 to 780 nm in intervals of 5 nm. This process was accomplished through a program designed in Matlab®, which can generate results quickly and place the coordinates on a chromaticity diagram. Then the distance from the reference E is calculated and considered for the next step.

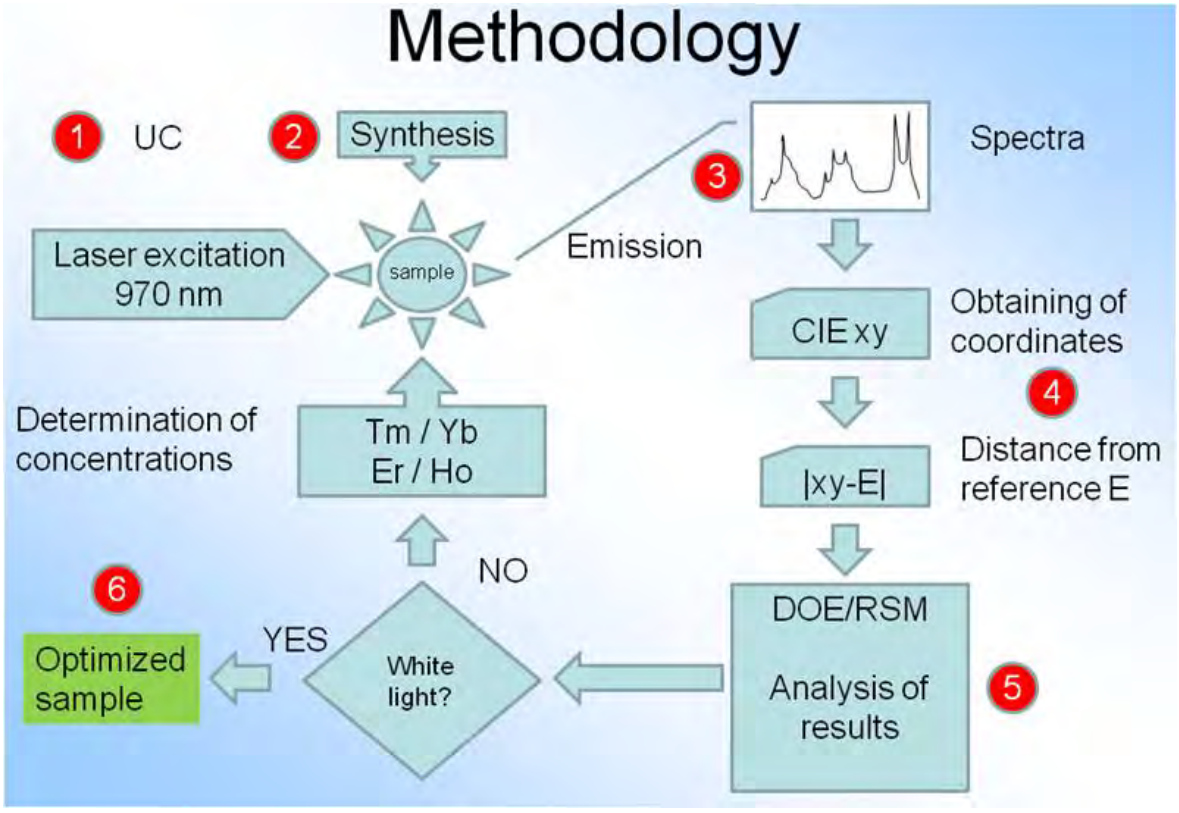

Figure 5.3: Flow chart describing the implemented planning methodology.

Before the color computation and the material synthesis, it is necessary to plan a set of samples that will allow us to infer the appropriate combination of ion concentrations. We had doubts about including Ho^{3+} due to its high green emission. The Ho^{3+} ion could be suitable for a system that requires a Yb^{3+}-Er^{3+} combination that reduces green emission. These three ions should be optimized for the intensity produced by the Tm ion in order to produce a balanced emission. The inclusion of four ions changes the excitation dynamics in a way that cannot be predicted using our own previous works [31,32]. According to the previous explanation we considered necessary to implement a design of experiments (DOE) methodology that converts this planning into a recursive process (step five). If the goal is achieved, then the methodology is complete (step six).

The experimental design is a statistical technique that allows the identification and quantification of causes and effects within an experiment. This is done by a deliberate manipulation of one or more variables in order to measure their effects on another variable of interest. The correct approach to dealing with several factors is to conduct a factorial experiment. This is an experimental strategy in which factors are varied together, instead of one at a time. The major disadvantage of the one-factor-at-a-time strategy is that it fails to consider any possible *interaction* between the factors. An *interaction* is the failure of the one factor to produce the same effect on the response at different levels of another factor. Interactions between factors are very common, and if they occur, the one-factor-at-a-time strategy will usually produce poor results. Experimental design enables the experimenter to investigate the individual effects of each factor (or the main effects) and to determine whether the factors interact. Thus the factorial experimental design concept is extremely important.

To illustrate how a factorial experiment is conducted, a two-factor factorial experiment is considered for studying the joint effects of these two factors. This experiment has both factors at two levels and that all possible combinations of the two factors across their levels are used in the design. Geometrically, the four runs form the corners of a square. This

particular type of factorial experiment is called 2^2 factorial design (two factors, each at two levels). Figure 5.4 shows the results of performing the factorial experiment.

Generally, if there are *k* factors, each at two levels, the factorial design would require 2^k runs. In any factorial design, all possible combinations of the levels of the factors are used. Clearly, as the number of factors of interest increases, the number of runs required increases rapidly; for instance, a 10-factor experiment with all factors at two levels would require 1024 runs. This quickly becomes infeasible from a time and resource viewpoint. Fortunately, if there are four to five or more factors, it is usually unnecessary to run all possible combinations of factors levels. A ***fractional factorial experiment*** is a variation of the basic factorial design in which only a subset of the runs are made. It will provide good information about the main effects of the factors as well as some information about how these factors interact. Fractional factorial designs are used extensively in industrial research and development, and for process improvement.

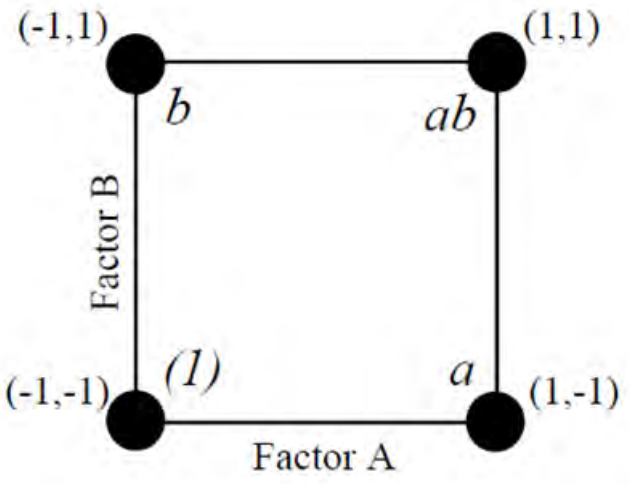

Figure 5.4: Geometric representation of a 2^2 factorial design. High and low levels are indicated as (1) and (-1) respectively; and factor under test is labeled on each inner corner.

Factors have an effect on the variable of interest, and these data are used to determine how the response (variable of interest) is related to all factors. With the obtained information is possible to make a model that describes these effects and interactions. An easy way to estimate a first-degree polynomial model is to use fractional factorial designs. This is

sufficient to determine which variables have an impact on the response or variable(s) of interest. Once we assume that only significant explanatory variables are left, it may be followed by a more complicated design based on Response Surface Methodology (RSM). As an important subject in the statistical design of experiments, the RSM is a collection of mathematical and statistical techniques useful for the modeling and analysis of problems in which a response of interest is influenced by several variables and the objective is to optimize this response.

In most RSM problems, the true response function *f* is unknown. In order to develop a proper approximation for *f*, the experimenter usually starts with a low-order polynomial in some small region. If the response can be defined by a linear function of independent variables, then the approximating function is a first-order model. If there is a curvature in the response surface, then a higher degree polynomial should be used. The approximating function is called a second-order model. In general all RSM problems use either one or the mixture of the both of these models. In each model, the levels of each factor are independent of the levels of other factors. In order to get the most efficient result in the approximation of polynomials the proper experimental design must be used to collect data. Once the data are collected, the Method of Least Square is used to estimate the parameters in the polynomials. The response surface analysis is performed by using the fitted surface.

Therefore, the objective of studying RSM can be accomplish by (1) understanding the topography of the response surface (local maximum, local minimum, ridge lines), and (2) finding the region where the optimal response occurs. The goal is to move rapidly and efficiently along a path to get to a maximum or a minimum response so that the response is optimized. We invite the reader to consult related literature from Montgomery [33], or any others, for further information related to this DOE technique.

5.3.2. EXPERIMENTAL

First, we considered the need to make test samples in order to elucidate the relation between the resulting color and the ion concentration. Based on our own previous work, five samples

were synthesized and the resulting color coordinates for each sample were obtained. We skipped the Ho^{3+} ion, for which we had already considered its adverse impact on the resulting emission. Concentrations are shown in Table 5.1, and resulting coordinates for each emission are represented in the chart in Figure 5.5. With this information we proceed to set lower and upper limits for each ion concentration, which is a relevant aspect for implementing the DOE methodology.

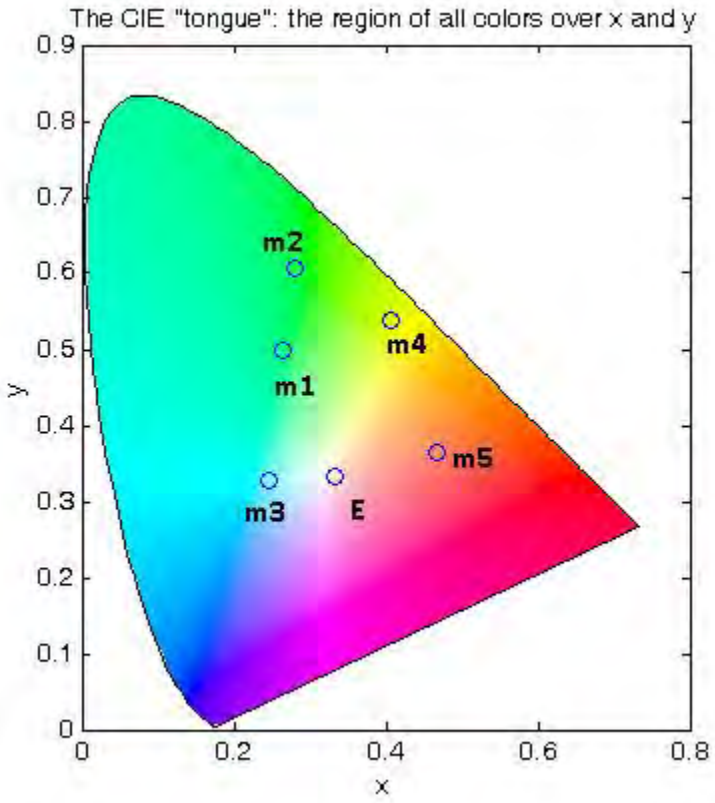

Figure 5.5: Distribution of chromatic coordinates for test samples into the CIE xy chromaticity diagram. Point E is the equipotential white that is used as a reference.

Table 5.1: Concentrations of test samples. Ho^{3+} ion effect was omitted. Quantities are in mol%.

Sample	Tm	Yb	Er
m1	0.2	5	0.2
m2	0.01	5	0.2
m3	0.2	5	1
m4	0.2	5	1.5
m5	0.5	8	1.8

After the test samples were analyzed, we implemented a fractional design in which eight samples were synthesized to determine the effect of the four ions (Tm^{3+}, Yb^{3+}, Er^{3+} and Ho^{3+}) in order to obtain a linear model that relates the chromatic response with the ion concentration. Samples m2, m3 and m5 are a good example of green, blue and red samples respectively. From these samples we elucidate new levels. We reduced the high level to 5 and 1 mol% for Yb^{3+} and Er^{3+}, respectively, because there was significant signal attenuation. We also reduced by 50% the lower levels for Tm^{3+} and Er^{3+} to explore this direction of change. For Yb^{3+} the low level was set at 2 mol%, because it is the value used in samples with the highest emissions in previous systems. The red emission requires a high concentration of Er^{3+}, for this reason the inclusion of Ho^{3+} was reviewed, in order to offset the green region; we used a high level of 0.1 mol% for this ion. Concentrations are in Table 5.2, and resulting coordinates are represented in Figure 5.6.

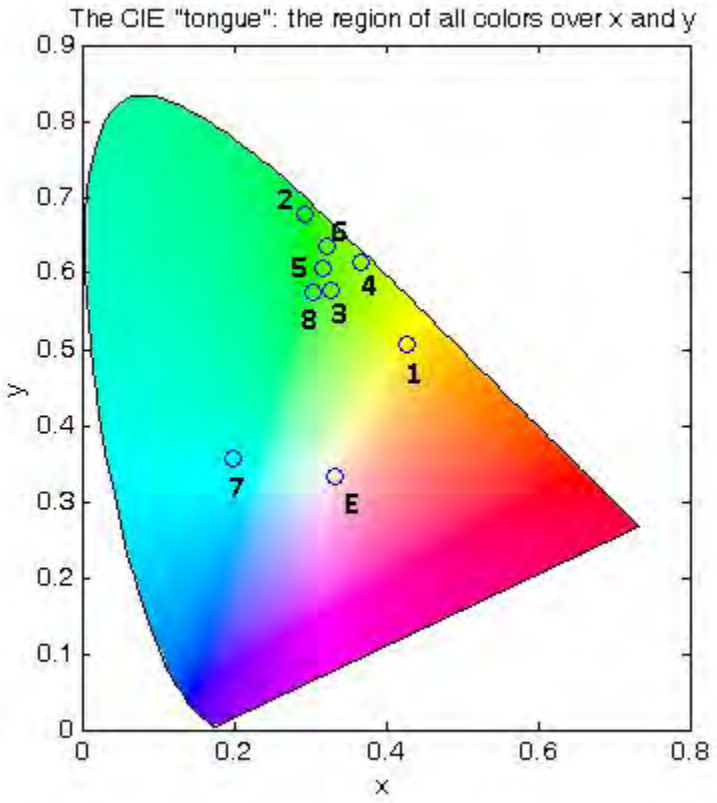

Figure 5.6: Distribution of chromatic coordinates for DOE samples into CIE xy chromaticity diagram. Point E is the equipotential white that is used for reference.

After obtaining the coordinates for each sample, we began to analyze the effect of each ion in order to find the emission concentration dependence. With the obtained data, we proceeded to calculate the distance between each sample coordinate and the reference white point E. This distance became the response parameter for the DOE analysis, and we discuss some important results in the following section.

Table 5.2: Concentrations of prototype samples used for constructing the experimental region. Quantities are in mol%.

Sample	Tm	Yb	Er	Ho
dde1	0.5	5	1	0.1
dde2	0.05	2	0.1	0.1
dde3	0.5	5	0.1	0.1
dde4	0.05	2	1	0.1
dde5	0.5	2	1	0
dde6	0.05	5	0.1	0
dde7	0.5	2	0.1	0
dde8	0.05	5	1	0

5.3.3. RESULTS

The purpose of the Pareto chart is to highlight the most important factors among a set of factors, over another under testing. From the Pareto chart of main effects shown in Figure 5.7, bars indicate three interactions (Tm·Er, Er·Ho and Yb·Er) and one main effect (Tm) related with whiteness. The plus and minus signals signifies that desired response gains advantage or disadvantage from those effects. The vertical blue line indicates the confidence level dividing the chart in two parts, and thus right side means a certainty. We note that the Tm ion concentration is the main factor for achieving white emission. In this case, this ion affects the final emission, due to the fact that all others must maintain a similar intensity in order to balance the resulting color. Unfortunately for us, the Tm ion is the weakest of the four. The second bar relates the Tm·Er interaction effect, and shows that this interaction should be controlled because it deteriorates the system behavior if concentrations for both ions are off. The third bar indicates that the Er ion is more relevant than Ho for white light generation, due

to the fact that a small amount of Ho ions present in the system favors intense green emission only. From the last bar we note that the Yb-Er concentration is less critical, even though the Yb^{3+} ion was considered necessary due to its energy transfer capacity and its influence on Er^{3+} ion emission.

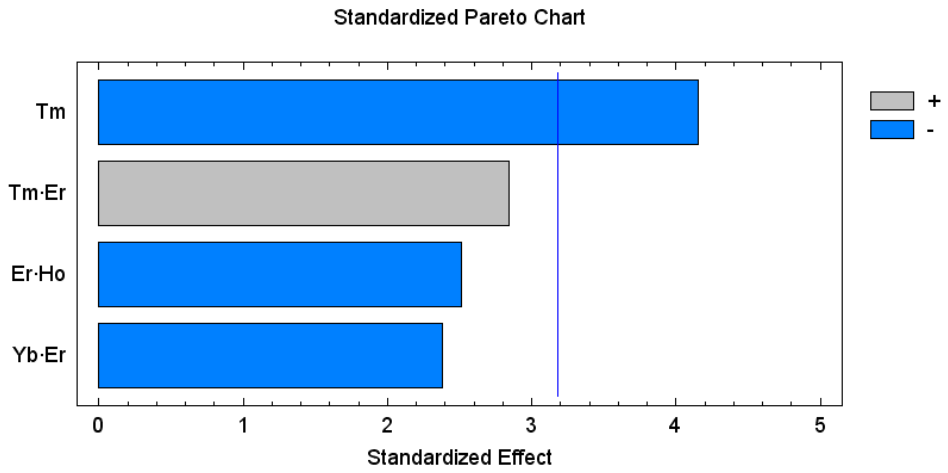

Figure 5.7: Pareto chart of main effects linked to white emission generation.

It is possible to observe three interactions from the interaction chart shown in Figure 5.8. The Tm·Er interaction exhibits a notable effect over whiteness. When Tm is set to its upper level and Er to its lower, the system tends to minimize the distance from reference white. Both Yb·Er and Er·Ho interactions have less significant overall effect over whiteness indeed, though in order to maintain Er in its low level is necessary to increase Yb^{3+} concentration. According to this chart, it is necessary prioritize the control of Tm^{3+} and Er^{3+} concentrations in order to achieve the goal, adjust Yb^{3+} concentration and discard the inclusion of Ho^{3+} ion.

We proceeded to calculate a linear model with the obtained data that represents the surface response of the system, in which all ion concentrations works as input variables and the whiteness as effect of interest. Using this model we synthesized two samples for testing, labeled as *pe* and *p2*, which are shown in Figure 5.8. The *p2* sample was obtained directly from the model. Nevertheless *pe* sample was obtained by considering that overly increasing

the concentration of Yb^{3+}, the emission would become reddish, and for the assumption it was required more Tm^{3+} concentration. However, results indicated that the surface was curved, so the test samples were used to explore the area of interest and to consider that a quadratic model yield a better approximation. To obtain the required model it was necessary to explore the coefficients of each factor from an equation called "saturated", i.e., where all coefficients exist. From this step, we proceed to find the significant coefficients and, in turn, fit the experimental data. The obtained model suggests Yb^{3+}=6 mol% and the non-interaction of Ho^{3+}, resulting the function:

$$CIE_{E\text{-}xy}(Tm, Er) = 0.377 - 1.442 \cdot Tm - 0.193 \cdot Er + 2.314 \cdot Tm^2 + 0.147 \cdot Er^2 \qquad (5.5)$$

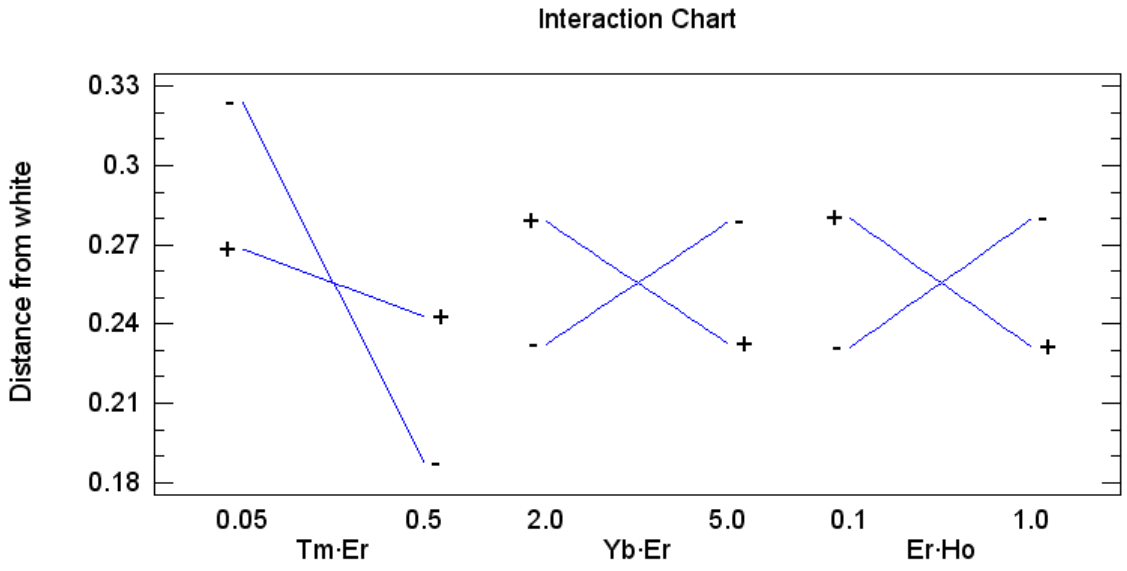

Figure 5.8: Interaction chart of the main effects linked to white light emission. Lower and upper levels for each first interaction ion (Tm, Yb, Er) are on the x axis; ones related to each second interaction ion (Er, Ho) are indicated with plus (+) and minus (-) symbols.

White target samples were done for this new model in order to obtain white emission. Samples are labeled as *t1*, *t2* and *t3*. Concentrations are in Table 5.3, resulting coordinates are represented on Figure 5.9, and corresponding emission images are shown in Figure 5.10.

Table 5.3: Concentrations for samples calculated for white approximation. Quantities are in mol%.

Sample	Tm	Yb	Er	Ho
pe	0.5	4	0.1	0
p2	0.05	6	0.2	0
t1	0.3	6	0.4	0
t2	0.3	6	0.8	0
t3	0.45	6	0.4	0

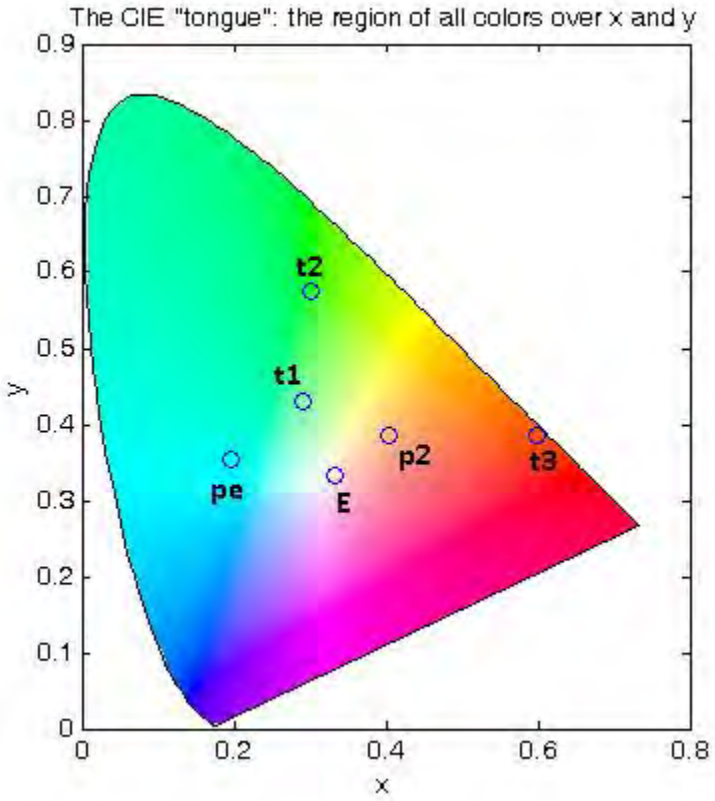

Figure 5.9: Distribution of chromaticity for samples calculated for the white approximation. Point E is the equipotential white that is used as a reference.

Figure 5.10: Emission images for target samples.

Perhaps the main advantage of using this DOE methodology is that every synthesized sample is useful since each coordinate is considered into the inferred response surface, resulting in a better approximation. In this manner, the testing is reduced significantly and improves the model. Every sample becomes a feasible tuning target. Figures 5.11 and 5.12 show the feasible tuning colors that the model can predict.

Figure 5.11: Set used to obtain valid concentration ranges for each ion. These samples exhibit part of the feasible tuning.

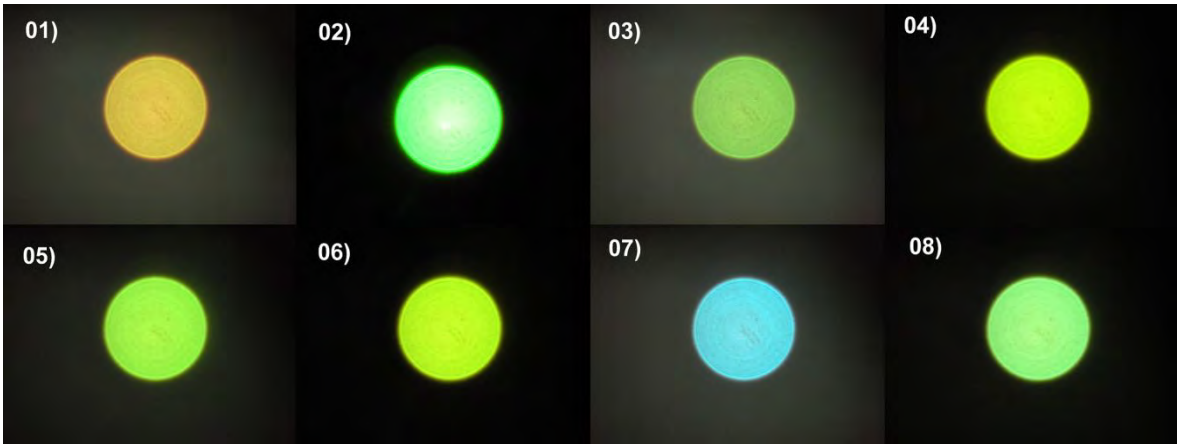

Figure 5.12: Set used for the first group of data to feed into the model. These samples exhibit part of the feasible tuning.

5.4. REFERENCES

[1] C.N.R. Rao, A. Müller, and A.K. Cheetham (eds.), Nanomaterials Chemistry, Recent Developments and New Directions, WILEY-VCH Verlag GmbH & Co. KGaA, Weinheim, 2007

[2] S.J. Green, J.I. Stokes, M.J. Hostetler, J. Pietron, R.W. Murray, "Three-dimension monolayers: Nanometer-sized electrodes of alkanethiolate-stabilized gol clusters molecules", J. Phys. Chem. B **101**, 2663 (1997)

[3] D.L. Gittins, D. Bethell, D.J. Schiffrin, R.J. Nichols, "A nanometre-scale electronic switch consisting of a metal cluster and redox-addressable groups", Nature **408** 67 (2000)

[4] N. Krasteva, I Besnard, B. Guse, R.E. Bauer, K. Mullen, A. Yasuda, T. Vossmeyer, "Self-Assembled Gold Nanoparticle/Dendrimer Composite Films for Vapor Sensing Applications", Nano Lett. **2**, 551 (2002)

[5] S. M. Briglin, T. Gao, N. S. Lewis, "Detection of Organic Mercaptan Vapors Using Thin Films of Alkylamine-Passivated Gold Nanocrystals", Langmuir **20**, 299 (2002)

[6] H. Ahn, A. Chandekar, B. Kang, C. Sung, J.E. Whitten, "Electrical Conductivity and Vapor-Sensing Properties of ω-(3-Thienyl)alkanethiol-Protected Gold Nanoparticle Films", Chem. Mater. **16** 3274 (2004)

[7] J.W. Grate, D.A. Nelson, R. Skaggs, "Sorptive Behavior of Monolayer-Protected Gold Nanoparticle Films: Implications for Chemical Vapor Sensing", Anal. Chem. **75** 1864 (2003)

[8] H. Wohltjen, A.W. Snow, "Colloidal Metal−Insulator−Metal Ensemble Chemiresistor Sensor", Anal. Chem. **70**(14) 2856 (1998)

[9] Q.A. Pankhurst, J. Connolly, S.K. Jones, J. Dobson, "Applications of magnetic nanoparticles in biomedicine", J. Phys. D: Appl. Phys. **36** R167 (2003)

[10] A. Jordan, R. Scholz, P. Wust, H. Fahling, R. Felix, "Magnetic fluid hyperthermia (MFH): Cancer treatment with AC magnetic field induced excitation of biocompatible superparamagnetic nanoparticles", J. Magn. Magn. Mater. **201** 413 (1999)

[11] A. Jordan, R. Scholz, K. Maier-Hauff, M. Johannsen, P. Wust, J. Nadobny, H. Schirra, H. Schmidt, S. Deger, S. Loening, "Presentation of a new magnetic field therapy system for the treatment of human solid tumors with magnetic fluid hyperthermia", J. Magn. Magn. Mater. **225** 118 (2001)

[12] S. Pathak, S.K. Choi, N. Arnheim, M.E. Thompson, "Hydroxylated quantum dots as luminescent probes for in situ hybridization", J. Am. Chem. Soc. **123** 4103 (2001)

[13] H. Mattoussi, J.M. Mauro, E.R. Goldman, G.P. Anderson, V.C. Sundar, F.V. Mikulec, M.G. Bawendi, "Self-Assembly of CdSe−ZnS Quantum Dot Bioconjugates Using an Engineered Recombinant Protein", J. Am. Chem. Soc. **122** 12142 (2000)

[14] Z. Chunyang, M. Hui, D. Yao, J. Lei, C. Dieyan, N. Shuming, "Quantum dot-labeled trichosanthin", Analyst **125** 1029 (2000)

[15] J.O. Winter, T.Y. Liu, B.A. Korgel, C.E. Schmidt, "Recognition Molecule Directed Interfacing Between Semiconductor Quantum Dots and Nerve Cells", Adv. Mater. **13** 1673 (2001)

[16] M. Dahan, T. Laurence, F. Pinaud, D.S. Chemla, A.P. Alivisatos, M. Sauer, S. Weiss, "Time-gated biological imaging by use of colloidal quantum dots", Opt. Lett. **26** 825 (2001)

[17] Q.L. De Chermont, C. Chaneac, J. Seguin, F. Pelle, S. Maitrejean, J.P. Jolivet, et al, "Nanoprobes with near-infrared persistent luminescence for in vivo imaging", Proc. Natl. Acad. Sci. USA **104**(22), 9266–71 (2007)

[18] Z.Q. Li and Y. Zhang, "Monodisperse silica-coated polyvinylpyrrolidone/$NaYF_4$ nanocrystals with multicolor upconversion fluorescence emission". Angew. Chem. Int. Ed. **45**(46), 7732–5 (2006)

[19] Wang F, Chatterjee DK, Li Z, Zhang Y, Fan XP and Wang MQ, "Synthesis of polyethylenimine /NaYF4 nanoparticles with upconversion fluorescence", Nanotechnology **17**, 5786–91 (2006)

[20] J.V. Frangioni, "In vivo near-infrared fluorescence imaging", Curr. Opin. Chem. Biol. **7**(5), 626–34 (2003)

[21] Chatterjee DK, Rufaihah AJ & Zhang Y, "Upconversion fluorescence imaging of cells and small animals using lanthanide doped nanocrystals", Biomaterials, **29**, 937-943 (2007)

[22] M. Hosokawa, S. Tajika, H. Kiyoshi, N. Makio, N. Toyokazu, Y. Shoudai, T. Hirakata (eds.), Nanoparticle Technology Handbook, Elsevier B.V., Linacre House, Jordan Hill, Oxford OX2 8DP, UK First edition 2007

[23] Y. Nishisu, M. Kobayashi, Report of the millennium project (Environment, No. 12317; Research and development of phosphors for a mercury-free lamp) by Science and Technology Agent (2006)

[24] M. Kakihana, Y. Kawahara, T. Ichihara and N. Kijima, Phosphor Research Society of the 304th Meeting Technical Digest, 25 (2004)

[25] T. Masui, Y. Mayama, K. Koyabu and N. Imanaka, "Synthesis of New Green-Emitting $Gd_2O_2CO_3:Tb^{3+}$ Fine Particles with High Luminescent Intensities", Chem. Lett., **34**, 1236 (2005)

[26] S. Yanagida, Y. Wada and Y. Hasegawa, "Molecular Designs of Lanthanide Complexes for Remarkable Luminescence and Their Applications", Phosphor Research Society of the 293rd Meeting Technical Digest, p.15 (2002)

[27] S. Yatsunenko, W. Lojkowski, G. Markovic, J. Loeffler, "R&D report on Nanoparticles", analysis compiled within the European project "Development of Advanced Technology Roadmaps in Photonics and Industrial Adaptation to Small and Medium sized Enterprises" ("PhotonicRoadSME"). Project funded by the European Commission under the "Seventh Framework" Programme (Project Number 224572), October 2009.

[28] http://en.wikipedia.org/wiki/File:CIE_1931_XYZ_Color_Matching_Functions.svg

[29] J. Schanda, Colorimetry: Understanding the CIE System, Wiley Interscience, (2007)

[30] Figure 7 from Stockman, A. (2004). Colorimetry. In T.G. Brown, K. Creath, H. Kogelnik, M.A. Kriss, J. Schmit & M.J. Weber (Eds.), The Optics Encyclopedia: Basic Foundations and Practical Applications (Vol. 1, pp. 207-226). Berlin: Wiley-VCH

[31] D. Solís, T. López-Luke, E. De la Rosa, P. Salas, and C. Angeles-Chavez, "Surfactant effect on the upconversion emission and decay time of ZrO_2:Yb-Er nanocrystals," Journal of Luminescence **129**, 449 (2009)

[32] D. Solis, E. De la Rosa, P. Salas, and C. Angeles-Chavez, "Green upconverted emission enhancement of ZrO_2:Yb^{3+} - Ho^{3+} nanocrystals," Journal of Physics D: Applied Physics **42**, 235105 (2009)

[33] Montogomery DC, Design and analysis of experiments, John Wiley and Sons, 5th edition, Singapore, (2000)

CHAPTER 6

CONCLUSIONS AND REMARKS

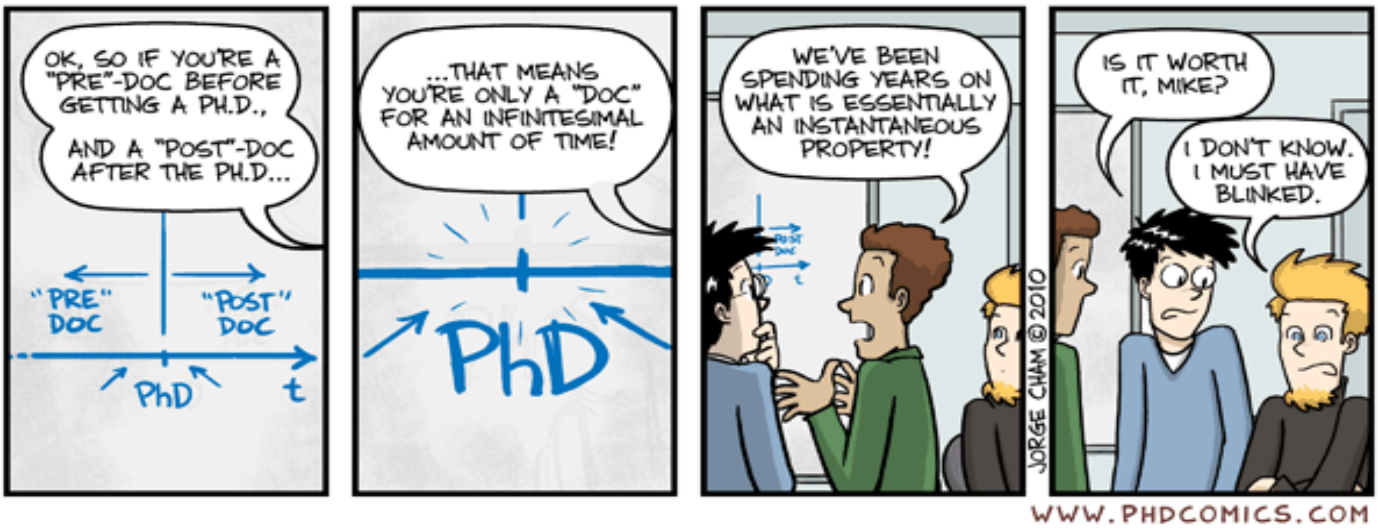

6.1. GENERAL CONCLUSION

What has been exposed through the chapters is undoubtedly the work that was carried out on the characterization of the properties of the material under study. Analyzed ions were Er^{3+}, Ho^{3+} and Tm^{3+} in conjunction with Yb^{3+} as a sensitizer, along with the use of ZrO_2 as a crystal host, using nearly a general synthesis method. Below are outlined relevant aspects from each system analyzed in this work, in order to recapitulate main points.

6.1.1. REGARDING ZrO_2:Yb^{3+}, Er^{3+}

Green and red visible emissions were obtained after 970 nm excitation. The color coordinate of the up-converted signal could be tailored by controlling the red/green ratio with the appropriate ion concentration. Up-conversion is favored by energy transfer from donor (Yb^{3+}) to acceptors (Er^{3+}). However, the red/green ratio and then the color coordinate are dominated by the cross relaxation (CR) and energy back transfer (EBT) process as was demonstrated theoretically and confirmed experimentally. Both contributions, CR and EBT, depend on the acceptor and donor concentration, respectively. In fact, experimental results indicate that cross-relaxation coefficient is larger than the energy back transfer is. However, the CR term is dominant for a concentration ratio Yb/Er ≤ 1.72. Both coefficients increase with the increment of sensitizer where cubic phase is dominant but C_{51} increase faster than C_{5b}. From the proposed model and experimental results, both coefficients were calculated resulting C_{51}~$1.02x10^{-16}$ cm^3s^{-1} and C_{5b}~$6.04x10^{-17}$ cm^3s^{-1} (for the largest concentration of dopants). The highest energy transfer efficiency calculated was η~64% for 2 mol% of Yb_2O_3 and 2 mol% of Er_2O_3. However, for the highest up-converted signal η was only about 29% obtained for 1 mol% Er_2O_3. The strength and tunability of emitted signal make these nanocrystals very attractive for luminescence labeling technology.

6.1.2. REGARDING ZrO_2:Yb^{3+}, Ho^{3+}

Strong, bright green up-conversion emission was obtained for 20 nm-sized nanocrystals with primarily tetragonal crystalline phase (about 70 wt%), as determined by the co-dopant content. Moreover, the up-converted signal is strongly dependent on the composition of both co-dopant ions, and the experimental results do not point to any apparent relation between

crystallite size and crystalline phase. The highest signal emission obtained for Yb/Ho doped at 2/0.001 mol% is 600% higher than that obtained for a Yb/Ho sample doped with Ho^{3+} at a concentration three orders of magnitude higher, implying that clustering interaction with Ho^{3+} happens promptly. Larger concentrations of both donors and acceptors produce luminescent quenching because of energy migrations due to inter-ionic cluster interaction. This process also reduces the energy transfer efficiency that in turn could reduce the up-conversion emission. The strong relation between τ_{eff} and the green emission band with Ho^{3+} concentration suggests that the dynamics of the visible emission are dominated by migration due to cluster formation. However, the rapid intensity loss for higher concentrations of Yb^{3+} is probably the result of a back transfer ($Ho^{3+} \rightarrow Yb^{3+}$) process. These results indicate that there is a zone for optimized concentration.

6.1.3. REGARDING ZrO_2:Yb^{3+}, Tm^{3+}

Luminescence up-conversion emissions were obtained after 970 nm excitation for ZrO_2:Yb^{3+}-Tm^{3+} nanocrystals with CTAB as surfactant. The XRD patterns shown crystalline phase composition of samples annealed for 2 and 5 hours at 800°C, are primarily tetragonal, for both sol-gel and micelle applied processes. For low dopant concentrations the tetragonal crystalline structure is more affected by temperature than annealing time. The emission spectra exhibits four distinct emission bands, from which the infrared and blue bands peaked at 800 nm ($^3H_4 \rightarrow {}^3H_6$) and 470 nm ($^1G_4 \rightarrow {}^3H_6$) represent about 80% from total visible signal. The system is very influenced by quenching originated from cluster interaction with Tm^{3+}, suggesting the presence of energy migration processes, and the introduction of Yb^{3+} produces the peak at 501 nm ascribed to cooperative emission. CUC emission is more intense due to the fact that in Yb^{3+}- Tm^{3+} pair the excitation is less efficient because of the smaller resonance in the first channel of energy transfer between the donor and the acceptor. A fast analysis of Yb^{3+} samples with rare-earth remnants (traces) indicates CUC emission by presence of Yb^{3+}-Yb^{3+} pairs. The maximum blue signal was obtained with 2 mol% of Yb^{3+} and 0.05 mol% of Tm^{3+}, this strong increase can be attributed to the reduction of Tm^{3+} inter-ionic cluster interactions. The blue UC emission from Tm^{3+} is affected by the cross-relaxation channel ($^3H_5 \rightarrow {}^3H_6$) + ($^3F_4 \rightarrow {}^3F_3$), which explains the relative incremented luminescence at 800 nm with

the increment of Tm^{3+} concentration. By comparing decay kinetics between both bands it is suggested that at 470 nm the fast component is ascribed to cross-relaxation. Detriment of effective decay kinetics does not occur for 800 nm band when CR channel is reduced.

6.1.4. REGARDING APPLICATION OF MULTIDOPED ZrO_2 NANOCRYSTALS

ZrO_2:Tm^{3+}, Yb^{3+}, Er^{3+}, Ho^{3+} nano-crystalline samples were synthesized by sol-gel method and up-converted emission properties analyzed as function of different concentrations of these rare-earth ions. During this work it was necessary to develop a method by which color coordinates for each sample could be rapidly calculated. From these results, a procedure is proposed for color tuning, as well as is described the feasibility of obtaining white light emission from a combination of ions concentrations of Yb, Tm and Er. The behavior of the whiteness and its relation with concentration of each ion was studied so as to build a fitting response surface, from which were possible to synthesize samples that met the considered purpose. Experimental data indicated that a quadratic model was required to obtain a better approximation; that model follows the form $Tm + Er + (Tm)^2 + (Er)^2$. These results indicate the feasibility of a model that could be used to infer the required concentration of Tm^{3+}, Yb^{3+}, Er^{3+} and Ho^{3+} ions on the basis of a given emission color coordinate.

6.2. GENERAL REMARKS

The results obtained in each case and the characteristics that were exposed from analyzed ion-host systems are specific and individual, however, I think they are able to be a guide to infer the general properties in other particular system.

The nanoparticles prepared by the sol-gel method without surfactant are more agglomerated. The results show that surfactants prevent the agglomeration of nanoparticles, passivate particle surfaces and reduce adsorption of contaminants such as OH, increasing the emitted luminescence. This is the result of the formation of micelles around each nanoparticle by using optimal concentrations of surfactant. Pluronic F-127 was studied with the purpose of comparing it with the cationic surfactant CTAB as to decide which one is more effective in

eliminating remnants during the synthesis process, especially the OH's. Samples synthesized with non-ionic surfactant Pluronic F-127 by a molar ratio Pluronic/ZrO_2 = 0.0082, presented a signal enhancement that is more intense than the ones obtained using the cationic surfactant CTAB, with molar ratio CTAB/ZrO_2 = 0.2. Pluronic F-127 has lower agglomeration and better remnant reduction. Finally, the advantages from CTAB could not be concluded at least for the annealing temperature of 800^{o}C. The emission of ZrO_2:Er-Yb ions are much more intense than that of doped ZrO_2:Er. With a molar ratio of 0.0082 was obtained notable increment emissions. Hence we conclude that the emission intensity is correlated to the type of surfactant. These results suggest that it may have strong emission intensities with surfactants with long chains, with two or more hydrophilic parts.

Large amounts of surfactant contribute to the formation of the tetragonal phase. The size and morphology was partially controlled with the surfactant, however, the main size control was achieved with time and annealing temperature. Nanocrystals with smaller particle size were obtained at 800^{o}C; suitable for a luminescent enhancement but their low luminescence is associated with the impurities remained at this temperature. Nonetheless, with these nanocrystals luminescence was enhanced comparing to samples without surfactant. We conclude that this increase in emissions is due to the reduction of contaminants remaining on the surface of nanoparticles, such as OH and CO_2. Samples at 1000^{o}C exhibit better luminescent intensity by remnant reduction, though their larger sizes do not exploit this advantage at all. A synthesis method that involves a better hydrolysis and surfactant combination, low annealing temperature, remnant reduction as well as impurity control is required to obtain improved results.

The decay times from emission confirmed that the residue on the surface of the nanocrystal are responsible for generating both short decay and long decay times, as shown by the samples with and without surfactant. The short time is related to phononic processes generated by remnants that could not be removed. According to the results, we conclude that

the increase on decay time is resulted from the elimination of superficial OH rather than the effect of crystal size and phase composition.

According to ion phenomena, there is a strong influence of both Yb^{3+} and Er^{3+} ion concentrations over the red/green ratio behavior mainly due to cross-relaxation. The blue UC emission from Yb^{3+}-Tm^{3+} is affected favorably by the cross-relaxation channel as well. The strong increase in blue signal can be attributed to the reduction of Tm^{3+} inter-ionic cluster interactions. The highest green signal emission obtained for very low concentration of Ho^{3+} implies promptly clustering interaction with Yb^{3+}. It is clear that the excitation dynamics is relevant part on the luminescent processes in nanocrystals. Thus is desirable the use of a technique that could produce clean surfaces and less organic remnants, to enhance the dynamic resulted from nano size effect. A more control over variables involved on chemical synthesis, such as size and surface passivation, is required as to achieve better manipulation and consistency in the final characteristics of produced materials.

On the other hand, results indicate that there is a feasible model that could be used to tailor the required concentration of ions on the basis of a given emission color coordinate. Though a detailed mathematical analysis is essential to test the properties of the model and its real viability, is very possible the need to prepare test samples to obtain required data so as to adjust and apply such model for each given system and synthesis method applied, and thereby losing its attraction. It could be a long term trial and its benefit is needed to be considered.

The feasibility of strong and tunability of emitted signal make these nanocrystals very attractive for luminescence labeling technology. To carry out this potential application is necessary to make small controlled-size particles with great dispersion and solubility. Moreover, a complete research in relation to how functionalize nanocrystals attaching them to specific molecules is required, as well as the finding of a procedure to obtain biocompatibility of the produced material.

For all the above we can conclude that information obtained during this project provides the right conditions for continuing a later stage where long-term goals can be carried out once the potential applications are determined to exploit the knowledge acquired. Improved methods of synthesis as well as an interdisciplinary work are critical to develop a tangible benefit to society.

List of publications, conferences and work in preparation derived from this research

Publications

D. Solis, E. De la Rosa, O. Meza, L.A. Diaz-Torres, P. Salas, C. Angeles-Chavez, "Role of Yb^{3+} and Er^{3+} concentration on the tunability of green-yellow-red upconversion emission of codoped ZrO_2:Yb^{3+}-Er^{3+} nanocrystals", Journal of Applied Physics, **108**, 023103-023109 (2010).

O. Meza, L.A. Diaz-Torres, P. Salas, E. De la Rosa and D. Solis. "Color tunability of the up-conversion emission in Er–Yb doped the wide band gap nanophosphors ZrO_2 and Y_2O_3", Materials Science and Engineering: B, article in press, (March, 2010)

D. Solís, T. López-Luke, E. De la Rosa, O. Meza, S. Anderson, "Syntonized white up-converted emission by Tm^{3+}-Yb^{3+}-Er^{3+}-Ho^{3+} doped ZrO_2 nanocrystals", Photonics West Conference, Proc. of SPIE Vol. 7617 76171Q-1 (2010).

D. Solís, E. De la Rosa, P. Salas and C. Angeles-Chávez, "Green upconverted emission enhancement of ZrO_2: Yb^{3+}–Ho^{3+} nanocrystals", Journal of Physics D: Applied Physics, **42** (23), pp. 235105-8 (2009).

P. Ghosh, E. De la Rosa, J. Oliva, D. Solis, A. Kar, and A. Patra, "Influence of surface coating on the upconversion emission properties of $LaPO_4$:Yb/Tm core-shell nanorods", Journal of Applied Physics, 11 (105), pp. 113532-5 (2009).

O. Meza, L.A. Diaz-Torres, P. Salas, E. De la Rosa, C. Angeles-Chavez, and D. Solis, "Cooperative pair driven quenching of Yb^{3+} emission in nanocrystalline ZrO_2:Yb^{3+}", Journal of Nano Research, v.**5**, pp. 121-134 (2009).

D. Solis, T. Lopez-Luke, E. De la Rosa, P. Salas, C. Angeles-Chavez, "Surfactant effect on the upconversion emission and decay time of ZrO_2:Yb-Er nanocrystals", Journal of Luminescence, **129**, 5, pp. 449-455 (2008).

E De la Rosa, D Solis, L. A. Díaz-Torres, P Salas, C Angeles-Chavez, O Meza, "Blue-green upconversion emission in ZrO_2: Yb^{3+} nanocrystals", Journal of Applied Physics, **104** (1), 6, (2008).

Ghosh P, Oliva J, De la Rosa E, Haldar KK, Solis D, Patra A, "Enhancement of upconversion emission of $LaPO_4$: Er@Yb core-shell nanoparticles/nanorods", Journal of Physical Chemistry C, 112 (26), pp. 9650-9658 (2008).

Lopez-Luke T, De la Rosa E, Solis D, Salas P, Angeles-Chavez C, Montoya A, Diaz-Torres LA, Bribiesca S, "Effect of the CTAB concentration on the upconversion emission of ZrO_2: Er^{3+} nanocrystals", Optical Materials, 29 (1), pp. 31-37 (2006).

Paper in preparation

D. Solís, E. De la Rosa, T. López-Luke, P. Salas, C. Angeles-Chavez, "Ion concentration effect on the spectroscopic properties of ZrO_2:Yb^{3+} – Tm^{3+} nanocrystals".

D. Solís, T. López-Luke, A. Christen, E. De la Rosa, P. Salas, "Response surface model for emission tuning on ZrO_2:Yb^{3+} – Tm^{3+} – Er^{3+} nanocrystals".

Conference Presentations

D. Solís, T. López-Luke, E. De la Rosa, O. Meza, S. Anderson, "Syntonized white up-converted emission by Tm^{3+}-Yb^{3+}-Er^{3+}-Ho^{3+} doped ZrO_2 nanocrystals", Photonics West, San Francisco, CA, EU, January 2010.

D. Solís, O. Meza, E. De la Rosa, "Estudio de mezclas y aproximación a la emisión blanca en sistemas nano-cristalinos de ZrO_2 tri-dopados", Congreso Sociedad Mexicana de Física, Acapulco, Gro., México, Octubre 2009.

D. Solís, T. Lopez-Luke, E. De la Rosa, L. Meza, S. Anderson, A. Christen, "Concentration analysis of Tm^{3+}, Yb^{3+}, Er^{3+} and Ho^{3+} ions into ZrO_2 nano-sized crystals towards feasible control of the chromaticity", Congreso NANOTECH, Guaymas, Son., México, Septiembre 2009.

D. Solís, O. Meza, E. De la Rosa, "Cálculo de coordenadas de color de la luminiscencia de emisión hacia arriba en fósforos nano-cristalinos y aproximaciones en la obtención de emisión blanca", Congreso VI Encuentro Participación de la Mujer en la Ciencia, León, Gto., México, Agosto 2009.

D. Solís, T. López-Luke, E. De la Rosa, O. Meza, S. Anderson, L.A. Díaz-Torres, A. Christen, "Feasible control over color tuning of Tm^{3+}, Yb^{3+}, Er^{3+} doped ZrO_2 nano-sized crystals", Congreso NANOTECH, León, Gto., México, Mayo 2009.

D. Solís, E. De la Rosa, P. Salas, "Up conversion characterization of ZrO_2:Yb^{3+}-Tm^{3+} nanocrystals", Congreso NANOTECH, DF, México, Noviembre 2008.

D. Solís, E. De la Rosa, P. Salas, "Ion concentration effect on the spectroscopic properties of ZrO_2:Yb^{3+}-Ho^{3+} nanocrystals", Congreso Sociedad Mexicana de Física, Zacatecas, Zac., México, Octubre 2008.

D. Solís, E. De la Rosa, P. Salas, "Ion concentration dependence on green up conversion luminescence of ZrO_2:Yb^{3+}-Ho^{3+} nanocrystals", SPIE Optics and Photonics, San Diego, CA, EU, August 2008.

D. Solís, E. De la Rosa, P. Salas, "Upconversion characterization of ZrO_2:Yb^{3+}-Tm^{3+} nanocrystals", SPIE Optics and Photonics, San Diego, CA, EU, August 2008.

D. Solís, T. López, P. Salas, E. de la Rosa, "Ion concentration effect on the spectroscopic properties of ZrO_2:Yb^{3+}-Ho^{3+} nanocrystals", Congreso NANOTECH, Monterrey, NL., México, Noviembre 2007.

D. Solís, T. López, P. Salas, E. de la Rosa, "Mejoramiento de la emisión de conversión hacia arriba en nano cristales de ZrO_2:Yb^{3+}-Er^{3+} por el proceso de micelas usando Pluronic F-127 durante el método de síntesis", Congreso de la Sociedad Mexicana De Cristalografía, Guadalajara, Jal., Octubre 2007.

D. Solís, L.A. Díaz-Torres, E. De la Rosa, P. Salas, "Tuning the green-red upconversion emission of ZrO_2:Yb^{3+}-Er^{3+} nanocrystals", Congreso NANOTECH, Puebla, Pue., México, Septiembre 2006.